University of Gdansk, Faculty of Chemistry

mgr Łukasz Lewandowski

NEW PHOTOCATALYSTS COVERED IN GRAPHENE

PhD thesis supervisor:
Prof. Dr hab. inż. Adriana Zaleska-Medynska
Auxillary PhD thesis supervisor:
Dr inż. Anna Gołąbiewska

Gdańsk 2022

Table of contents:

Abbreviations:

AQE - Apparent quantum efficiency
AQY - Apparent quantum yield
BQ - p-Benzoquinone
c - The speed of light
CCC - Concordance correlation coefficient
CDOM - Chromophoric dissolved organic matter
CVD - Chemical vapor deposition
EDS - Energy Dispersive X-ray spectrum
eV - Electron Volt
h - Planck's constant
HAADF - High Angle Annular Dark Field imaging
NHE - Normal hydrogen electrode
PC - Photochemical
PEC - Photoelectrochemical
POP - Persistent organic pollutant
PV-EC - Photovoltaic-electrochemical
PVSP - Photovoltaic solar panels
pXRD - Powder X-ray diffraction
RMSE - The root mean square error
sccm - Flow speed (cm^3 min^{-1})
SDHP - Solar-driven hydrogen production
SEM - Scanning electron microscopy
STEM - Scanning Transmission Electron Microscopy
STH - Solar to hydrogen
TBA - tert-Butyl alcohol
TEM - Transmission electron microscopy
XPS - X-ray photoelectron spectroscopy
XRD - X-ray diffraction

Abstract

The goal of transforming photocatalysts into practical tools has been pursued through the use of scalable industrial methods, resulting in the development of new photocatalytic materials. Specifically, a TiO_2-Cu-Graphene composite has been synthesized using a newly designed fluidized bed reactor and chemical vapor deposition. Optimal synthesis conditions were determined through computer aided modelling, which identified an inverse correlation between activity and both the temperature and time of graphene synthesis. The most effective sample achieved a 2.06% efficiency in hydrogen evolution from water photoconversion. The incorporation of a graphene layer improved the activity of the material and may have played a role in hindering the conversion of metallic copper to oxides.

Additionally, an Ag_3PO_4-Graphene composite was obtained via graphene plasma sputtering and successfully employed for water purification, with phenol serving as the model pollutant. Depending on the duration of graphene sputtering, the coating exhibited no or slightly detrimental influence on the photoactivity of the composite, but significantly improved its stability.

Streszczenie

W celu zbliżenia się do praktycznego wykorzystania fotokatalizatorów, opracowano nowe materiały fotokatalityczne za pomocą skalowalnych technik przemysłowych. Syntetyzowano kompozyt TiO_2-Grafen w nowoczesnym reaktorze fluidyzacyjnym, wykorzystując metodę chemicznego osadzania z fazy gazowej (CVD). Warunki optymalne dla syntezy zostały określone dzięki modelowaniu wspomaganemu komputerowo, które wykazało odwrotną zależność między aktywnością materiałów a temperaturą i czasem syntezy grafenu. Najbardziej efektywna próbka osiągnęła 2,06% wydajności w produkcji wodoru z fotokonwersji wody. Warstwa grafenu na powierzchni próbki nieco zwiększyła wydajność materiałów i mogła odgrywać istotną rolę w hamowaniu lub opóźnianiu procesu utleniania metalicznej miedzi zawartej w próbkach. Opracowano również kompozyt Ag_3PO_4-Grafen, stosując technikę napylania plazmowego. Uzyskany fotokatalizator został z powodzeniem wykorzystany do oczyszczania wody, przy fenolu jako modelowym zanieczyszczeniu. W zależności od czasu napylania grafenu, warstwa ta okazała się nie wpływać lub nieco obniżać fotoaktywność materiału, jednak jednocześnie znacznie zwiększała jego stabilność.

1 The aim and scope of work

The objective of this study was to investigate the potential applications of photocatalysts in various industrial sectors. The research aimed to assess the current state of photocatalytic science in terms of efficiency, economic viability, and practicality. The study also aimed to evaluate scalable synthesis methods to determine the extent to which photocatalysts can be implemented in common usage, and to identify the most feasible approach for achieving this goal. Additionally, this investigation explored the feasibility of using graphene as an alternative to expensive and potentially hazardous noble and/or heavy metal components in photocatalysts.

The experimental section was based on the following hypotheses:

1. Applying graphene to the surface of a semiconductor can enhance its photoactivity by acting as a metal cocatalyst.
2. Applying graphene to the surface of a semiconductor can enhance its photoactivity by increasing the material's specific area.
3. Applying a graphene coating to the surface of a semiconductor can enhance its stability by preventing oxidation and reduction of metal cocatalysts and semiconductors, respectively.
4. Scalable industrial methods are applicable for photocatalyst synthesis.
5. Graphene can be synthesized at relatively low temperatures of 500ºC, allowing for the use of affordable glass containers instead of quartz ones.
6. Graphene plasma sputtering can be performed using a simple plasma sputtering reactor.
7. Graphene synthesis can be carried out directly on fluidized semiconductor particles using a fluidized bed reactor.

The experimental section aimed to achieve the following specific objectives:

1. To develop a chemical vapor deposition (CVD) method for coating TiO_2 with graphene in a fluidized bed reactor. The objective of this method was to enhance the photocatalytic activity of the semiconductor in terms of hydrogen evolution from water photoconversion.

2. To establish a correlation between the synthesis parameters, graphene shell thickness, and photocatalytic properties of the resulting material.

3. To develop a plasma sputtering-based modification method for Ag_3PO_4-graphene composites, with the aim of improving their photocatalytic activity and stability.

4. To investigate the impact of graphene on the activity of Ag_3PO_4 and the relationship between activity and light spectrum using action spectra analysis.

2. Introduction

Given the constant growth of global energy demand and the inevitable depletion of fossil fuels and other non-renewable sources, many scientists have shifted their focus towards renewable energy sources, due to their negative environmental impact. The average annual electrical energy demand per person in Europe has grown from 1215.8 kWh in the 1960s to 6352.8 kWh in 2014 [1]. This growth is expected to continue, as energy demand is positively correlated with technological advancements and societal growth (Figure 1).
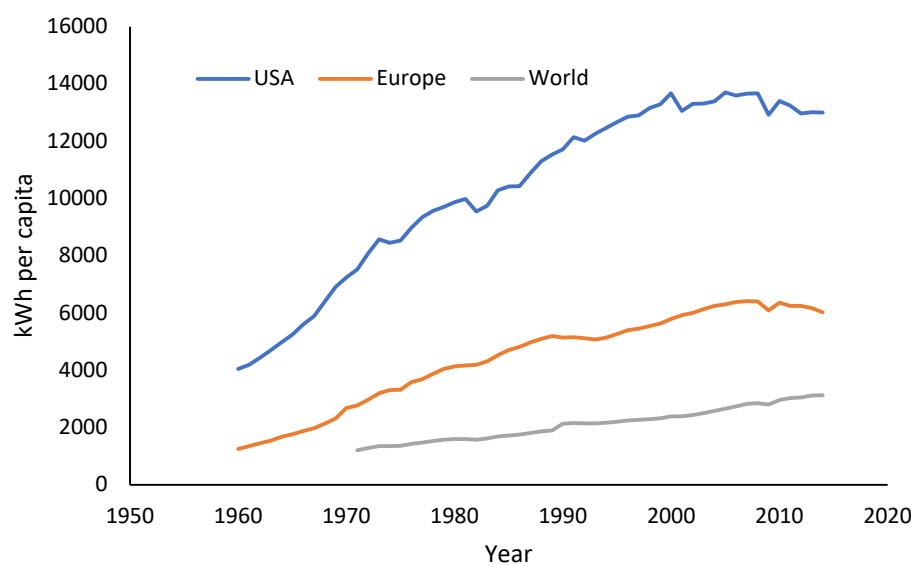
Figure 1 Electrical energy consumption per capita over the years 1960-2014 [1]

This trend is not limited to Europe, and despite disparities in energy consumption among developed regions such as the United States and Europe, energy demand is projected to rise globally as developing nations catch up. Meeting this demand will require the construction of new power plants with environmentally friendly technology. However, to enable this transition towards green energy, technical challenges of renewable sources, such as efficient energy storage, must be overcome [2-6]. Currently, one of the most significant challenges is the lack of efficient energy storage methods for renewable sources such as wind turbines, water turbines,

and solar panels. Excess energy produced by renewable sources is typically lost and can pose a risk to electrical grids by causing damage and malfunctions. Renewables are often dependent on weather conditions and therefore have an uneven temporal distribution, making them unreliable and difficult to use as stand-alone energy sources. Building energy storage facilities like industrial battery banks or pumped storage hydro power stations can address this issue. However, such solutions are expensive and inefficient, with up to 75% of energy being lost due to technical reasons [2-6].

Another approach to addressing the energy storage problem is the use of photocatalysts. Photocatalysts allow for the direct use of light for various applications, such as pollutant degradation in water or hydrogen generation from water splitting. Direct photoinduced hydrogen evolution can potentially solve the energy storage problem, as hydrogen is an energy carrier that can be stored and used based on momentary energy demand. The current research focuses on the advancement of photocatalyst technology and its readiness for industrial applications.

3. Renewable energy sources available today:

As the demand for renewable energy sources continues to increase, the availability of local resources remains a limiting factor. Each type of renewable energy technology has unique requirements and environmental risks associated with its implementation. Currently, hydroelectric plants, wind turbines, and photovoltaic solar panels are the most commonly used renewable energy technologies, but this may change with the emergence of new technologies such as wave, tide, kite, and bladeless wind energy tapping methods that are still in development [7-8].

Hydropower is a form of energy derived from water runoff through hydraulic turbines. It is a specific type of source that requires a suitable landscape and has a relatively high environmental impact due to the need to retain water in artificial bodies in order to create sufficient pressure for turbine operation. When built on rivers, it creates barriers that hinder the ability of nekton organisms to traverse the river upstream and downstream. Although some workarounds are possible, the environmental impact is always significant. However, hydropower has several advantages. In favorable conditions, it can be a useful energy source as the energy production and output are mostly constant, and it does not rely on energy storage facilities to the same extent as other renewable energy sources. Norway provides an excellent example of the

utilization of hydroelectric power plants, as they cover nearly 100% of the country's electrical demand, with the only Norwegian coal-powered electrical plant located in Longyearbyen on the Spitsbergen island [8].

Wind energy conversion systems, commonly known as wind turbines, have been in use since medieval or even ancient times. However, the true proliferation of wind energy has only occurred in recent decades, as advancements in material science have enabled the construction of large, lightweight turbine blades and the establishment of both land and marine wind farms [9]. While wind energy is subject to specific landscape and meteorological conditions, it is a more globally applicable form of energy than hydroelectric power. Unlike hydropower, wind turbines are dependent on wind conditions and thus less reliable in terms of consistent power output. To optimize wind energy potential, energy storage facilities must be employed. The negative environmental impact of wind turbines includes the risk of collision with birds and bats, as well as landscape disruption, strobe effect, and the non-recyclability of turbine blades that have reached the end of their service life [10-11]. The capacity of onshore wind turbines is typically around 2.5 MW, while their larger offshore counterparts can generate up to 3.5 MW of electricity per turbine. Several offshore wind farms are planned for construction off the Polish Coast in the Baltic Sea [12].

Photovoltaic solar panels (PVSP) are devices that directly convert sunlight into electricity. The output of these devices is directly dependent on the amount of insolation, which varies depending on weather and latitude. The utility of PVSP is also influenced by the season and local microclimate, which determines the amount of direct sunlight received in a given location. A significant advantage of PVSP is their lack of moving parts and modular construction, allowing them to be installed in a variety of locations, from individual homes and large vehicles to industrial-scale solar farms. However, like most renewable energy sources, they require energy storage facilities to provide power 24 hours a day. The efficiency of PVSP varies, ranging from $26.7 \pm 0.5\%$ for Si crystalline cells to $39.2 \pm 3.2\%$ for Six-junction (monolithic) (2.19/1.76/1.45/1.19/.97/.7 eV) cells and up to $47.1 \pm 2.6\%$ for the AlGaInP/AlGaAs/GaAs/GaInAs(3) (2.15/1.72/1.41/1.17/0.96/0.70 eV) panel type, as per the Version 57 and 58 Solar Cell Efficiency Tables from 2020 and 2021 [13-14].

Photocatalysts are a class of semiconductor-based materials that enable the direct utilization of sunlight (or artificial light) for a range of applications, including air and water purification, virus and bacteria inactivation, self-cleaning surfaces, and hydrogen production via

photoinduced water splitting or water photoconversion. Despite being mainly in the laboratory research phase [15], the first attempts at semi-industrial application have been made. For example, the University of Tokyo has developed a functional photocatalytic water splitting device at the Kakioka research facility. The setup used $SrTiO_3$:Al as the photocatalyst for water splitting and separated the evolved oxygen/hydrogen mixture via a semipermeable membrane filter. The installation was found to be safe, even in the event of a gas explosion due to the ignition of the mixture. However, several improvements are still required, as the oxygen/hydrogen separation was far from satisfactory (20% of evolved hydrogen was not separated), and the energy balance was at a net loss (5.0 MJ obtained for every 6.1 MJ required to run the equipment of the setup). Nevertheless, considering that the maximum theoretical Solar To Hydrogen (STH) conversion of the photocatalyst used was 0.76%, the setup's efficiency could be significantly improved with a more efficient photocatalyst [16, 17, 18]. Photocatalysts will be discussed broader in the further sections of this work.

The utilization of renewable energy sources for electricity generation in Europe has been evolving since the turn of the 21st century, as demonstrated by the data presented in Figure 2. Onshore wind turbines are currently the most prevalent renewable energy source in Europe. However, as of 2010, offshore wind turbines and solar power have begun to play a more significant role in overall renewable electrical energy production. It is expected that these proportions will shift in the near future, with offshore wind turbines becoming increasingly prominent due to their larger size and greater power output efficiency, allowing for more efficient windfarms in terms of the ratio of occupied area to power output.

The efficiency of photovoltaic solar panels (PVSP) has been increasing, and their production costs have been reduced as a result of advancements in electronics technology, leading to a surge in popularity. Since the year 2000, the amount of power produced from wind has increased over 20-fold, while the increase for photovoltaics is even more remarkable at a staggering 12,000-fold.
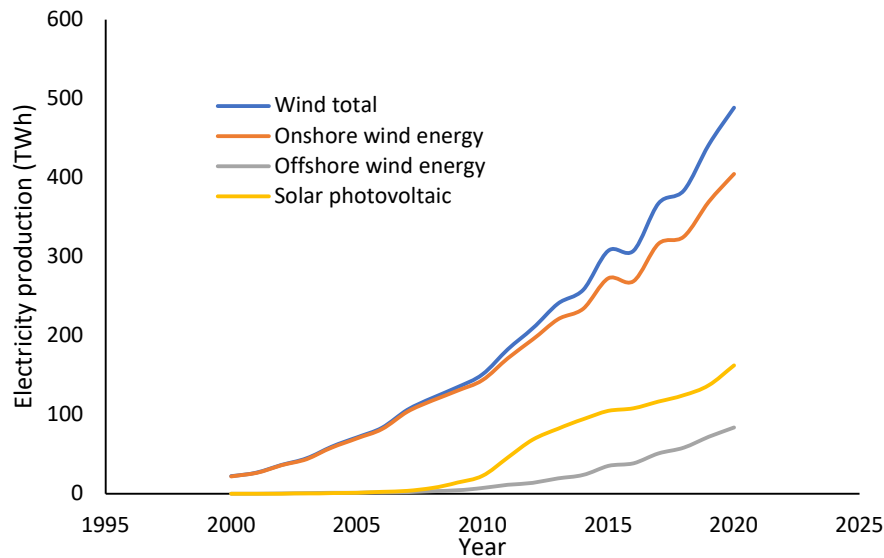
Figure 2 Electrical energy production from selected renewable power sources in Europe in the Years 2000-2020 in Tera Watt hours [12]

Despite the significant increase in the electricity production from PVSP, the overall contribution of solar electricity in the energy sector is still inadequate. In the United States and Europe, solar electricity accounts for slightly less than 4% of total electricity generation, while in Poland, the contribution of solar energy is between 2 and 2.5% (Figure 3) [19].
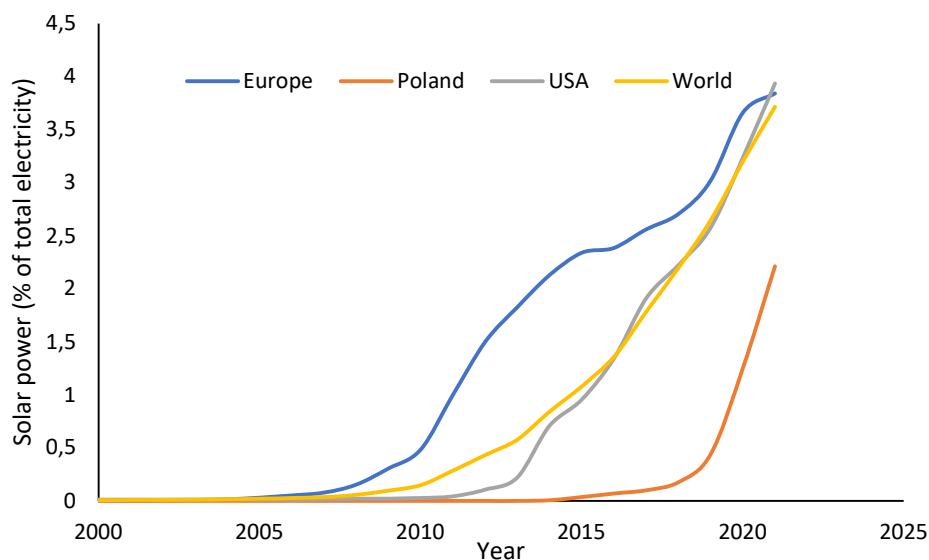
Figure 3 Solar photovoltaic energy as percent of total electric energy produced for a given region [19]

While the contribution of renewable energy sources to global electricity production is presently limited, their increasing prominence in the future is evident from recent trends. However, one

11

of the major drawbacks of all renewable sources of energy is their unpredictable and unstable energy output. To address this issue, energy storage technologies need to be implemented to collect excess energy for later use when direct production is not feasible.

4 Solar Spectrum.

In this study, all computations were conducted using the AM 1.5 global standard IEC 60904-3-Ed2 irradiation [1] which consists of a model solar spectrum with a flux density of 997 W m^{-2}. The spectral irradiance plot is illustrated in Figure 4.
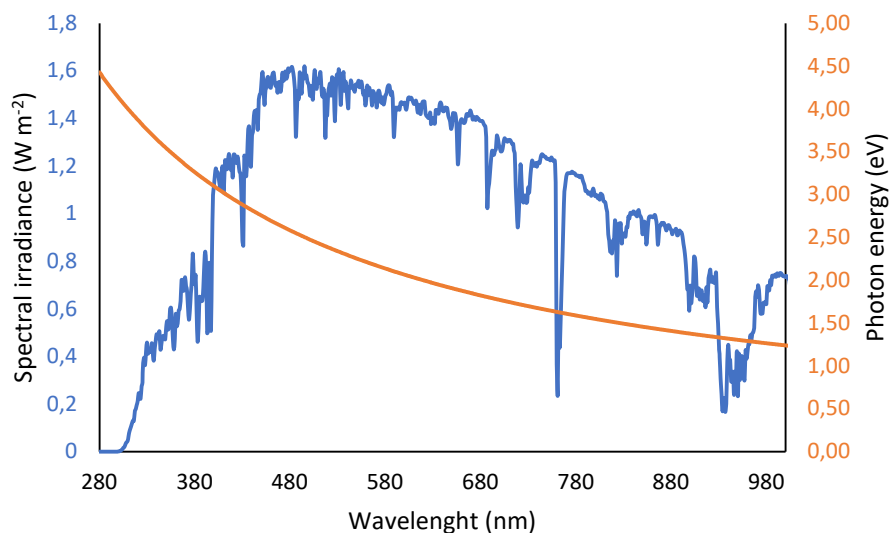
Figure 4 AM 1.5 standard IEC 60904-3-Ed2 solar spectrum with superimposed photon energy [23].

To determine the energy carried by a photon with a particular wavelength, the equation **E = hc/λ** was employed, where E represents the energy carried by a single photon with a specific wavelength measured in electron Volts (eV), h represents Planck's constant, c denotes the speed of light in a vacuum expressed in meters per second (ms^{-1}), and λ represents the wavelength of the photon in micrometers (μm)

5 Photocatalysts - a brief review

Describing photocatalysts in simple terms is challenging as they represent a convergence of several scientific disciplines, including chemistry, physics, electronics, mechanical engineering, nanotechnology, and material science. To fully appreciate their nature, it is necessary to understand how they work and what distinguishes them from conventional catalysts.

Firstly, catalysts are substances that lower the activation energy required for a chemical reaction to proceed without being consumed in the reaction. As a result, the reaction rate increases, and the reaction can occur under more favorable conditions. Chemical reactions can be classified based on the exchange of energy during the process. If energy is absorbed during the reaction, it is endoergic, while energy release characterizes exoergic reactions.

Many critical chemical processes for human civilization, such as CO_2 conversion into hydrocarbons or organic pollutant mineralization, are endoergic, necessitating an input of energy. Currently, available energy sources include fossil fuels, nuclear power, and renewable sources. However, using natural fossil hydrocarbons to produce synthetic hydrocarbons or hydrogen is not efficient, and only renewable energy sources are suitable for fuel production and organic pollutant breakdown The technology of photocatalytic hydrogen production [15] is one of the most promising techniques of obtaining clean energy via direct use of sunlight.

Each photocatalyst is based on at least one semiconductor and functions by using absorbed photon energy to transfer an electron from the valence to the conduction band. The electron-hole pair generated during this process is then utilized for a redox reaction, as illustrated in Figure 5.
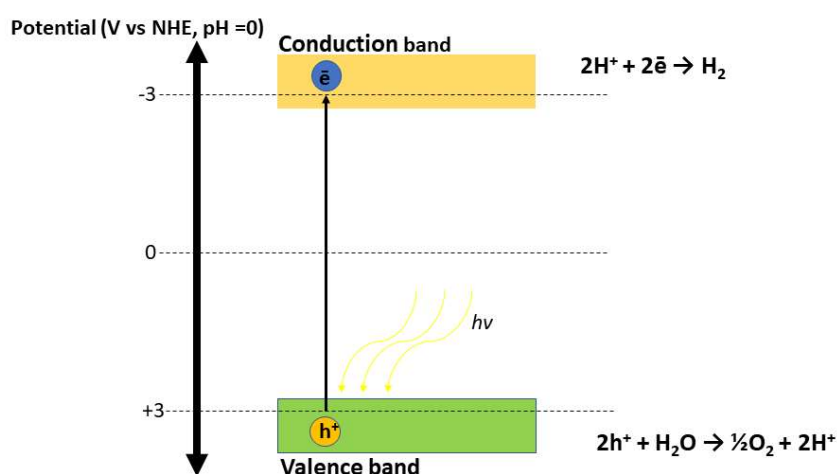

Figure 5. Schematic depiction of the photocatalysts working principle with exemplary reactions

Recent advances in photocatalyst design have focused on improving stability, efficiency, and photosensitivity, resulting in the modification of simple photocatalysts into complex nanodevices. These modern photocatalysts exhibit intricate morphologies and internal structures, with different chemical compositions serving distinct functions. The design process for these photocatalysts frequently involves doping the crystal structure of semiconductors with heteroatoms, synthesizing particles with specific morphologies, and modifying their surfaces with cocatalysts, including metals, quantum dots, nanocarbon structures, and organic sensitizers [24-26]. Current research on photocatalyst design emphasizes semiconductors with surface modifications. One popular modification technique involves decorating the surface of semiconductors with metal nanoparticles, which can greatly enhance photoactivity by increasing photosensitivity, enlarging the photocatalyst's surface area, and acting as electron conduits to prevent electron-hole recombination. However, the use of metals in photocatalyst design can be problematic due to the toxicity of heavy metals or the scarcity and high cost of noble metals. The widespread application of these materials may pose difficulties, even if they ensure adequate catalyst performance. Additionally, the introduction of elemental metallic contaminants to the environment can result in permanent soil contamination, as current soil purification methods are insufficient for removing these contaminants.

An alternative solution may lie in graphene, which exhibits properties similar to metals while being a metal-free, fully synthetic, and fully degradable organic substance [27]. Graphene can be produced in unlimited quantities at low cost, making it a promising candidate for enhancing photoactivity and even serving as a photocatalyst on its own. The potential of graphene in photocatalyst design will be discussed further in subsequent sections of this work.

5.1. Photocatalyst's applications

Photocatalysts have various applications, but two primary applications are widely used, which include (1) conversion of solar energy into hydrogen (or other energy carriers or fuels), and (2) removal of organic pollutants from water or air through photocatalytic mineralization. Therefore, to investigate these basic model applications, two model photocatalysts have been selected in this study, including (1) TiO_2 for hydrogen evolution and (2) Ag_3PO_4 for water purification. The investigation focuses on their usage and scalable production methods

5.1.1. Solar-driven hydrogen production (SDHP)

"Photocatalysts have become increasingly popular due to their ability to perform various tasks, including solar-driven hydrogen production (SDHP) and the purification of water or air via photocatalytic mineralization of organic pollutants. SDHP involves the use of solar radiation to split water molecules into their elemental components and obtain H_2 and O_2, as represented by the following equation:

$$2H_2O \rightarrow 4e^- + 4H^+ + O_2.$$
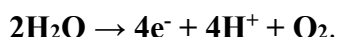
This process can be achieved through various methods, including photochemical (PC), photoelectrochemical (PEC), and photovoltaic-electrochemical (PV-EC). In the PC method, hydrogen is generated directly on the surface of the photocatalyst, which is immersed in liquid or gaseous water and exposed to irradiation. The bandgap of any photocatalyst capable of water splitting by itself must be greater than 1.23 eV with bandgap edges placed below 0 V and above 1.23 V in relation to the normal hydrogen electrode (NHE) at pH=0. On the other hand, PEC involves the use of two photosensitive semiconductor-based electrodes, one for each half of the water-splitting reaction, resulting in the separate collection of oxygen and hydrogen. Finally, in PV-EC, the process of water splitting is achieved through simple water electrolysis with the use of an external power source in the form of a photovoltaic cell, allowing for the separate collection of products but introducing energy loss through electrical resistance of wires and other components.

This work mainly focuses on the PC hydrogen evolution methods, with the other methods serving as a reference point to assess the efficiency and viability of the PC method's broad use. The maximal theoretical STH efficiency of the SDHP processes can be calculated based on the solar radiation spectrum, assuming the bandgap of the used semiconductors is known. The photon energy calculation indicates that photons of λ<1000 nm may be utilized for photoinduced water splitting as they carry above 1.23 eV. This covers the whole visible and near-infrared solar spectrum. Assuming that all photons of energy equal to or higher than a given photocatalyst's bandgap can transfer an electron from the valence to the conduction band, the maximal theoretical efficiency can be calculated using the following formula:

$$STH = (jsc\mathit{\Delta G}\eta F)/P_{solar}$$

Where STH is the maximal theoretically possible Solar To Hydrogen efficiency (%), jsc is the short circuit photocurrent density (mA cm^{-2}), ΔG is the thermodynamic water splitting potential at 25ºC equal to 1.23 V, ηF is the Faradaic coefficient for hydrogen production, assumed to be equal to 1 in this calculation, and P$_{solar}$ is the total power of the AM 1.5 solar spectrum (99.7 mW cm^{-2}). It is worth noting that the solar power taken into calculations was the total power of the solar spectrum stretching from 280 to 4500 nm, even though photons of λ>1000 nm are unable to facilitate water splitting. The maximal theoretical STH efficiencies of the chosen semiconductors, TiO$_2$ for hydrogen evolution and Ag$_3$PO$_4$ for water purification, have been investigated and their use and scalable production methods have been analyzed in this work. All the presented photocatalysts have a bandgap exceeding 1.23 and band edge positions allowing for water splitting, as presented in Figure 6.
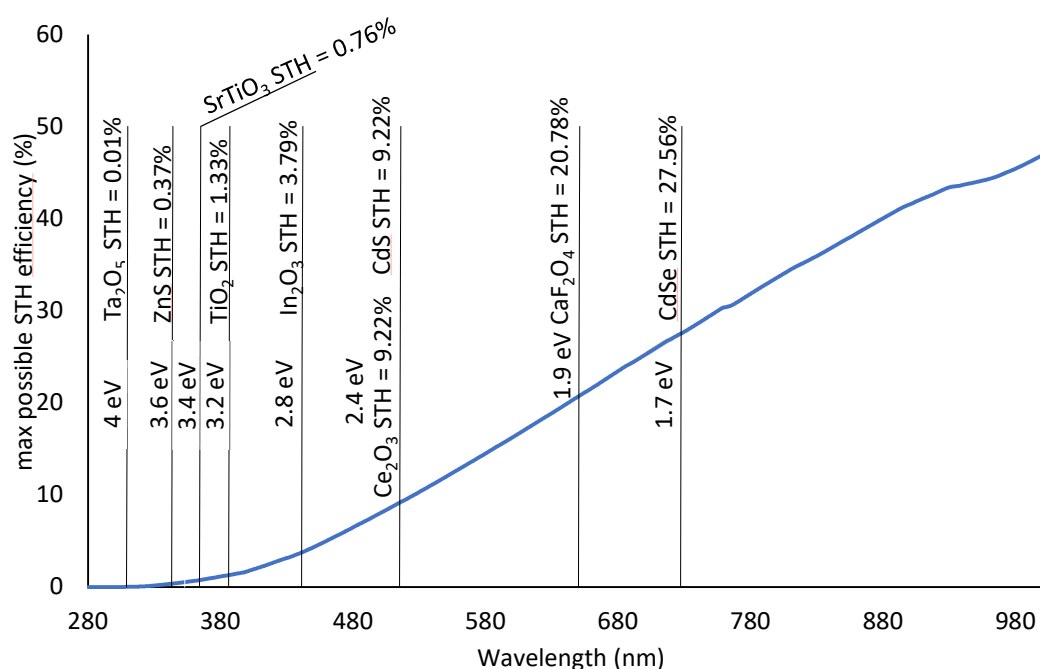
Figure 6 Maximal theoretical solar to hydrogen (STH) efficiency (blue line) with some exemplary photocatalyst's theoretical efficiencies marked (results calculated according to the method described by Chen et. al. [28])

In practice, determining the efficiency of a photocatalyst is a challenging task. The reason for this is that not all absorbed photons result in the creation of an electron-hole pair, and not all generated pairs initiate a chemical reaction. Furthermore, the efficiency evaluation is often

impeded by the experimental setup, which can affect measurements. Additionally, a lack of standardization in photoactivity and efficiency measurement techniques among researchers further complicates the assessment. Consequently, many efficiency values reported in the scientific literature are unsuitable for comparison since they lack complete information on the methodology used for quantum yield calculations or, at the very least, reliable paper-to-paper comparisons. This issue has been discussed in the scientific literature, notably by Chen and Jaramillo et al. in 2010 [28]. However, it appears to be largely disregarded based on the content of many scientific papers.

Active species scavengers may be utilized to aid in hydrogen evolution and prevent oxygen formation and electron-hole recombination. When oxygen generation is inhibited, this process is known as "hydrogen evolution through water photoconversion," and researchers may not recognize it as genuine water splitting. The use of scavengers is widely described in numerous publications and will not be further explored in this work.

5.1.2. Photocatalytic water purification

Within the realm of environmental sciences, the terms pollution and contamination are often used interchangeably, however they are distinct concepts that should not be confused. Pollution refers to the excess of naturally occurring substances, such as the elevated levels of nitrates in the Baltic Sea. Conversely, contamination arises when the environment contains foreign substances that do not naturally occur in the ecosystem, such as antibiotics, petroleum derivatives, and Persistent Organic Pollutants (POPs). Contamination poses a great threat to the environment, as many of these contaminants are not broken down by natural processes due to their unfamiliarity with the flora and fauna. Because many of these synthetic pollutants are of recent origin, there are no evolutionary metabolic mechanisms that allow organisms to deal with this new threat. As a result, natural waters and soils are increasingly found to contain pharmaceuticals, polycyclic aromatic hydrocarbons, and other pollutants.

One promising solution to this environmental challenge is the use of photocatalysts, which are compounds that can initiate the breakdown of organic pollutants through photodegradation. Photocatalysts create superoxide radicals and hydroxide radicals that degrade organic pollutants into simpler compounds, ultimately resulting in the formation of carbon dioxide and water. Recent studies have explored the use of photocatalysts for the degradation of various pollutants, with advanced projects testing their semi-industrial applications [29-30].

Despite the potential of photocatalysts, the chemical composition of natural environments remains complex and unpredictable. For example, chromophoric dissolved organic matter (CDOM), also known as "yellow substances," is widely present in natural waters and is the final stage of bacterial metabolism of organic matter. CDOM is a complex mixture of organic macromolecules that is devoid of biologically available calories and thus cannot be utilized as a food source for most organisms. This material is naturally degraded photosynthetically. Due to the immense diversity of natural waters and their chemical makeup, it is difficult to compare the performance of photocatalysts. Therefore, researchers typically investigate the degradation of pollutants using model reactions based on simulated pollutants such as phenol or organic dyes. [31-33].

6 Literature review

6.1. General trends in photocatalysts containing graphene

In this section, I present an analysis of available written sources to enhance understanding of the present state of knowledge, trends, and development of photocatalysts and their properties. To this end, Table 1 is included, which lists reviewed publications on semiconductor-based photocatalysts containing graphene or closely related compounds such as graphene oxide or reduced graphene oxide. In order to create a representative sample of the primary research trends, publications were searched using the keywords "photocatalyst" and "graphene" and selected randomly from various publishers.

Table. 1 Sample publications regarding composite semiconductors containing graphene

Photocatalyst as reported	Model Reaction	Graphene component morphology	Synthesis method	Scalability consideration mentioned	Toxicity consideration mentioned	Reference
$Sr_2Ta_2O_7N_x$ –G	Hydrogen evolution	sheet	photocatalytic reduction of GO	N	N	[34]
Ni doped GO	Hydrogen evolution	sheet	hydrothermal	Y	Y	[35]
RGO-BiOBr	DYE degradation	sheet	hydrothermal	N	N	[36]
ZnO-Graphene	DYE degradation	sheet	hydrothermal	Y	N	[37]
RGOAg	Phenol degradation	sheet	solvothermal	Y	Y	[38]

CuS-rGO	DYE degradation	sheet	hydrothermal	N	N	[39]
TiO$_2$-Graphene Oxide	DYE degradation	sheet	Hummers method + sonication + self assembly method	N	N	[40]
TiO$_2$-Graphene Oxide film	DYE degradation	sheet	modified Hummers	N	N	[41]
Bi$_2$WO$_6$-Graphene	DYE degradation	sheet	hydrothermal	N	N	[42]
c-Bi$_2$MoO$_6$-Graphene	DYE degradation	sheet	hydrothermal	N	N	[43]
WO$_3$ –RGO	DYE degradation	sheet	hydrothermal	N	N	[44]
TiO$_2$-Graphene oxide	DYE degradation	nanosheet	hydrothermal	Y	Y	[45]
RGO-Mn$_3$O$_4$	DYE degradation	sheet	hydrothermal	N	N	[46]
S doped Graphene	Hydrogen evolution	Quantum Dots	hydrothermal synthesis	N	Y	[47]
ZnS-Graphene	DYE degradation	sheet	hydrothermal + microwave assisted	N	N	[48]
Fe$_3$O$_4$-Graphene	DYE removal through adsorption	sheet	solvothermal	N	Y	[49]
TiO$_2$-Graphene	N/A	sheet	solvothermal	N	Y	[50]
P25-Graphene	DYE degradation	sheet	hydrothermal	N	N	[51]
CeO$_2$-RGO	DYE degradation	sheet	dip-molding andultrasound-assistedprocess	N	N	[52]
TiO$_2$-Graphene	DYE degradation	sheet	hydrothermal	N	N	[53]
TiO$_2$-Graphene	DYE degradation	sheet	sonochemical	N	N	[54]
CdS–G	Hydrogen evolution	sheet	solvothermal	N	N	[55]
TiO$_2$-nanorods-Graphene oxide	DYE degradation	sheet	Hummers method	N	Y	[56]

TiO$_2$-nanorods-Graphene oxide	Photocatalytic sterilization of E.coli. / DYE degradation		Sonication + dry freezing	Y	Y	[57]
TiO$_2$-Graphene	DYE degradation	sheet	hydrothermal	N	N	[58]
RGO-CdO	DYE degradation	sheet	hydrothermal	N	N	[59]
CNTs Graphene	DYE degradation	sheets riddled with CNTs	CVD	N	N	[60]
MoS$_2$r-GO	Hydrogen evolution	sheet	pyrolysis of alginic acid	N	N	[61]
P doped Graphene	Hydrogen evolution	sheet	pyrolysis of Modified Alginate	N	N	[62]
N doped Graphene	Hydrogen evolution	sheet	pyrolisys of chitosan	N	N	[63]
Oriented CuO$_2$-N-G films	Hydrogen evolution	sheet	pyrolysis of chitosan	N	N	[64]
Oriented Au-N-G films	Hydrogen evolution	sheet	pyrolysis of chitosan	N	N	[65]
Cu$_3$Se$_2$-rGO	DYE degradation	sheet	co-precipitation	N	N	[66]
RGO-BiPO$_4$	DYE degradation	sheet	solvothermal	N	Y	[67]
ZnO-RGO	DYE degradation	sheet	hydrothermal	N	N	[68]
B doped Graphene	Hydrogen evolution	sheet	graphite annealing with precursor	N	N	[69]
RGO-NiO	DYE degradation	sheet	hydrothermal	N	Y	[70]
RGO/SrTiO$_3$	DYE degradation	sheet	high energy ultrasonication treatment	N	N	[71]
RGO-ZnS	DYE degradation	sheet	hydrothermal	N	N	[72]
SnO$_2$-RGO	DYE degradation	core shell	RGO reduction in N2	N	N	[73]
TiO$_2$-RGO	DYE degradation	sheet	hydrothermal	N	N	[74]

Graphene-TiO_2-MCM-41	degradation of 2-propanol	coating	HT carbonisation of 2,3-dihydroxynaphthalen	N	N	[75]
P25-Graphene oxide	ciprofloxacin degradation	sheet	hydrothermal	N	N	[76]
ZnO-Graphene	DYE degradation	sheet	hydrothermal	N	N	[77]
β-$SnWO_4$-RGO	DYE degradation	sheet	microwave assisted	N	N	[78]
BiOI–RGO	DYE degradation	sheet	hydrothermal	N	N	[79]
Cu_2O-RGO	DYE degradation	sheet	hydrothermal	Y	N	[80]
Ag_2CO_3/RGO	DYE degradation	sheet	hydrothermal	N	N	[81]
RGO–$ZnWO_4$$^{-2}$	DYE degradation	sheet	hydrothermal	N	N	[82]
TiO_2 –G	Hydrogen evolution	sheet	hydrothermal	N	N	[83]
$InNbO_4$ Graphene	DYE degradation	sheet	hydrothermal	N	N	[84]
RGO–$Bi_2WO_6$$^{-3}$	DYE degradation	sheet	hydrothermal	N	N	[85]
$ZnFe_2O_4$-Graphene	DYE degradation	sheet	hydrothermal	N	Y	[86]
TiO_2-Graphene film	DYE degradation / photoelectric sells efficiency	sheet	hydrothermal	Y	N	[87]
TiO_2-Graphene	DYE degradation	sheet	hydrothermal	N	N	[88]
P25-Graphene	DYE degradation	sheet	hydrothermal	N	N	[89]
P25-Graphene	DYE and benzene degradation	sheet	hydrothermal	N	N	[90]
Cu_2SnS_3-RGO	DYE degradation	sheet	hydrothermal	N	N	[91]
GO	Hydrogen evolution	sheet	hydrothermal	N	N	[92]
N doped Graphene	Hydrogen evolution	Quantum Dots	graphite annealing with precursor	Y	N	[93]
ZnSe/RGO	DYE degradation	sheet	hydrothermal	N	N	[94]
Cu-Graphene	DYE degradation	sheet	hydrothermal	N	N	[95]

Au-Graphene	DYE degradation	sheet	hydrothermal	N	N	[96]
RGO-Bi$_2$S$_3$	DYE degradation	sheet	solvothermal	Y	N	[97]
BiVO$_4$ /RGO30/	DYE degradation	sheet	microwave assisted	N	N	[98]
RGO-Ag$_2$Se	DYE degradation	sheet	hydrothermal	Y	N	[99]
CdS–rGO	DYE degradation	sheet	hydrothermal	N	N	[100]
α-Fe$_2$O$_3$-RGO	DYE degradation	sheet	hydrothermal	N	N	[101]

This section, presents an analysis of available literature sources regarding the application of graphene and closely related materials in photocatalysis. The results demonstrate that such materials have attracted considerable interest within the scientific community. Of the reviewed publications, approximately 80% focused on the use of graphene-modified photocatalysts for water purification, using dyes or hydrocarbons as model pollutants. The second most frequent topic investigated was photoinduced hydrogen evolution from water conversion or water splitting.

However, it is apparent from the literature analysis that the research in this field is still in its early stages. Only 15% of the publications considered synthesis scalability, and 16% paid attention to the environmental toxicity of the investigated photocatalysts, with only 6% considering both. The majority of research still focuses on the intrinsic mechanisms governing photocatalytic reactions and their efficiency. Furthermore, many of the investigated composites contain expensive or environmentally hazardous metals such as platinum, gold, cadmium, zinc, nickel, or cobalt, making them unsuitable for large-scale applications, particularly in water purification, where such substances can be hazardous for the environment.

This lack of certain guidelines for designing environmentally safe and easily scalable photocatalysts is clearly evident. Additionally, most of the publications focus on graphene in the form of sheets or nanosheets, with photocatalysts typically obtained by hydrothermal methods. Although useful in small laboratory scales, these methods have little potential for scaling up to the industrial level as they require expensive and sometimes toxic chemicals and are laborious multi-step processes. Furthermore, almost all photocatalysts exhibit a similar morphology, with the graphene component utilized in the form of sheets with semiconductors "sprinkled" on their surface. Therefore, it is reasonable to suggest that the next logical step in

research should be the investigation of semiconductors with different morphologies and the exploration of alternative synthesis methods (especially those allowing easy scale-up).

6.2. Photocatalysts for hydrogen evolution – efficiency and composition

In the realm of photocatalysis, photoinduced hydrogen evolution has been garnering significant attention in recent scientific literature. Table 2 presents a compilation of photocatalysts specifically designed for photoinduced hydrogen evolution from either water splitting or water photoconversion. The table includes information on the reported efficiencies of the photocatalysts, the types of light sources employed, and the cocatalysts utilized.

Table. 2 Catalysts for photoinduced water splitting – literature sample

Metal of the cocatalyst or dopants	Catalyst (as reported)	Lamp kind	Lamp power (W)	Efficiency (mmol H_2 h^{-1} g^{-1})	Synthesis method	Reference
Au	Au–TiO_2–rGO	LED	12	0.296	Hydrothermal	[102]
Au	Au/TiO_2 (P25)-gC_3N_4	Hg	150	0.419	Thermal polycondensation	[103]
Au	Au/TiO_2-gC_3N_4	Hg	150	0.57	Sol–gel procedure and calcination	[104]
Ag	Ag–TiO_2/SiO_2	Xe	150	0.738	Hydrothermal	[105]
Pt	Pt/Sn_3O_4	Xe	300	0.01667	Hydrothermal	[106]
Au	Au/$InVO_4$	Xe	300	0.1167	Hydrothermal	[107]
Pt	Pt/CoO_x/TiO_2	Xe	300	0.2759	Atomic layer deposition with assisted template	[108]
Pd	Pd-CdS/g-C_3N_4	Xe	300	0.293	Hydrothermal	[109]
Au	Au/$BiVO_4$/g-C_3N_4	Xe	300	0.41	Calcination	[110]
Au	Au/TiO_2/RuO_2	Xe	300	0.527	Sol-gel method	[111]

Pt	Pt/TpPa-1, $C_3N–Pt–Cl_2$	Xe	300	0.719	Integration	[112]
Rh	$Rh/CuGa_3S_5$	Xe	300	1	Hydrothermal	[113]
Pd	$Pd/2D\ C_3N_4$	Xe	300	1.2086	Hydrothermal	[114]
Pt	$g\text{-}C_3N_4$ (pCN) Pt	Xe	300	2.138	Calcination	[115]
Pt	Pt-$CuS/ZnIn_2S_4$	Xe	300	4	Assisted hydrothermal	[116]
Pt	Pt/black $TiO_{2\text{-}x}$	Xe	300	5.2	Impregnation	[117]
Ru	Ru atoms/multi-edged TiO_2 spheres	Xe	300	7.2	Solvothermal	[118]
Ag	$Ag\text{-}ZnIn_2S_4$	Xe	300	7.3	Hydrothermal	[119]
Pt	$Co\text{-}P/Bi\text{-}La_2Ti_2O_7$ nanosheet/Pt	Xe	300	8	Hydrothermal	[120]
Pt	$Pt/O\text{-}g\text{-}C_3N_4$	Xe	300	8.875	Thermal oxidation	[121]
Au	$TiO_2\ \text{–Au}$	Xe	300	12.44	Electrospinning (ES) combined with subsequent calcination	[122]
Pt	Pt/TiO_2	Xe	300	21.9	Deposition precipitation	[123]
Pt	Pt atoms on defective TiO_2	Xe	300	52.7	Hydrothermal	[124]
Pt	Pt/CdS nanowires	Xe	350	0.01606	Solvothermal	[125]
Ag	$CdS\text{-}Ag_3PO_4$	Xe	350	6.6	Solvothermal	[126]
Pt	Pt/TiO_2 nanosheets	Xe	350	16.68	Hydrothermal	[127]
Ru	$RuO_2/BaCeO_3$	Hg	400	0.059	Pechini-type process	[128]
Ru	RuO_2/CeO_2 :Sr	Hg	400	0.1	Hydrothermal	[129]
Pt	Pt/Ta_3N_5	Hg	450	0.136	Hydrothermal	[130]
Ag	$Ag/CaTiO_3$	Hg	450	0.167	Hydrothermal	[131]

Ag	Ag_2S / MoS_2	Xe	450	0.628	In situ growth	[132]
Rh	Rh/Cr_2O_3 shell)/(Ga x Zn x)(N x O x)	Hg	450	1.16	In situ photodeposition method	[133]
Pt	TiO_2 /Pt/rGO	Xe	500	0.876	Modified Hummers method	[134]
Rh	Rh-Ti_3NS	Xe	500	1.97	Solid-state reaction method	[135]
Rh	Rh-doped TiO_2	Xe	500	2.55	Thermal annealing	[136]
Rh	Rh-doped $Ca_2Nb_3O_{10}$	Xe	500	77	Thermal annealing	[137]

The scientific literature concerning photocatalysts for photoinduced hydrogen evolution is a popular area of research. Table 2 presents a compilation of photocatalysts used for photoinduced hydrogen evolution from water splitting or water photoconversion, including their corresponding efficiencies, light source types, and types of cocatalysts utilized.

However, it is important to note that most of the papers reviewed in Table 2 are based on laboratory experiments using a xenon arc lamp, which has a spectrum that is similar to natural sunlight. Despite the fact that all papers included in Table 2 report the lamp type and its power, fewer than 20% of the publications provide information on the surface density of irradiation or the power reaching either the photocatalyst or the reactor's surface. Furthermore, only a minority of authors report the readily calculated Quantum Yield or Apparent Quantum Yield of the photocatalytic process. Reports regarding the lamp's power and construction type have also been largely inconclusive, as there is no correlation between the lamp's power and the energy reaching the photocatalysts across the scientific literature. The relevant data required to verify this claim has been collected in Table 3.

Table. 3 Surface power density, lamp kind, lamp power and efficiency comparison for chosen experiments

Catalyst (as reported)	Lamp kind	Lamp power (W)	Surface power density at the reactor (mW cm^{-2})	Efficiency (mmol H$_2$ h^{-1} g^{-1})	Reference
MoS/TiO$_2$	Xe	300	600	1.6	[138]
MoS$_2$/CdS	Xe	300	50	0.137	[139]
ZnS-MoS$_2$-/GR	Xe	300	125	2.258	[140]
TiO$_2$/MoS$_2$	Xe	300	2.7	2	[141]
MoS$_2$/TiO$_2$	Xe	300	100	0.075	[142]
Pt-Ti/G	Xe	500	100	0.686	[143]
S-ZnIn$_2$S$_4$/MoSe$_2$	Xe	300	254	63.21	[144]
Sb-SnO$_2$	Xe	300	251.4	0.049	[145]
TiO$_2$-GO	Hg-Xe	1000	100	0.12	[146]
Ag-TiO$_2$/Gr	Xe	300	100	0.225	[147]
TiO$_2$/Gr	Xe	500	80	0.0054	[148]
TiO$_2$/Cu/GNP	LED	9.5	20	89.3	[149]
TiO$_2$/Cu/RGO	Xe	150	47	2.9	[150]
TiO$_2$-Cu-C-500-25	Xe	1000	50	2.3	Current work
TiO$_2$/Gr	Xe	300	80	0.74	[151]
TiO$_2$/Gr	Xe	500	150	0.09	[152]
TiO$_2$/Cu/Gr	Xe	300	220	22	[153]

As demonstrated in Figure 7, there is no correlation between the overall power of the lamp used in an experiment and the energy actually reaching the photocatalyst (R^2=0.0092).
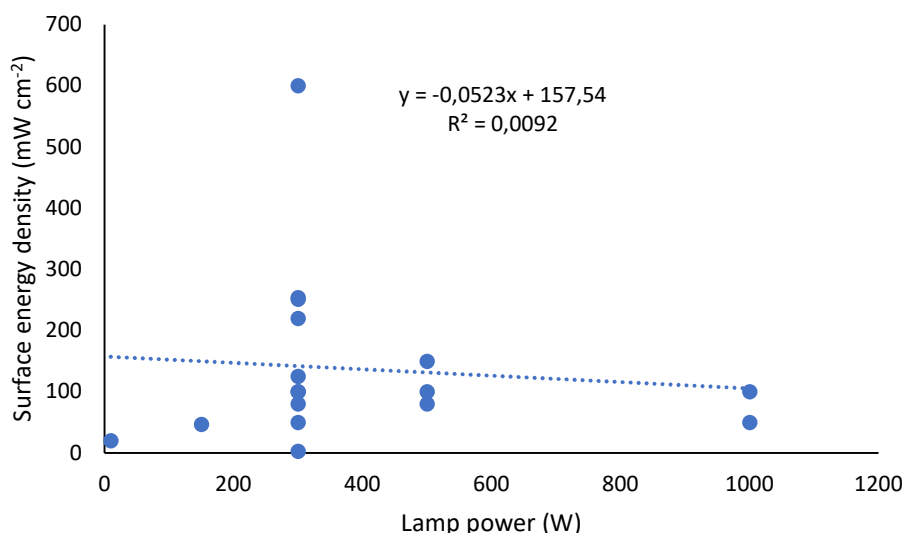
Figure 7 Correlation between the power of the lamp used in chosen experiments and the surface density of energy reaching the photocatalyst

In the absence of sufficient data for conventional Quantum Yield calculations in most of the reviewed papers, an alternative method has been established for estimating the efficiency of the reported photocatalysts. Data from Table 3 was used for the calculation, as the surface density of energy reaching the reactor is necessary. Since the overwhelming majority of experimental photoreactors have a volume of approximately 100 ml, an assumption was made (based on the author's laboratory experience) that photoreactor vessels have a window of approximately 15.7 cm^2, which is the most common window surface among 100 ml sized photoreactors encountered by the author. Assuming this, the efficiency of the photocatalysts was estimated by dividing the power equivalent of the hydrogen obtained in the experiment (expressed in kJ h^{-1} assuming hydrogen energy density of 127 kJ / gram H_2) by the incident power reaching the reactor window (expressed also in kJ h^{-1}):

Efficiency (%) = [(H_2 power equivalent) / (Incident power at the reactor window)] * 100

The term "estimated" is used here because the surface area of the photoreactor window was derived based on "expert judgement" and thus introduces a certain level of error. However, as this information was not reported in the reviewed papers, it was deemed a necessary sacrifice in order to calculate the required information. The results of the estimation are presented in Table 4.

Table. 4 Estimated efficiencies of chosen photocatalysts

Catalyst (as reported)	Lamp kind	Lamp power (W)	Surface power density at the reactor (mW cm^{-2})	Efficiency reported (mmol H$_2$ h^{-1} g^{-1})	Estimated efficiency (%)	Reference
TiO$_2$/Gr	Xe	500	80	0.0054	0	[148]
Sb-SnO$_2$	Xe	300	251.4	0.049	0.01	[145]
MoS$_2$/TiO$_2$	Xe	300	100	0.075	0.03	[142]
TiO$_2$/Gr	Xe	500	150	0.09	0.03	[152]
TiO$_2$-GO	Hg-Xe	1000	100	0.12	0.05	[146]
Ag-TiO$_2$/Gr	Xe	300	100	0.225	0.1	[147]
MoS$_2$/CdS	Xe	300	50	0.137	0.12	[139]
MoS/TiO$_2$	Xe	300	600	1.6	0.12	[138]
Pt-Ti/G	Xe	500	100	0.686	0.31	[143]
TiO$_2$/MoS$_2$	Xe	300	270	2	0.33	[141]
TiO$_2$/Gr	Xe	300	80	0.74	0.41	[151]
ZnS-MoS2-/GR	Xe	300	125	2.258	0.81	[140]
TiO$_2$-Cu-C-500-25	Xe	1000	50	2.3	2.06	Current work
TiO$_2$/Cu/RGO	Xe	150	47	2.9	2.77	[150]
TiO$_2$/Cu/Gr	Xe	300	220	22	4.49	[153]
S-ZnIn$_2$S$_4$/MoSe$_2$	Xe	300	254	63.21	11.18	[144]

Most of the estimated efficiency data falls within the realm of reasonable results and stays in close relation to the maximal theoretical efficiencies calculated earlier. Estimates exceeding 10% should be treated with caution, especially that such high results are seldom encountered in publications. The average efficiency of the obtained results equals 1.4% while the median is as low as 0.2%. This is below the commonly recognized viability threshold of 10% and way lower than the possibilities of PVSP. Surprisingly, there seems to be a strong correlation between the reported efficiencies given in mmol H$_2$ h^{-1} g^{-1} and the estimated efficiencies normalized and expressed as % of harnessed energy. In both cases - with the complete data set and after removing extreme values (Figure 8).
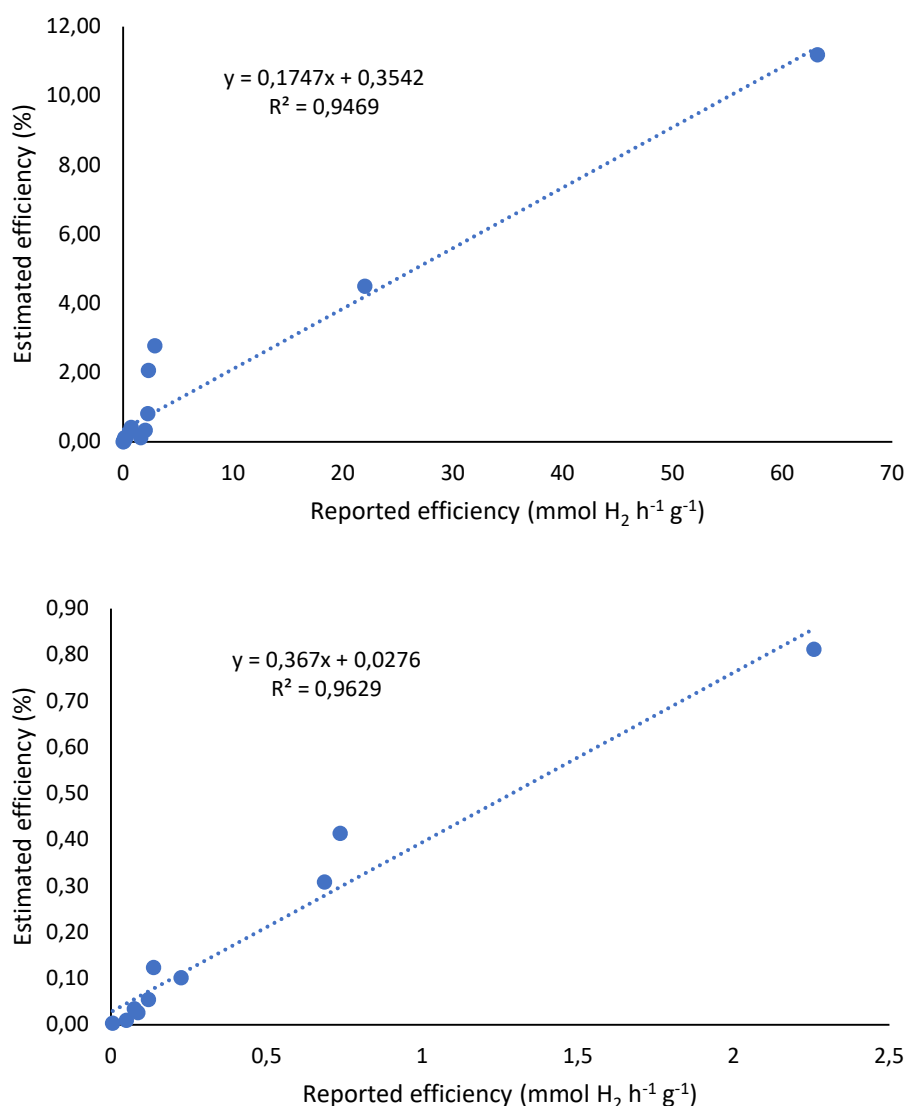
Figure 8 Correlation between estimated and reported efficiencies, upper graph contains complete dataset, lower graph contains dataset without extreme values

The present study analyzed the estimated efficiency data of photocatalysts reported in scientific literature, providing a basis for comparison among different photocatalysts. The estimated efficiencies were obtained by dividing the power equivalent of hydrogen produced in the experiment by the incident power at the reactor window. The obtained efficiency values were within the range of reasonable results and were generally in agreement with the maximal theoretical efficiencies calculated earlier. It should be noted, however, that estimates exceeding 10% should be treated with caution as they are rarely encountered in publications.

The average and median efficiency values of the obtained results were 1.4% and 0.2%, respectively. These values are below the commonly recognized viability threshold of 10% and

are considerably lower than the possibilities of photovoltaic solar panels. Notably, there was a strong correlation between the reported efficiencies given in mmol H_2 h^{-1} g^{-1} and the estimated efficiencies normalized and expressed as a percentage of harnessed energy.

This suggests that a rough comparison of efficiency between different kinds of photocatalysts reported in the literature is possible within the (mmol H_2 h^{-1} g^{-1}) unit. However, it is important to bear in mind that the risk of error is elevated in the absence of reliable normalization data, and that such data should be used with caution. Despite these limitations, the results indicate that photocatalysts containing noble metal-based cocatalysts generally perform better than those containing earth-abundant materials, with the difference in efficiency ranging from 3 to 8 times in favor of metals.

However, it should be noted that the use of noble, heavy, and toxic components increases the cost of production and poses a risk of environmental contamination, which undermines the environmental benefits of the energy source. To illustrate, the cost of one ton of TiO_2 (P25) decorated with 0.01% Pt according to the average market prices of the necessary materials in 2022 would be approximately 32,320 USD, while the same amount of TiO_2 decorated with 1% Cu and covered in 1% graphene would cost 2,823 USD.

Although the cost of graphene is currently high, it is expected to decrease as the production techniques improve and the demand increases. On the other hand, platinum is very expensive and rare, and its abundance in the Earth's crust is minimal. The increased demand for platinum would further elevate its price, making it less feasible for practical applications. Therefore, a balanced approach that considers both the raw efficiency of the photocatalytic process and the environmental and economic aspects of production, environmental risk management, and utilization costs of the spent photocatalytic materials is necessary when designing a viable photocatalyst.

The prices used in the above calculations were derived from leading market online services (metal.com, lme.com, metalary.com, bullionvault.com, bloomberg.com, statista.com, businenninsider.com, cheaptubes.com, asianmetal.com).

7. Summary of the literature review

Based on the literature review, the main focus of photocatalyst research has been on developing efficient photocatalysts and exploring their functional mechanisms. While investigating the latter will always remain crucial, it is evident that the former has now progressed to a new level of evolution. It is my inference that photocatalysts based on toxic metals and noble, expensive, and rare elements will face significant challenges in transitioning from laboratory research to industrial applications. Therefore, it is imperative to incorporate economic and environmental factors into the design of modern photocatalysts to facilitate their industrial applications.

To evaluate the feasibility of producing an economically viable and environmentally friendly photocatalyst, a series of experiments have been devised. The aim is to employ industrial synthesis methods to produce composite photocatalysts containing graphene as a cocatalyst and to assess the viability of this approach.

Numerous researchers have directed their attention towards graphene as a potential alternative to noble metal cocatalysts. This interest is due to the fact that graphene is comprised solely of carbon and exhibits numerous characteristics that make it an attractive substitute for metal cocatalysts. Graphene displays outstanding thermal and electrical conductivity, chemical inertness, excellent mechanical strength, and the ability to increase catalyst surface area and adsorption properties. Furthermore, it can be modified to function as a semiconductor itself [154-155]. Graphene is also frequently utilized in combination with metal-oxide semiconductors and metallic cocatalysts as a modifier and/or cocatalyst [34-101].

Therefore, graphene was selected as the focus of the experimental portion of this research. The primary objective was to investigate the synthesis and application of graphene as a potential cocatalyst.

8. Experimental section

A set of experiments was conducted with a particular emphasis on photoinduced hydrogen evolution and water purification. The primary aim of these experiments was to examine the impact of incorporating graphene on the properties of photocatalysts. The experiments were designed in accordance with the following guidelines: (i) the method employed for incorporating graphene was to be scalable for industrial application, and (ii) the composition of the photocatalysts was to have minimal toxicity.

8.1. Graphene wrapped copper decorated TiO$_2$ for hydrogen evolution form water photoconversion

8.1.1. Reagents

Laboratory reagents used in this experiment were purchased in Sigma Aldrich – Copper (I) acetate $Cu(CH_3COO)$ and methanol CH_3OH, Degussa – TiO$_2$ in the form of P25 and Linde-gaz – Compressed hydrogen, acetylene and argon.

8.1.2 Photocatalyst synthesis procedure

A novel fluidized bed reactor setup and method were developed exclusively for this experiment, resulting in a patent pending (P.430994 29 08 2019) method and reaction vessel. To the best of my knowledge, using a fluidized bed reactor for graphene synthesis on a semiconductor has not been attempted before, and therefore there was no prior work to base the design of the reaction vessel upon. Figure 9 depicts the vessel, which was designed using a combination of SimFlow Computational Fluid Dynamics Software and a trial-and-error approach. The resulting vessel has a broad gas flow-speed tolerance, allowing for an intuitive estimation of the fluidization gas velocity without additional calculations.

The device consists of high-pressure gas tanks connected to the fluidized bed reactor through Alicat electronic flow regulators, which can regulate gas flow within a range of 1-1000 sccm (cm^3 min^{-1}). The reaction chamber is situated in an oven capable of reaching 1100 ºC. The gas tanks are connected to the flow regulators via pressure reducing valves, and the flow regulators are computer-controlled, ensuring precise administration of the desired amounts of gases to the gas mixer. The resulting gas mixture is then delivered to the reaction chamber within the high-temperature oven. Here, the gas performs two functions – it fluidizes the powdered

semiconductor and, depending on the gas composition, triggers the desired chemical reaction. Finally, after passing through the reaction vessel, the gas is vented through the exhaust. Figure 10 provides a schematic representation of the setup.
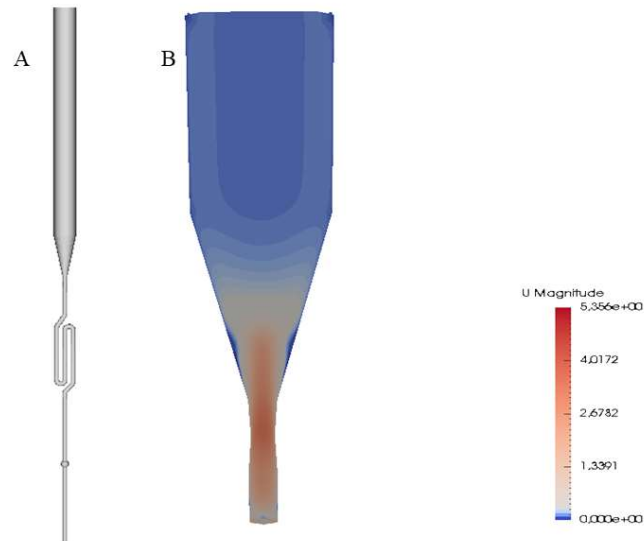

Figure 9. A – General shape of the reaction vessel, B - Schematic illustration of the fluidized bed chamber with gas flow visualization simulated by the SimFlow – Computational Fluid Dynamics Software. The fluidization occurs throughout the region marked by the red color, blue color indicates regions where the gas flow is too slow to carry particles of the semiconductor (Patent pending P.430994 29 08 2019) [162]
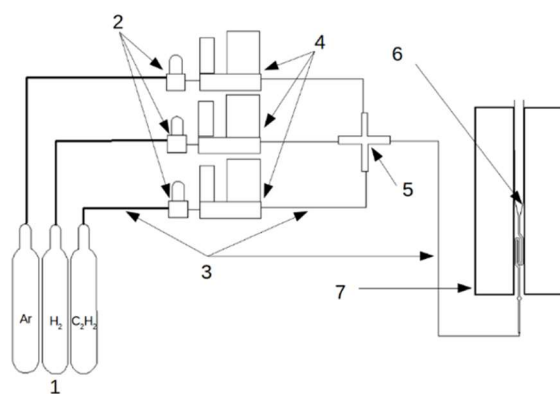
Figure 10. Schematic illustration of the setup used for fabrication of graphene coated photocatalysts 1 –gas tanks, 2 – electro-valves, 3 – gas leads, 4 – gas flow regulators, 5– gas mixer, 6 – fluidized bed reaction chamber, 7 – high temperature oven. (Patent pending P.430994 29 08 2019) [162]

The synthesis of the photocatalyst was initiated by dissolving 0.0572 g of copper (I) acetate in 100 cm^3 of distilled water to create a copper precursor aqueous solution. Then, 2 g of P25 was introduced into the solution and stirred for 60 minutes to ensure that Cu$^+$ ions were adsorbed onto the surface of the titania. The vessel was dried in a dryer at 60 ºC until it was dry, and the resulting mixture was ground in a mortar. Subsequently, 0.5 g of the powder was placed into the reaction chamber of the fluidized bed reactor.

The fluidized bed reactor was operated by flowing argon gas at a rate of 1000 sccm (cm^3 min^{-1}) to induce the fluidization process while the reactor was heated to a temperature between 500 and 850 ºC, depending on the sample. Once the designated temperature was achieved, the gas flow was changed to a 90% argon and 10% hydrogen mix, aimed at reducing the copper precursor to metallic copper. This reduction process took 20 minutes, after which the gas composition was changed to 995 sccm argon and 5 sccm acetylene, which underwent pyrolysis in the high temperature. The duration of the pyrolysis process ranged from 25 to 180 seconds depending on the sample. The pyrolysis process led to graphene synthesis directly on the surface of the metallic copper-decorated semiconductor. After the graphene synthesis was complete, acetylene was shut off, and argon-only flow through the reactor was reinstated. The reaction vessel was allowed to cool down to room temperature, and the procedure was finalized by switching off the argon gas flow.

The fluidized bed reactor setup and method were designed specifically for this experiment using SimFlow – Computational Fluid Dynamics Software and a trial-and-error process. The

resulting vessel is capable of broad gas flow-speed tolerance, allowing for an intuitive estimation of fluidization gas velocity, with no additional calculations needed. The high-pressure gas tanks that are part of the device are connected to the fluidized bed reactor via Alicat electronic flow regulators, with a range of 1-1000 sccm. The reaction chamber is located in an oven capable of reaching 1100 ℃. This method and reaction vessel are patent-pending (P.430994 29 08 2019), and to the best of my knowledge, utilizing a fluidized bed reactor for graphene synthesis on a semiconductor has not been attempted before.

Figure 11 provides a visual representation of the entire process.
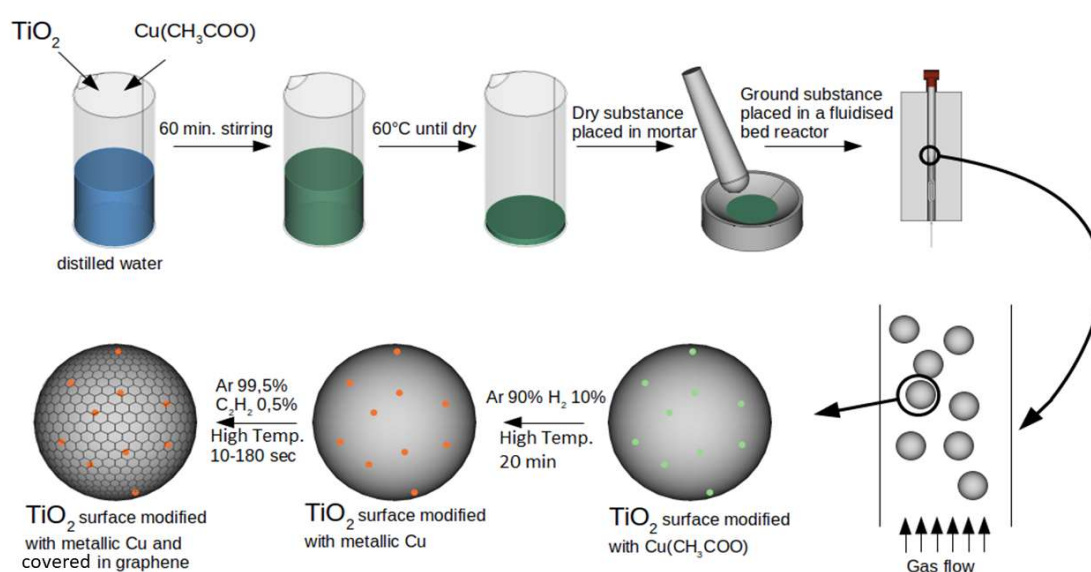
Figure 11. synthesis procedure of TiO_2-Cu-C material [162]

8.1.3. Characterization

The materials obtained in this study underwent a range of measurements and imaging techniques. The morphology of the materials was analyzed through the use of SEM and TEM electron microscopy, conducted with JEOL JSM 7000 and FEI Europe Tecnai F200 X-Twin, respectively. However, due to resource constraints, only a select few samples underwent TEM imaging, XRD, and XPS analysis. All samples were subjected to Raman spectroscopy, collected with a DXR tm3 Thermo Fisher Scientific spectroscope with 532 nm laser. Powder X-ray diffraction (pXRD) was performed using the Burker B2 Phaser diffractometer with Cu Kα radiation and LynxEye-XE detector. LeBail refinement of the XRD data for rutile and anatase

was carried out using a PHI 5000 Versa Probe (ULVAC-PHI) spectrometer with monochromatic Al Kα radiation (hν = 1486.6 eV) at a spot size of 100 μm, 25W, 15V. High resolution XPS spectra were collected using a hemispherical analyzer, and Casa XPS software was utilized for data evaluation. The HR XPS spectra were deconvoluted using Shirley background and a Gaussian peak shape with 30% Lorentzian character. A standard UV-VIS spectrophotometer UV 2600 Shimadzu was used to obtain sample spectra, with BaSO4 used as a reference during the scanning of samples in powder form. A depiction of the various measurements and imaging techniques can be seen in Figure 12.
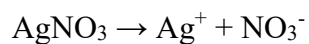
8.1.4. Photoactivity

The photoactivity of the catalyst was tested under controlled conditions using a 1000W xenon lamp as the light source, with a UV-VIS intensity of 50mW cm^{-2} at the reactor window surface. The reactors were composed of quartz and had a volume of 100 mL, containing 80 cm^3 of a 10% methanol solution in distilled water, and 100 mg of the catalyst. The mixture was stirred continuously throughout the entire process, and a rubber septum was utilized to seal the reactor, enabling sampling using a syringe. Nitrogen was introduced into the reactor to replace the atmosphere at the start of each measurement cycle, and the temperature was maintained at 10ºC using a cryostat. The testing procedure involved a 30-minute dark period before each experiment, after which the light was turned on, and the hydrogen concentration was monitored using a TCD detector with Gas Chromatography. The measurements were taken every hour over a three-hour period.

8.2. Ag$_3$PO$_4$ modified with graphene via plasma sputtering

8.2.1. Reagents

The reagents utilized in the experiments were of analytical purity. Silver nitrate, polyvinylpyrrolidone (PVP), and sodium dihydrogen phosphate dihydrate were procured from Sigma Aldrich. Initially, 7.9 grams of PVP were dispersed in 200 ml of deionized water, following which, 4.25 grams of silver nitrate, dissolved in 100 ml of aqueous solution, were added to the first solution and mixed. Subsequently, a solution of 5.68 grams in 200 ml of deionized water was gradually added dropwise to the preceding mixture until a color change to yellow was observed. The final solution was centrifuged, washed several times with deionized water and ethanol, and vacuum-dried at 60 ºC. The reactions occurred as follows:

$$AgNO_3 \rightarrow Ag^+ + NO_3^-$$

$$H_3PO_4 \rightarrow HPO_4^{2-} + H^+ \rightarrow PO_4^{3-} + 2H^+$$

$$PO_4^{3-} + Ag^+ \rightarrow Ag_3PO_4$$
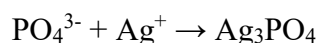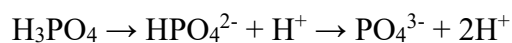
8.2.2. Photocatalyst synthesis procedure

Graphene nanoparticles were deposited onto Ag_3PO_4 through the use of plasma sputtering, and an experimental setup was specifically designed and constructed for this investigation. Standard components were used to create the high voltage power supply, while a custom vacuum chamber was fabricated for the experiment. A glass chamber reactor with a stainless steel substrate electrode (positive) and a graphite target electrode (negative) was used for the sputtering process. The reactor pressure was maintained at 150 mTorr and the potential between the electrodes was set to 2000V. A small sample tray containing 0.3 g of Ag_3PO_4 was positioned 3 cm from the target electrode, directly under the focusing magnet. A series of samples were prepared with sputtering times of 15, 30, 60, 150, and 300 seconds. Each sample underwent the sputtering procedure three times, with thorough homogenization between each session. The reactor assembly is illustrated in Figure 12.
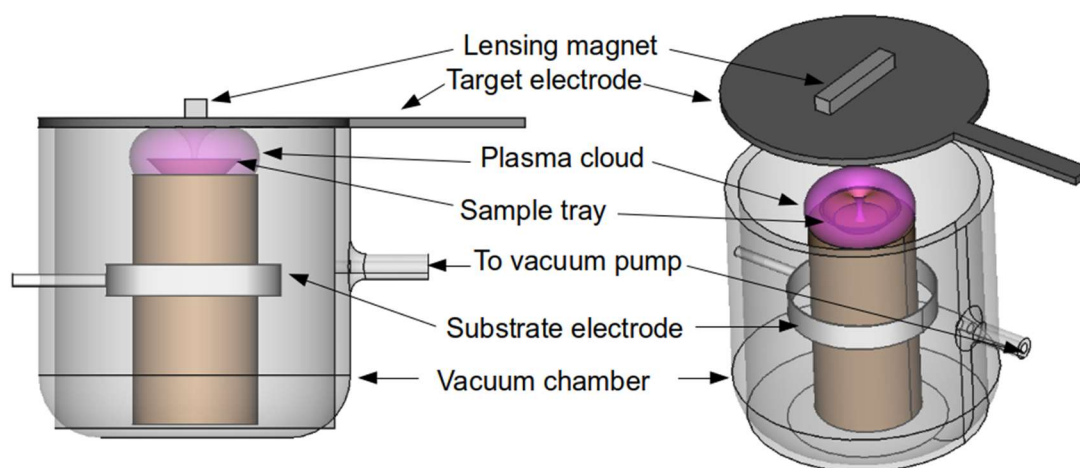

Figure. 12 Scheme of the laboratory scale plasma sputter reactor [177]

8.2.3. Characterization

The materials obtained were subjected to various measurements and imaging techniques. SEM and TEM electron microscopy were used to investigate their morphology. JEOL JSM 7000 and FEI Europe Tecnai F200 X-Twin were employed for SEM and TEM, respectively. Due to limited resources, only a select few samples were subjected to imaging using TEM, XRD and XPS. Raman spectra were collected for all samples using DXR tm3 Thermo Fisher scientific spectroscope with 532 nm laser. Powder X-ray diffraction (pXRD) was done with Burker B2 Phaser diffractometer Cu Kα radiation and LynxEye-XE detector. LeBail refinement of the XRD data for rutile and anatase was performed using a PHI 5000 Versa Probe (ULVAC-PHI) spectrometer with monochromatic Al Kα radiation (hv = 1486.6 eV) with an X-ray at 100 μm spot size, 25W, 15V. High resolution XPS spectra were gathered with the use of hemispherical analyzer, and Casa XPS software was utilized for XPS data evaluation. For deconvolution of the HR XPS spectra, a Shirley background and a Gaussian peak shape with 30% Lorentzian character were utilized. Standard UV-VIS spectrophotometer UV 2600 Shimadzu was used to collect sample spectra. The samples were subjected to scanning in the form of powder with $BaSO_4$ used as reference.

8.2.4. Photoactivity

The Ag_3PO_4-GR photocatalyst was utilized to perform water purification experiments utilizing phenol as a model pollutant. An irradiation source in the form of a 1000 W xenon lamp with a cut-off filter at 455 nm was employed. The Hamamatsu C9536-01 irradiation meter recorded a value of 3 mW cm^{-2} at the reactor's surface. 125 mg of photocatalyst was dispersed in 25 ml of 0.21 mM phenol aqueous solution and placed in the reactor with a quartz window. The mixture was stirred throughout the entire process. For establishing sorption/desorption equilibrium, a period of darkness lasting 30 minutes preceded each irradiation cycle. The reactor was then illuminated, and a 1 ml sample was taken every 5 minutes for a total experiment time of 10 minutes. To confirm a 2% loss of phenol, a blank sample (no photocatalyst) was also conducted. Benzoquinone, a phenol photodegradation byproduct, was analyzed to better understand the experiment's processes. Shimadzu HPLC with Kinetex C18 column and SPD-M20 A diode array detector at 205 nm were used to analyze the samples.

8.2.5. Action Spectra Analysis

The action spectra of two samples, pure Ag_3PO_4 and the most active sample of the series, were investigated. The degradation of phenol and the increase of hydroquinone concentration were studied under monochromatic light at six wavelengths: 455, 460, 480, 505, and 510 nm, carrying photons with energies of 2.72 to 2.43 eV. The experiment used a JASCO RM DF diffraction gating illuminator coupled with a 1000 W xenon lamp as the light source. In the quartz reactor, 25 mg of photocatalyst was suspended in 15 ml of 20 mg dm^{-3} phenol solution and stirred throughout the process. As before, each cycle was preceded by a 30-minute period of darkness for sorption/desorption equilibrium, and a blank sample (no photocatalyst) was also tested. Irradiation time was set to one hour, after which the concentrations of phenol and hydroquinone were analyzed with HPLC.

8.2.6. Role of active species

The method used to determine the active species was previously described by Zwara et al. [173]. To perform the scavenger experiment, the same procedure as the activity tests was followed, with the addition of one of three radical scavengers to the reactor. Each scavenger was tested separately, including p-Benzoquinone (BQ), tert-Butyl alcohol (TBA), and $AgNO_3$, which are known to scavenge superoxide ($O_2^{-\bullet}$), hydroxyl ($^{\bullet}OH$), and electron (e^-) species, respectively. The concentration of the scavengers in the reaction mixture was set to 0.21 mmol dm^{-3}.

9. Results

9.1. Graphene wrapped copper decorated TiO_2 for hydrogen evolution form water photoconversion

The experimental samples are presented in Table 5 in the photoactivity section. The composite material consisted of three components: 1 - the semiconductor (which is the core of the photocatalyst), 2 - a surface modifier based on copper nanoparticles, and 3 - a graphene layer coating. Each sample was assigned an ID code that encoded the synthesis conditions information. The ID code was constructed as follows: <semiconductor (TiO_2)>-<copper based surface modifier (if present, indicated as "Cu")>-<graphene surface modifier (if present, indicated as "C")>-<oven temperature (if applicable) in degrees Celsius>-<graphene synthesis time (if graphene synthesis procedure was employed) in seconds>. For example, a sample with

the ID TiO$_2$-Cu-C-550-30 represents a TiO$_2$ photocatalyst decorated with copper-based nanoparticles and subjected to graphene synthesis at 550°C for 30 seconds, while TiO$_2$-Cu-850 indicates a sample where only copper modification was performed at 850°C and no carbonic layer was synthesized.

Table 5. List of samples synthesized during the experiment.

Sample ID	Synthesis temperature (°C)	Synthesis time (s)
TiO$_2$-Cu-C-500-30	500	30
TiO$_2$- Cu-C-500-25	500	25
TiO$_2$-Cu-550	550	0
TiO$_2$-Cu-550	550	0
TiO$_2$-Cu-C-550-10	550	10
TiO$_2$-Cu-C-550-10	550	10
TiO$_2$-Cu-C-550-15	550	15
TiO$_2$-Cu-C-550-15	550	15
TiO$_2$-Cu-C-550-30	550	30
TiO$_2$-Cu-C-550-30	550	30
TiO$_2$-Cu-C-550-45	550	45
TiO$_2$-Cu-C-550-45	550	45
TiO$_2$-Cu-C-550-60	550	60
TiO$_2$-Cu-C-550-60	550	60
TiO$_2$-Cu-C-550-180	550	180
TiO$_2$-Cu-600	600	0
TiO$_2$-Cu-C-600-30	600	30
TiO$_2$-Cu-C-600-30	600	30
TiO$_2$-Cu-C-600-60	600	60
TiO$_2$-Cu-850	850	0
TiO$_2$-Cu-850	850	0
TiO$_2$-Cu-C-850-60	850	60

9.1.1. Morphology and composition

The SEM images in Figure 13 show that most of the synthesized photocatalyst samples have irregularly-shaped particles, with diameters ranging from 10 to 50 nm, similar to regular P25. However, the samples obtained at higher temperatures (T>800ºC) have much larger grain sizes,

with individual particles exceeding 100 nm. This increase in particle diameter can be attributed to sintering of individual grains, which reduces the contact area between the photocatalyst and its surroundings, and may indirectly impact the overall activity of the sample.
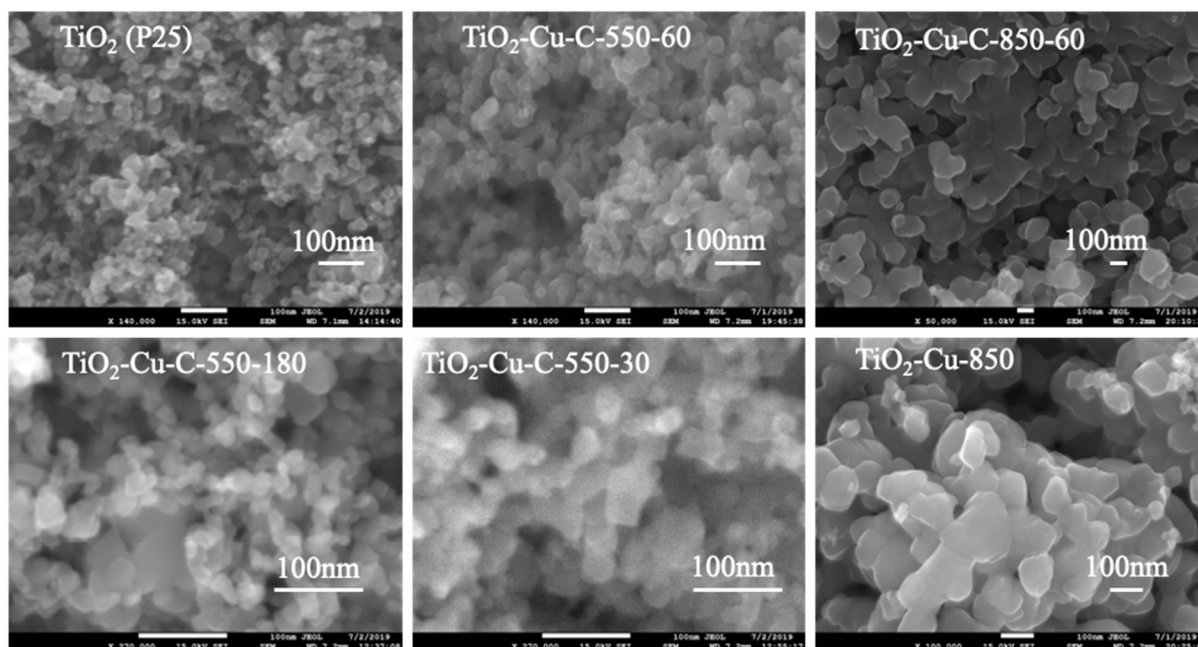

Figure. 13 SEM image of pristine P25 TiO$_2$ and selected samples after graphene synthesis [162]

TEM images presented in Figure 14 provide more detailed information on the morphological features of the synthesized photocatalysts. The TEM images were combined with corresponding Raman spectra, which were normalized against the peak at 1350 cm^{-1} for samples synthesized below 600ºC and against the peak at 1590 cm^{-1} for samples synthesized above 600ºC. The intensity normalization was carried out using the formula:

$$\text{Inorm} = [\text{I} * (100{,}000 * \text{Imax})]/100$$

where Inorm is the normalized intensity, and Imax is the maximal intensity (intensity at 1400 cm^{-1} and 6100 cm^{-1} for samples obtained < 600 ºC and > 600 ºC respectively).
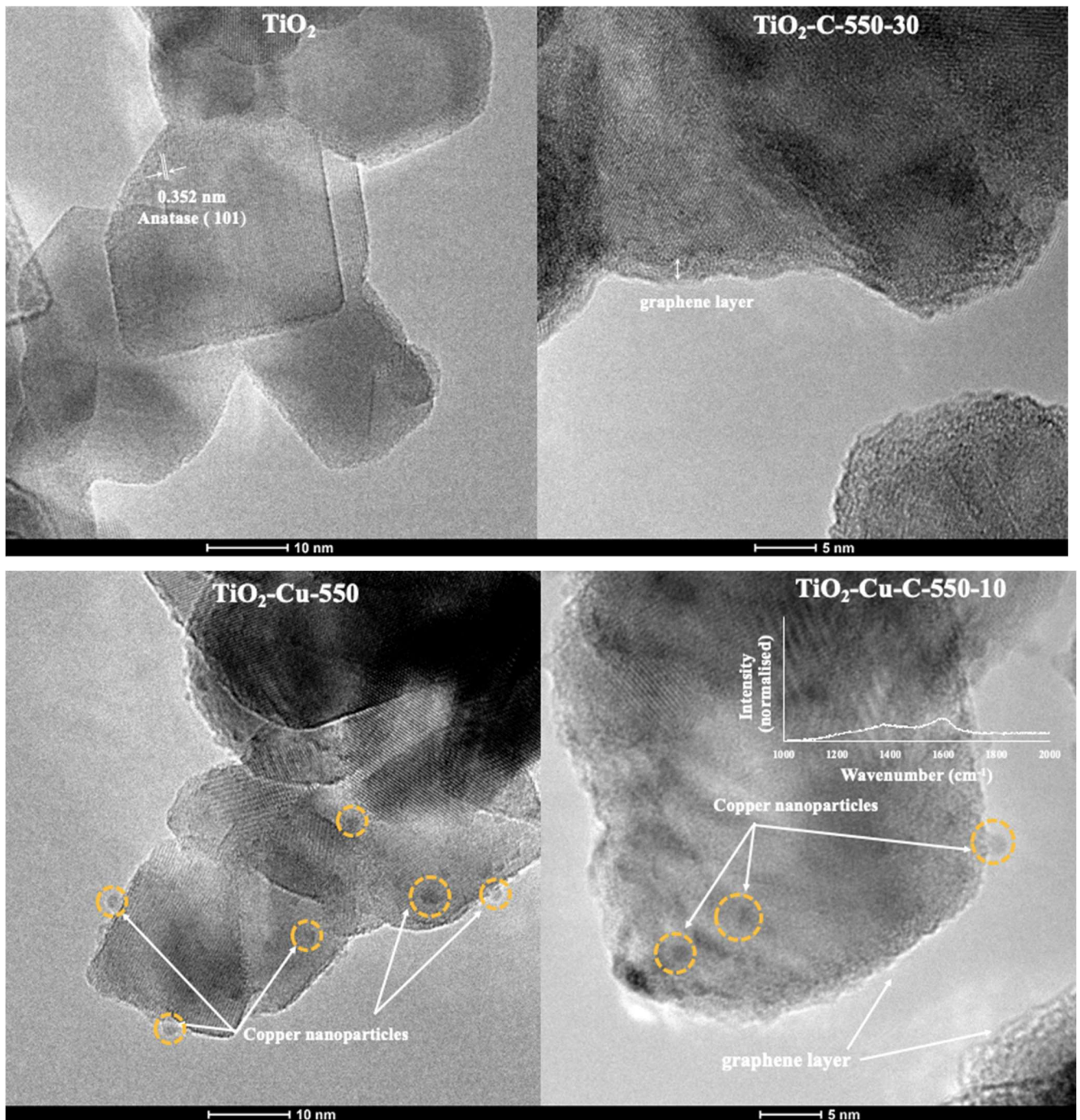
Figure. 14 TEM images of selected samples of investigated photocatalysts with superimposed corresponding Raman spectra. [162]
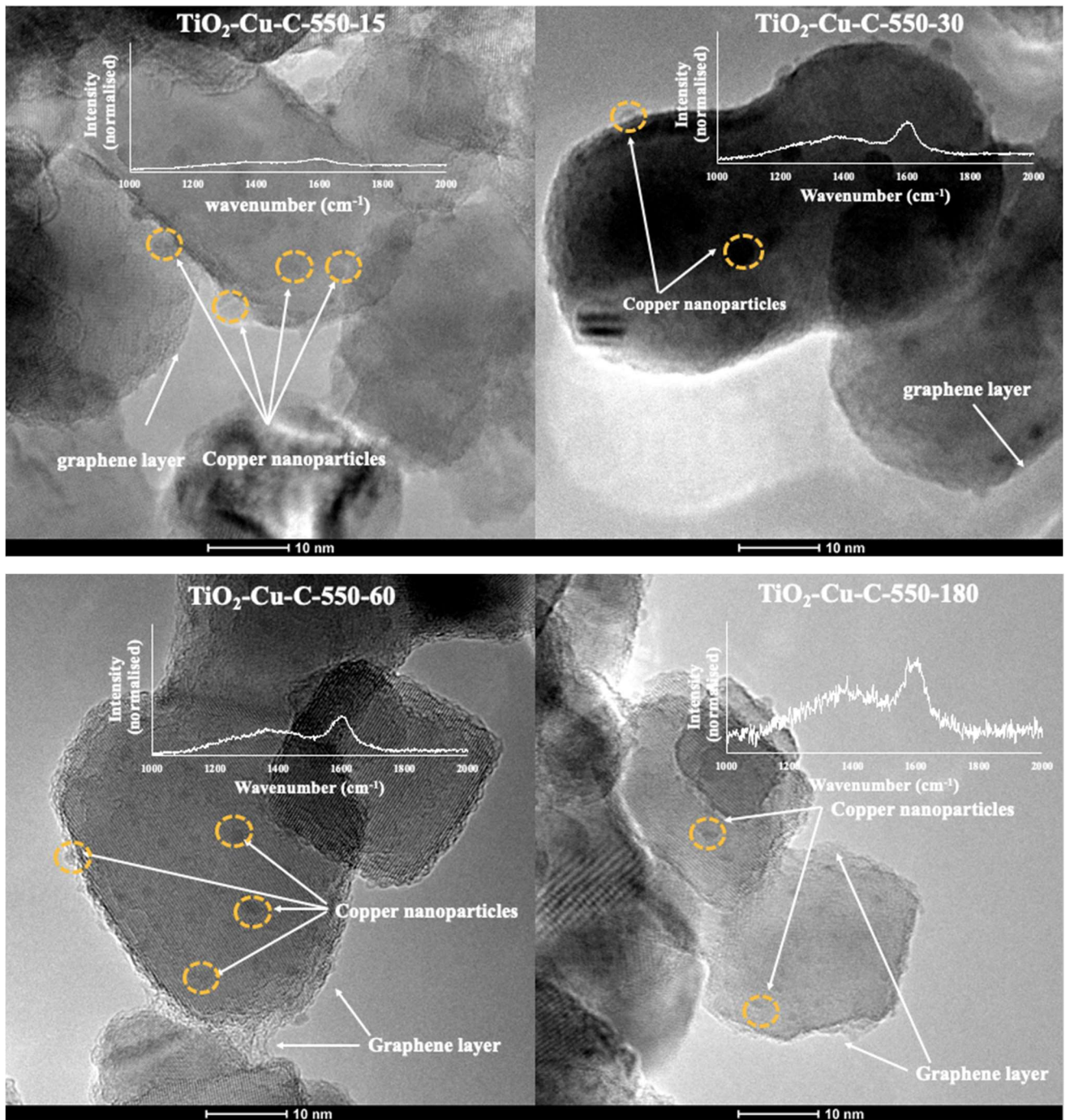
Figure. 14 TEM images of selected samples of investigated photocatalysts with superimposed corresponding Raman spectra. continued [162]
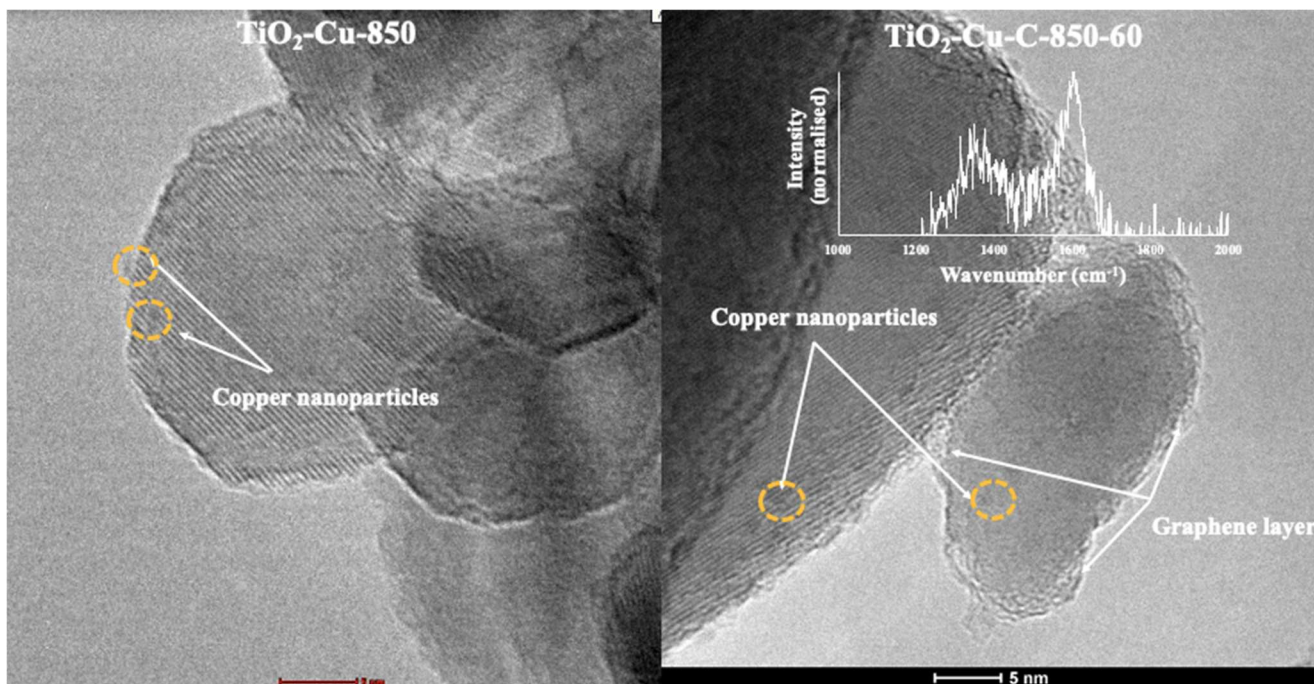
Figure. 14 TEM images of selected samples of investigated photocatalysts with superimposed corresponding Raman spectra. continued [162]

The TEM images confirm the successful construction of the composite material, showing TiO_2 crystals with dark copper nanoparticles distributed irregularly on their surface, and a narrow, few-layered graphene coating visible on the surface of samples where the complete graphene synthesis procedure was performed. Raman spectra analysis confirms the presence of the desired graphene layer, with distinct D and G bands visible at 1350 cm^{-1} and 1590 cm^{-1} respectively. The presence of the D band is attributed to sp3 hybridized carbon atoms, while the G band is attributed to sp2 hybridized carbon atoms, both consistent with the graphene structure. These peaks are only present when graphenic carbon is present in the sample, as evidenced by Raman spectra that returned "flat" at these wavenumbers when no graphene synthesis was attempted, or no copper was present.

Using TEM images, estimates of graphene layer thickness and copper nanoparticle sizes were obtained, with the results presented in Table 6. Simple linear regression analysis showed no clear relationship between synthesis conditions and copper nanoparticle size (~1-2 nm) or graphene layer thickness (~1.1-1.8 nm). However, a weak positive correlation was found between thickness and the G/D band ratio (R^2=0.6557), suggesting that good synthesis

conditions can benefit both the quality and quantity of the graphene layer. Nevertheless, the limited number of cases prohibits drawing any solid conclusions.

Table. 6 TEM and Raman analysis results. Copper nanoparticle size estimation was based upon 10 nanoparticles (TEM imaging), Thickness of graphene layer was estimated with TEM imaging

Sample ID	G/D band ratio	Size of Cu nanoparticles (nm)	Thickness of graphene layer (nm)
TiO_2- Cu-550	-	1.7	-
TiO_2- Cu-850	-	1.6	-
TiO_2- Cu-C-550-10	1.42	1.5	1.2
TiO_2- Cu-C-550-15	1.44	1.7	1.4
TiO_2- Cu-C-550-30	1.77	1.6	1.8
TiO_2- Cu-C-550-60	0.6	2.1	1.1
TiO_2- Cu-C-550-180	1.35	1.3	1.4
TiO_2- Cu-C-850-60	1.41	1.5	1.5

Figure 15 displays the pXRD patterns of the investigated samples. The experimental data points are indicated by dots, while a solid blue line represents a model containing two tetragonal phases of TiO_2, namely, atanase (I 41/amd) and rutile (P42/mnm). To calculate the lattice parameters (compiled in Table 7) and verify the chemical purity of the samples, the profile refinement (LeBail method) was employed. As shown in panels (a)–(d), the starting material (P25) and samples treated at temperatures below 600°C comprise both the anatase and rutile forms of TiO_2. The estimated lattice parameters show almost no difference, with changes not exceeding 0.1%. An approximate calculation of the anatase crystallite size (d) was carried out using the Scherrer equation and the shape of the first (011) reflection, with $2\theta = 25.3$ deg. The rough estimation reveals a value of d~200 Å.

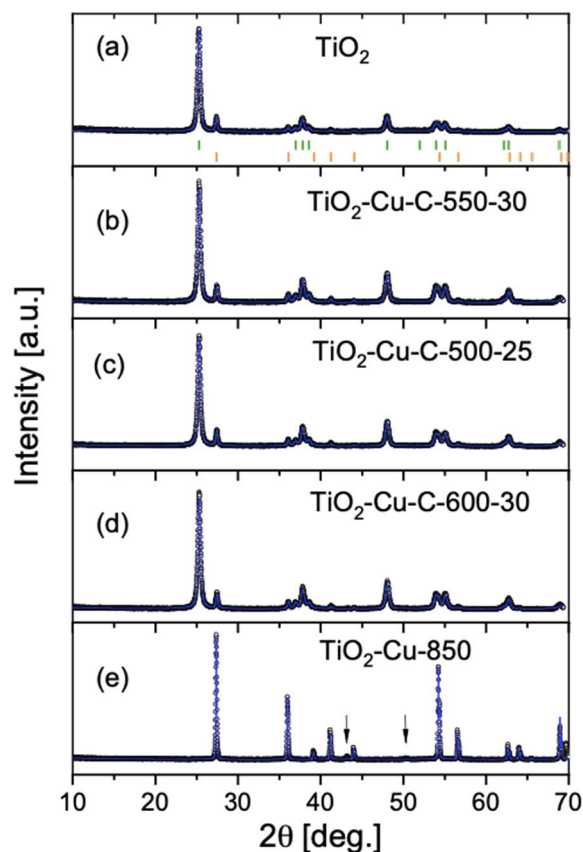**Figure 15.** Powder X-ray diffraction patterns for: (a) starting material TiO_2-P25, (b) TiO_2-Cu-C-550-30, (c) TiO_2-Cu-C-500-25, (d) TiO_2-Cu-C-600-30, (e) TiO_2-Cu-850, a blue line represents a profile refinement (LeBail) with the used TiO_2-anatase and TiO_2 rutile phases. The Bragg peak positions for the first phase are shown by green tick marks, whereas for the second phase by orange tick marks. Arrows show Cu reflections. [162]

Upon increasing the temperature to 800°C, the anatase fully transitions to the rutile form, with the calculated lattice parameters comparable to those obtained for samples treated at lower temperatures. In the TiO_2-Cu 850 sample, two faint Cu reflections were observed (see Figure 15e), marked by arrows. Interestingly, the presence of graphite was not detected, which may be due to the small amount of material in the sample. The lack of graphene traces in the XRD studies is attributed to the close position of the main graphene and anatase peaks, and the very low mass fraction of graphene in the final product.

Table 7. Crystal lattice patterns of selected samples. All values in Å.

Sample ID	Anatase			Rutile		
	a	c	d	a	c	
TiO$_2$	3.7841(2)	9.5036(7)	190	4.5925(5)	2.9565(5)	20%
TiO$_2$-Cu-C-550-30	3.7864(3)	9.5077(9)	190	4.5964(5)	2.9587(4)	17%
TiO$_2$-Cu-C-500-25	3.7858(3)	9.5065(7)	200	4.5955(4)	2.9582(3)	18%
TiO$_2$-Cu-C-600-30	3.7859(3)	9.5058(8)	200	4.5948(6)	2.9587(3)	15%
TiO$_2$-Cu-850	---	---	---	4.5924(1)	2.9598(1)	100%

X-ray photoelectron spectroscopy (XPS) was used to assess the chemical composition of the samples. High-resolution XPS spectra for the Ti2p region revealed a spin-orbit doublet with two peaks around 458.7 eV BE (Ti2p 3/2) and 464.4 eV BE (Ti2p1/2), typical for titanium (IV) oxide [156]. These results are consistent with data obtained using XRD. The XPS spectra of titanium for processed samples were similar to the reference TiO2 sample, indicating no chemical changes in TiO$_2$ during processing. The presence of copper in the analyzed samples was confirmed by XPS studies. Due to spin-orbit coupling, the Cu2p state appeared as a doublet of peaks (2p3/2 and 2p1/2) with two groups of peaks around 933 eV (Cu 2p3/2) and 953 eV (Cu 2p1/2). Deconvolution of Cu2p3/2 peaks suggested the presence of two copper chemical states. The Cu 2p3/2 peak at around 932.7 eV can be attributed to the presence of copper (0) or copper (I) oxide, as both compounds occur in the same XPS spectrum area [212]. This assumption is consistent with data obtained using TEM and XRD, confirming the presence of copper in the samples. However, further differentiation of these substances in the obtained samples is almost impossible due to the overlap of Ti2s peaks and Cu LMM Auger peaks, which are usually used for this purpose [157]. The source of the second Cu 2p3/2 peak, discovered at a higher binding energy (935 eV), could be the primary origin of copper in the samples - copper acetate [158]. This hypothesis also finds support in the high intensity of the C1s peak observed at 289 eV, attributed to the COOR group [213].
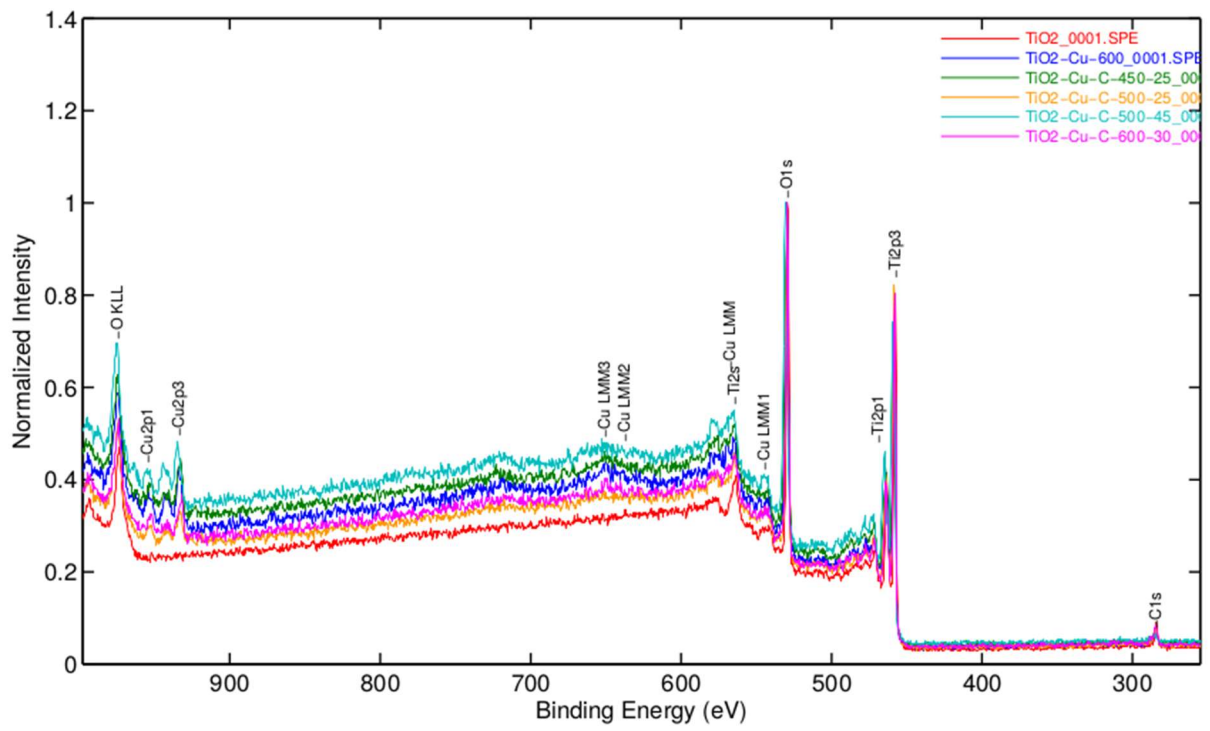
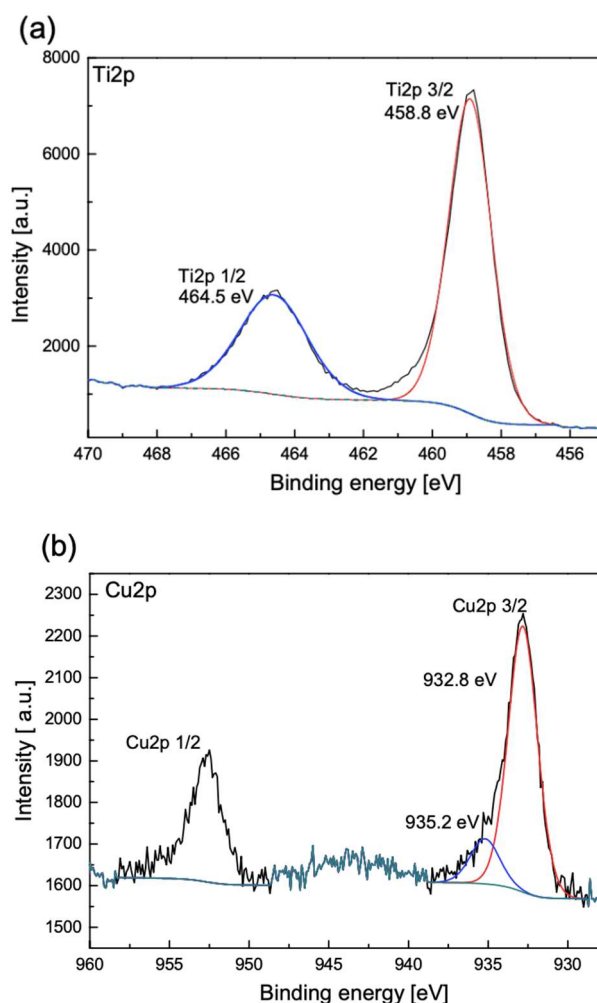**Figure 16**. XPS spectra of investigated samples.

Figure 17. XPS spectra of TiO$_2$-Cu-C-500-25: (a) Ti2P peaks indicative of TiO$_2$ and (b) Cu2P peaks indicative of either Cu^0 or Cu$^{(I)}$. [162]

Figures 16, 17, and 18 show XPS spectra and UV-VIS scans of the studied samples. The presence of a graphene layer caused a slight redshift in the absorption spectra of the samples, possibly related to the hybridization of O2p and C2p atomic orbits, leading to the formation of a new valence zone. The presence of copper also affected the absorption edge shift towards longer wavelengths. In the case of TiO$_2$-Cu-850, without a graphene layer, the redshift was likely associated with the transformation of anatase to rutile induced by exposure to high temperature. Copper-modified samples exhibited a band in the 700-800 nm range, attributed to the d-d electronic transitions of Cu^{2+}, suggesting partial oxidation of the metal. Synthesis conditions indicate that all obtained samples initially contain only metallic copper, but the oxidation of copper deposited on TiO$_2$ may occur rapidly in a normal atmosphere, especially when the graphene layer is incomplete or absent. XPS scans do not allow distinguishing between Cu(0) and Cu(I), suggesting a high probability of coexistence of metallic copper with copper oxides on the surface of TiO$_2$.
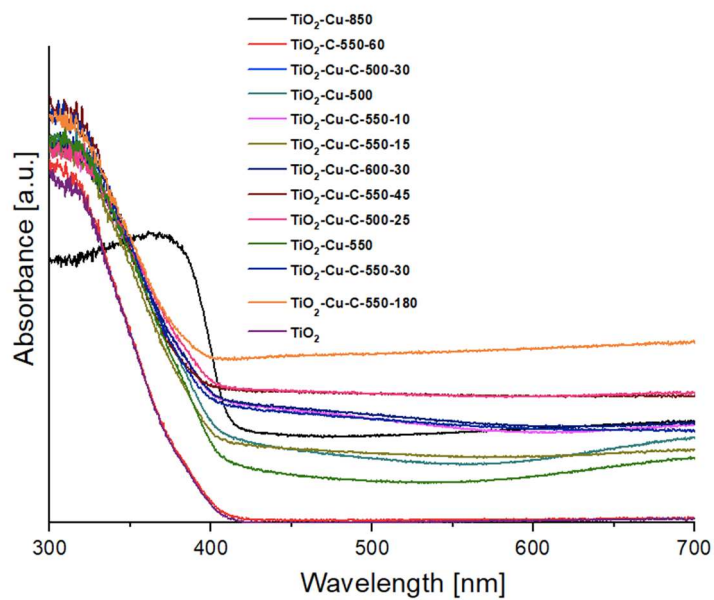
Figure. 18 UV-VIS spectra of selected samples [162]

9.1.2. Photoactivity and stability (hydrogen evolution experiment)

The results of the photoactivity tests have been recalculated to (μmol H_2 h^{-1} $g_{catalyst}^{-1}$) and placed in the table 8.

Table 8. The results of photoactivity experiment with chosen sample synthesis parameters

Sample ID	H_2 h^{-1} g_{cat}^{-1} (μmol)	Graphene synthesis time (s)	Graphene synthesis temperature (°C)
10% methanol	0	0	N/A
TiO_2	86.56	0	N/A
TiO_2- Cu-850	309.7	60	850
TiO_2- Cu-C-850-60	29.92	60	850
TiO_2- Cu-600	1807.05	0	600
TiO_2- Cu-C-600-60	404.7	60	600
TiO_2- Cu-C-600-30	1141.38	30	600
TiO_2- Cu-550	1589.5	0	550
TiO_2- Cu-C-550-180	2065.62	180	550
TiO_2- Cu-C-550-60	2131.11	60	550
TiO_2- Cu-C-550-45	1731.25	45	550
TiO_2- Cu-C-550-30	2152.17	30	550
TiO_2- Cu-C-550-15	1750.19	15	550
TiO_2- Cu-C-550-10	1897.72	10	550
TiO_2-Cu-500	1825.26	0	500
TiO_2- Cu-C-500-30	2151.66	30	500
TiO_2- Cu-C-500-25	2296.27	25	500

The photocatalytic activity of synthesized samples was evaluated by measuring the amount of hydrogen produced during the experiment. A blank sample, containing no photocatalyst, did not exhibit any photoactivity, with zero or below detection limit quantities of hydrogen being produced over the three-hour experiment. The least efficient samples were those synthesized at temperatures of 600ºC and higher (TiO_2-Cu-C-850, TiO_2-Cu-C-850-60, TiO_2-Cu-C-600-60) and pristine TiO_2 (P25). Within samples treated with T > 600ºC, it appears that the generation of graphene covers had a negative effect on photoactivity, as a reverse correlation between the amount of evolved hydrogen and graphene synthesis time occurred. The photocatalysts treated at lower temperatures demonstrated much higher efficiencies. The most likely explanation for this outcome is the sintering that occurs at high temperatures. The individual particles of the photocatalyst obtained at 850ºC are roughly ten times larger in diameter compared to pristine

TiO_2 and materials treated at lower temperatures. Moreover, the anatase to rutile transformation occurring at high temperatures may be detrimental to hydrogen evolution capabilities.

Initially, the exact relationship between synthesis conditions and photocatalyst efficiencies was unclear. Therefore, computer modeling was employed, as described in the following section and in other work [192], which revealed a negative correlation between synthesis times and temperatures and efficiency. Based on the synthesis parameters derived from the computer modeling, the most active sample in the experiment (TiO_2-Cu-500-25) was synthesized, achieving 2296.27 μmol H_2 h^{-1} g_{cat}^{-1}. The most active sample also demonstrated stability, as evidenced by a 15-hour stability experiment conducted in the same manner as the photoactivity experiments, with the only difference being that irradiation lasted for 10 hours (the stability experiment is further discussed in the latter part of this section). The photocatalyst demonstrated stable hydrogen evolution throughout the entire duration of the test.

The most active photocatalyst from this work was compared to results reported by other researchers in table 4. Most of the reported materials had an efficiency below 1%. The photocatalyst from the current work allowed for the production of 2.3 mmol H_2 h^{-1} g_{cat}^{-1}, which correlated to 2.06% power efficiency, placing it high on the tier list and next to very similar composites [150, 153] with 2.77% and 4.49% efficiencies, respectively.

A stability test was performed for the most active sample (TiO_2-Cu-C-500-25) over a 10-hour period. The production of hydrogen continued throughout the whole duration of the experiment until the reactor was filled with ~100% hydrogen, which concluded the test. The sample did not seem to show signs of deterioration, and it is assumed that its structure may be intact even in repeated usage. This finding is in accord with literature data for a similarly structured material [193].
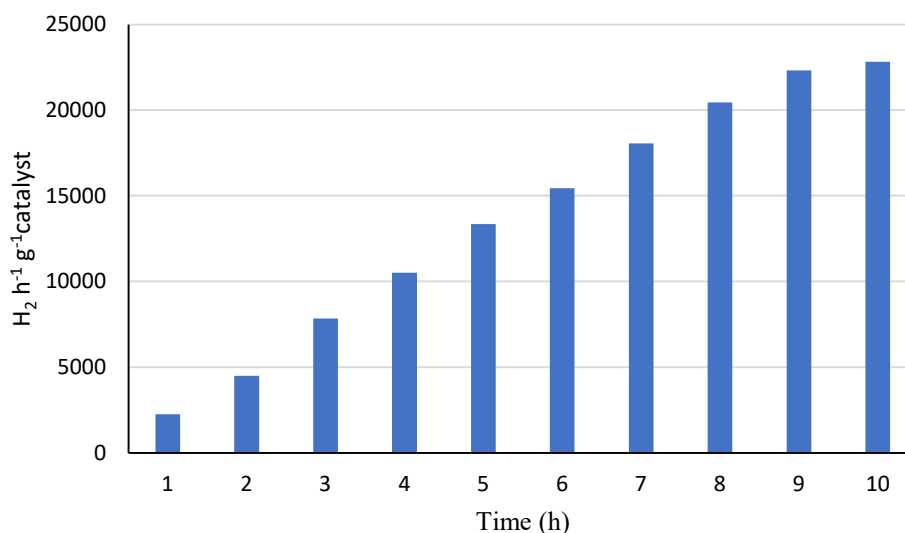
Figure 19. Long term stability results for the most active sample (TiO$_2$-Cu-C-500-25).

9.1.3. Computer aided modelling

In this study, a modeling approach was utilized to explore the impact of different synthesis conditions on the photoactivity of the produced samples. The analysis began with a basic scatter plot (Figure 21a) of the synthesis time versus temperature. The results revealed that samples synthesized at temperatures of 550ºC or less, for a minimum of 30 seconds, exhibited the most optimal hydrogen evolution activity. The conclusions drawn from the scatter plot were further supported by the correlation coefficients computed and displayed on the correlogram (Figure 20).
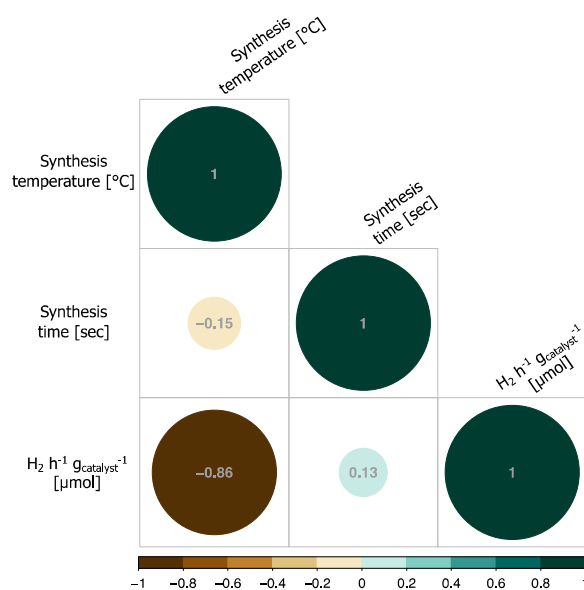
Figure 20. Correlation plot that by definition presents the correlation between any two variables. Color and the size of the circle indicate the strength and direction of a linear relationship: positive correlations are displayed in dark green and negative correlations in brown color. The small circles indicate smallest correlation coefficients, whereas big circles denote highest correlation coefficients [162]

An inverse correlation between synthesis temperature and photoactivity (r=-0.86) was observed, while a weak positive correlation between activity and graphene synthesis time (r=0.13) was detected. To identify the optimal synthesis conditions, a photoactivity experiment produced 21 results, which were divided into a training data set T (15 results) and a validation data set V (6 results). Using a kernel-weighted polynomial regression approach, a computational model was developed to search for a pointwise approximation of an unknown regression function with the help of p-order polynomials (in this case, p=0) for every point of interest. The model considered only the closest few training points to the target point. A detailed description of the model can be found in the relevant literature [164, 165, 166]. To verify the model's predictive capacity, it was trained using the training data set and then tested using the validation data set. To ensure the scientific consistency of the model, several metrics commonly used in computational modeling [167, 168, 169] were calculated, including the determination coefficient (R2), which indicates the goodness-of-fit, and the external validation coefficients (Q2F1, Q2F2, Q2F3) and concordance correlation coefficient (CCC), which indicate the real predictive capacity. The root mean square error (RMSE) was used to estimate the overall error between the experimental data and the model predictions. Table 9 shows that the developed model had high predictive power and goodness-of-fit.

Table 9. Predictive model evaluation metrics. [162]

Quality metrics		Minimum threshold
Goodness-of-fit		
R^2	0.98	> 0.7
$RMSE_T$	47.86	as low as possible
Predictive power		
Q^2_{F1}	0.88	> 0.6
Q^2_{F2}	0.88	> 0.6
Q^2_{F3}	0.92	> 0.6
CCC	0.91	> 0.7
$RMSE_{Ext}$	193.68	as low as possible
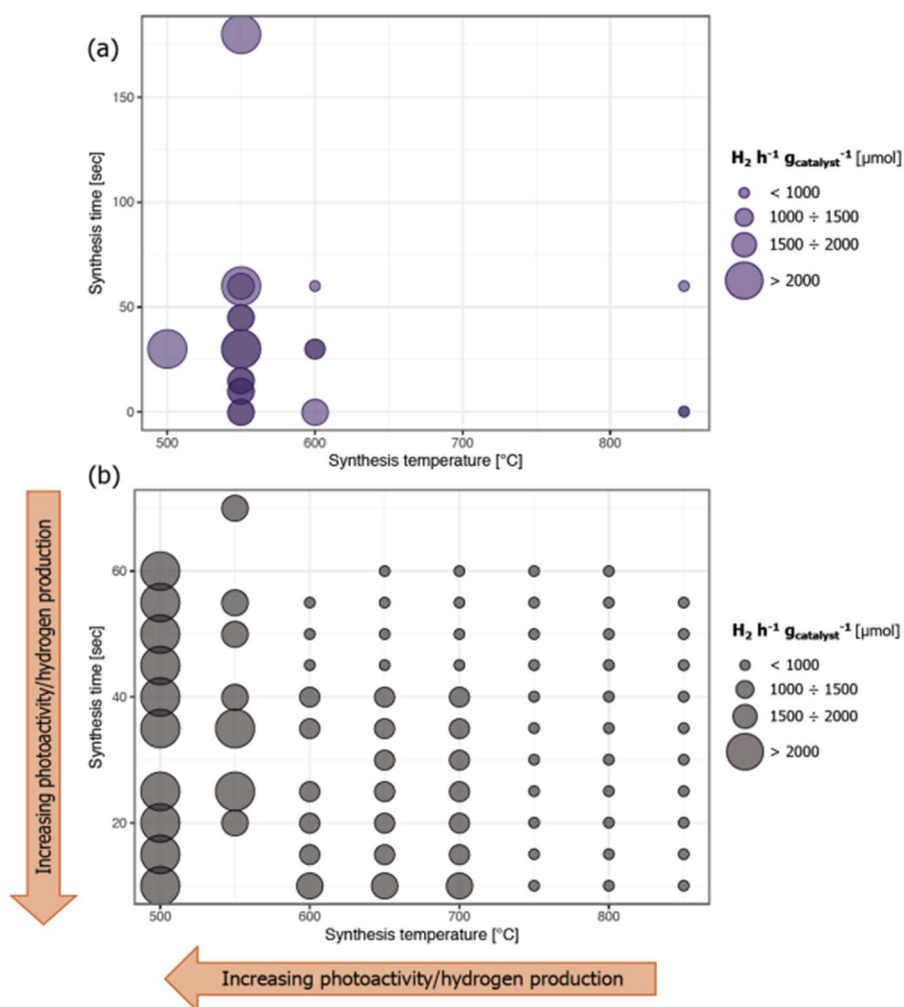
Figure 21 Scatter plot illustrating the relationship between synthesis temperature and synthesis time and their effect on the efficiency of hydrogen production: (a) experimentally measured samples; (b) combinatorically generated theoretical samples. [162]

The relation between model derived hydrogen production values and the experimental results used for validation, also confirms the accuracy of the model (Figure 22.)
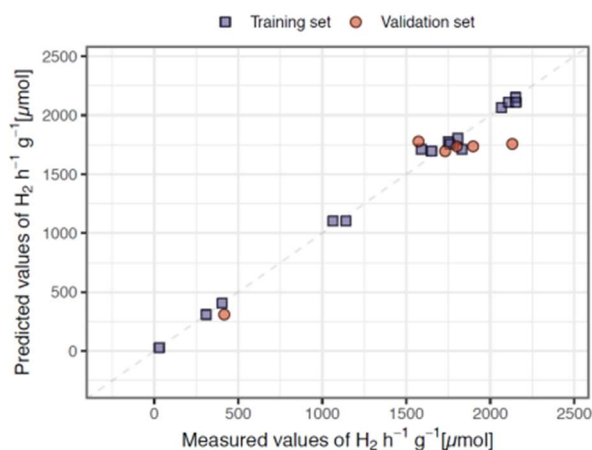
Figure 22. Plot of experimentally measured versus predicted values of hydrogen production $(H_2 \ h^{-1} \ g_{cat}^{-1} \ [\mu mol])$. [162]

The subsequent step involved the utilization of the developed model to determine the optimal synthesis conditions for obtaining the most efficient sample for hydrogen generation. To achieve this, a multitude of samples with different time and temperature variables were combinatorially generated and then modelled. The range of the search was confined to 500-850°C and 0-60s to ensure that the model does not make predictions beyond the experimentally derived data. The outcomes revealed that the sample synthesized at 500°C with a graphene generation time of 15-45 seconds is expected to produce 2151.66 µmol $H_2 \ h^{-1}_{gcat}^{-1}$. As a next step, a physical sample was synthesized at 500°C with 25 seconds of graphene generation time. The resulting sample exhibited a hydrogen generation performance of 2296.27 µmol $H_2 \ h^{-1}_{gcat}^{-1}$, proving to be the most efficient sample in this study and validating the model's reliability.

9.1.4. Proposed photocatalysis mechanism in TiO₂-Cu-C composites

The presence of a graphene layer has a minor impact on the photocatalytic activity of TiO₂-Cu-C composites, with the presence of copper and other factors having a much greater influence. The negative correlation between photoactivity and synthesis temperature is likely due to two factors. Firstly, higher temperatures lead to the formation of larger grains of TiO₂, reducing the surface area/mass of the catalyst. Secondly, temperatures above 600°C cause anatase to rutile conversion, resulting in structural changes in Titania crystals that can be detrimental to photoactivity.

The generation of the graphene layer occurs immediately after the reduction of copper to its metallic form, and it is assumed that metallic copper remains reduced until the graphene cover is breached. However, it is possible that the cover may be imperfect, leading to oxidation of some copper nanoparticles. Previous studies have shown that unprotected metallic copper can oxidize almost immediately after exposure to air. The presence of a graphene layer may act as a shielding agent to prevent oxidation, but it is not always 100% effective, and there is a possibility of copper oxide quantum dots being created from metallic copper nanoparticles below 3 nm in diameter.

There are three potential mechanisms of photoinduced water splitting: TiO_2 with metallic copper as co-catalyst, TiO_2 with CuxOy as composite semiconductors, and both materials mixed with a graphene cover. In all cases, the graphene cover serves as an additional, Schottky-like cocatalyst, preventing charge recombination and acting as a conduit for electrons.

The weak positive correlation between graphene synthesis time and photoactivity may be due to the fact that prolonged synthesis does not necessarily lead to a larger surface area. It is possible that graphene is only generated up to a certain point until the entire copper surface is covered, insulating it from the surrounding environment. This could explain why TEM images of samples with varying graphene generation times do not show significant differences in morphology.

9.1.5. Efficiency and viability – hydrogen evolution

When discussing the efficacy of current photocatalysts, a major issue is the lack of a common methodology for reliable comparison between publications and calculation of the actual viability of a given photocatalyst. However, recent publications recognize this problem and are shifting towards unification of methodology and standardization of result reporting. Some authors propose a benchmark of 10% STH efficiency that must be achieved to recognize a photocatalyst as industrially viable, but this number is somewhat arbitrary and may omit the economical aspect. Economic efficiency may overrule the 10% STH rule and make photocatalysts viable even with lower efficiency.

To assess the economic viability of current photocatalysts, a thought experiment was conducted. Assuming an average household requires 8 kWh per day and that 1 kWh is

equivalent to ~14.2 mol H_2, with the energy of hydrogen released with the use of a 50% efficient power cell, 1 kWh of energy requires 28.5 mols of H_2. Since the efficiency of photocatalysts is reported in mol $_{h-1\ gcat}^{-1}$ and there are on average four hours of useful sunlight available in central Europe, a hypothetical photocatalyst needs to evolve an equivalent of 2 kWh per one hour, which, considering the fuel cell efficiency, gives us ~60 mols of H_2 per hour requirement. Assuming the efficiency reported in mmol H_2 h^{-1} $_{gcat}^{-1}$, the amount of photocatalyst required for powering the average household can be calculated using the formula M photocatalyst = (P equivalent / Eff)/1000, where M photocatalyst is the required mass of the photocatalyst in kg, P equivalent is the power equivalent expressed in mols of H_2 required to release 2 kWh of energy, and Eff is the photocatalyst efficiency expressed in mmol H_2 h^{-1} $_{gcat}^{-1}$.

For the purpose of this work, a model photocatalyst (TiO_2-Cu-C-500-25) was synthesized with an efficiency of 2.3 mmol H_2 h^{-1} g^{-1} and an estimated material cost of producing one ton of the photocatalyst of approximately 2823 USD (with current market prices taken from worldbank.org). In the model application, 26 kg costing 73.5 USD of this photocatalyst would suffice to power one household, but to match current electricity prices, it would have to maintain stability over the period of 214 hours. The efficiency of the TiO_2-Cu-C-500-25 catalyst equals 2.06%, which is almost twice as high as the maximal theoretical efficiency of pure TiO_2 equal to 1.33%, indicating that it is possible to significantly increase the basic capabilities of single material semiconductor photocatalysts. However, with this efficiency, the photoreactor's surface required to power a single household would be equal to 100 m^2. The amounts of photocatalysts needed for any practical attempt of employment are well within tens of kilograms, which strongly indicates that only scalable methods of synthesis (like the use of a fluidized bed reactor) are viable if any practical scale attempts are to be made. Also, at this magnitude of production, the costs cannot be neglected, and thus photocatalysts containing only earth-abundant and readily accessible materials are preferable.

The above estimates are a thought experiment and do not include the costs of an actual photoreactor and the equipment necessary to operate it. Nevertheless, they are not outside the realm of possibility and confirm that it is entirely possible to proceed with the attempts of employing photocatalysts in real-life practice.

9.2. Ag$_3$PO$_4$ modified with graphene via plasma sputtering

In a previous study conducted by Zwara et al. [173], Ag$_3$PO$_4$ was found to exhibit high photocatalytic activity, particularly in the rhombic dodecahedral morphology, which outperformed other tested morphologies. This morphology was chosen for further experimentation in this work, specifically for surface modification with graphene via plasma sputtering. To investigate the effect of varying sputtering times on the composite photocatalysts, several samples were synthesized, and each was labeled according to the sputtering time as the only variable synthesis parameter. The label contains all relevant information concerning sample preparation and is encoded as follows: <semiconductor name (Ag$_3$PO$_4$)>_<graphene presence indicator marked as "GR" (present if the graphene sputtering has been performed)> <(graphene sputtering time) in seconds>. Thus, a sample labeled as Ag$_3$PO$_4$_GR (60s) represents Ag$_3$PO$_4$ treated with plasma graphene sputtering for 60 seconds. All synthesized photocatalysts and their respective labels have been listed in Table 10.

Table 10. List of photocatalysts synthesized for the purposes of current experiment.

| Sample label	Sputter time (s)
Ag$_3$PO$_4$	0
Ag$_3$PO$_4$_GR(15s)	15
Ag$_3$PO$_4$_GR(30s)	30
Ag$_3$PO$_4$_GR(60s)	60
Ag$_3$PO$_4$_GR(150s)	150
Ag$_3$PO$_4$_GR(300s)	300

9.2.1 Morphology and composition

The investigation of the newly synthesized Ag$_3$PO$_4$ photocatalysts was carried out using SEM, TEM, EDS, and HAADF analysis techniques. SEM imaging revealed that the Ag$_3$PO$_4$ particles were rhombic dodecahedral in shape, with some irregularly shaped particles in the size range of 0.5–10 nm. These particles had smooth surfaces and were similar to those reported in previous studies [174-179]. Plasma sputtering treatment of the samples resulted in a visible

change in morphology, with the particle size remaining the same but the surface texture becoming rugged. The addition of graphene was observed in the form of semi-transparent flakes on the surface of Ag_3PO_4, as marked in circles in Figure 23.

TEM imaging confirmed the presence of graphene flakes on the surface of Ag_3PO_4, as well as silver nanoparticles, which were 10 nm in diameter, on the surface of Ag_3PO_4 and on the surface of graphene flakes at some distance away from Ag_3PO_4. The silver nanoparticles were most likely a side-product of the sputtering process and originated from Ag^+ present in the semiconductor. The morphology of the graphene flakes was affected by the sputtering time, with shorter sputtering times resulting in more tightly fitted flakes to the surface of Ag_3PO_4, while longer sputtering times produced more discreet and protruding graphene sheets.

EDS and HAADF analysis provided a better understanding of the elemental composition of the synthesized samples. The dominant building blocks of the samples were found to be silver, oxygen, phosphorus, and carbon, which aligns with what was expected. The obtained results demonstrate that plasma sputtering treatment can significantly change the morphology of Ag_3PO_4, and the addition of graphene can enhance its photocatalytic activity. The presented results may have important implications for the design and development of advanced photocatalytic materials for various applications.
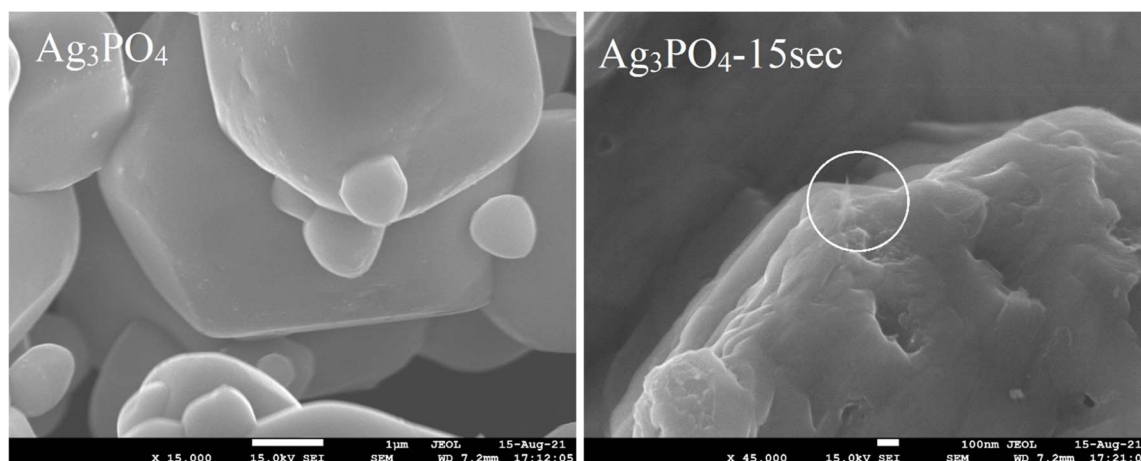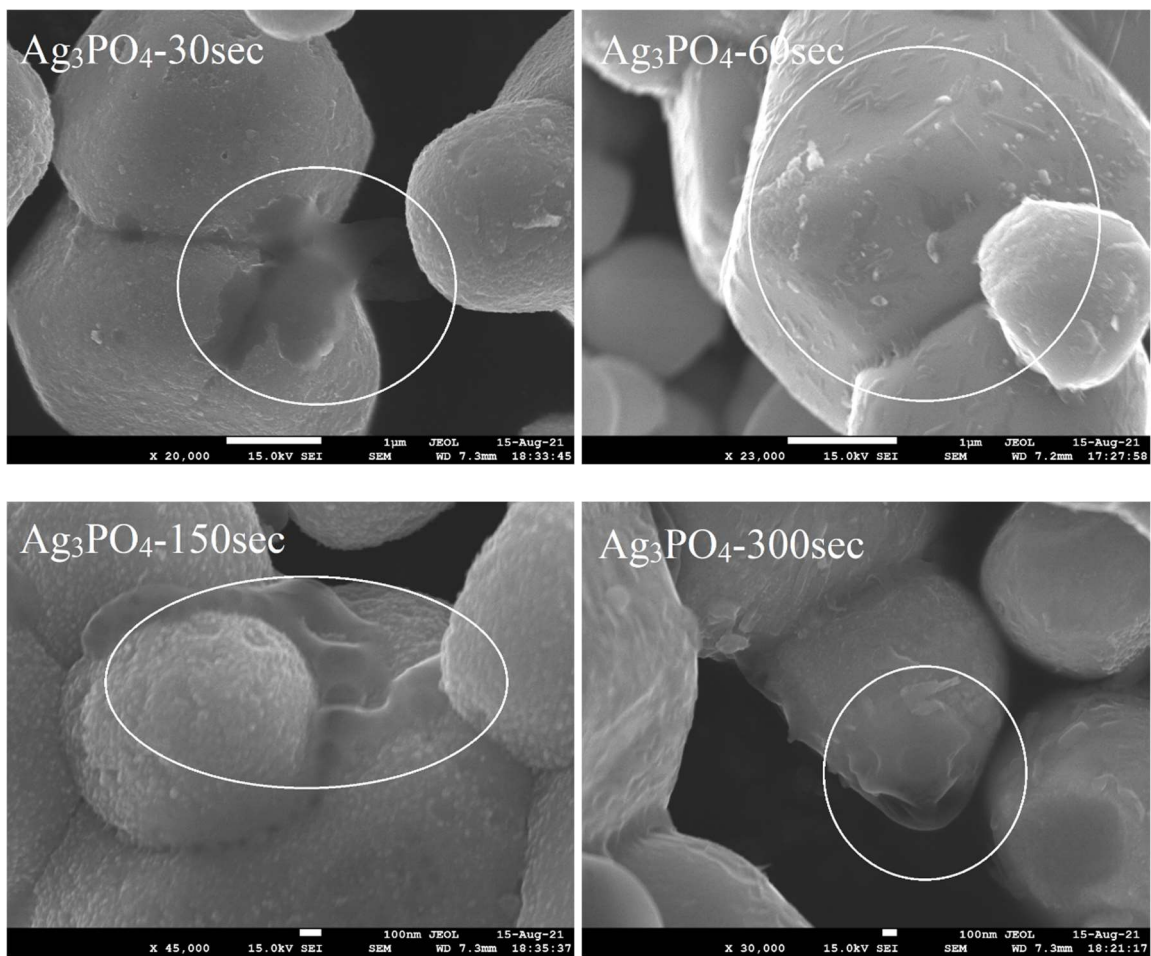
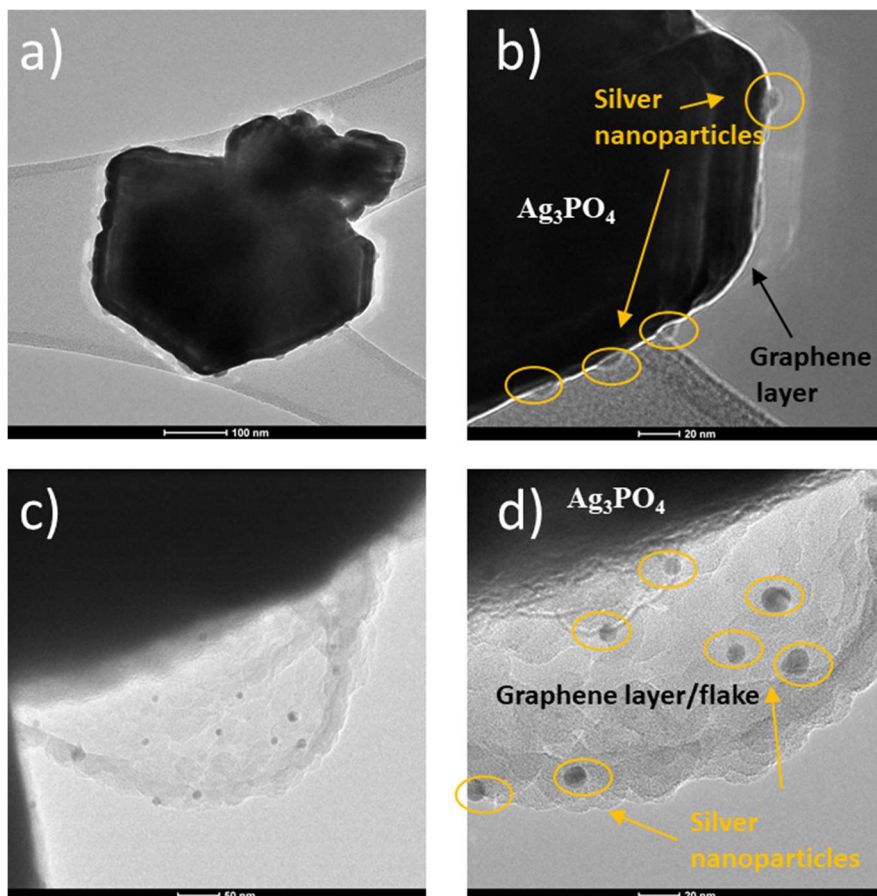**Figure 23.** SEM images of obtained photocatalytic composites, graphene flakes have been marked in white circles [177]

Figure 24. TEM images of Ag$_3$PO$_4$_GR(15s) after photocatalytic process (marked a) and b)) and Ag$_3$PO$_4$_GR(150s) marked c) and d). Metallic silver nanoparticles have been marked in yellow circles. [177]
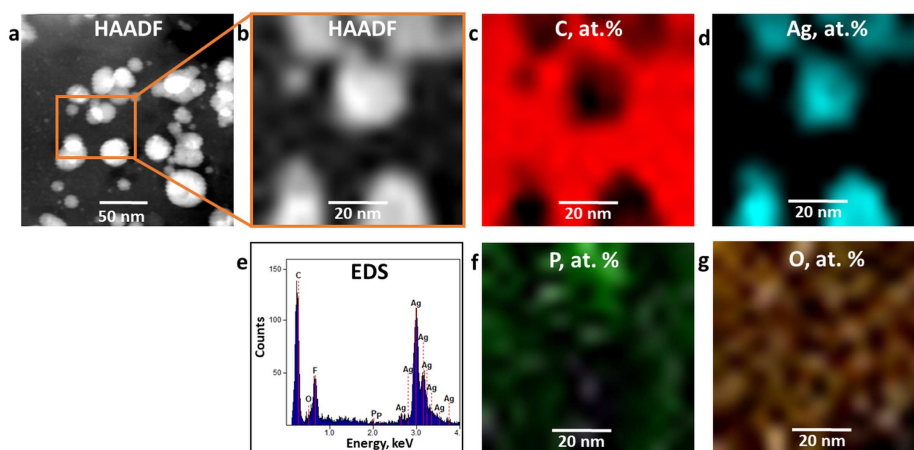

Figure 25. Silver nanoparticles in graphene matrix. (a, b) Scanning Transmission Electron Microscopy (STEM) High Angle Annular Dark Field (HAADF) imaging (c, d, f, g) – element maps and (e) Energy Dispersive X-ray (EDS) spectrum. Sample – Ag$_3$PO$_4$_GR(150s) [177]

Figure 26 presents the Raman spectra of the analyzed photocatalysts. The obtained results confirm the expected composition of the photocatalyst. All samples exhibited visible peaks at 406 and 555 cm^{-1}, corresponding to the symmetric and asymmetric bending of [PO$_4$], respectively. The symmetric and asymmetric peaks of O-P-O bonds were also visible at 909 and 1003 cm^{-1} [180-191]. The G-band related peak remained relatively constant in magnitude across all samples, except for the one treated for 300 seconds, where the overall shape of the spectra suggested that it was obscured by the background noise and broadened beyond recognition due to the buildup of non-graphitic amorphous carbon. The lack of a D-band may be attributed to the absence of edge defects in graphene planes or its small size that could not be detected against the background noise.
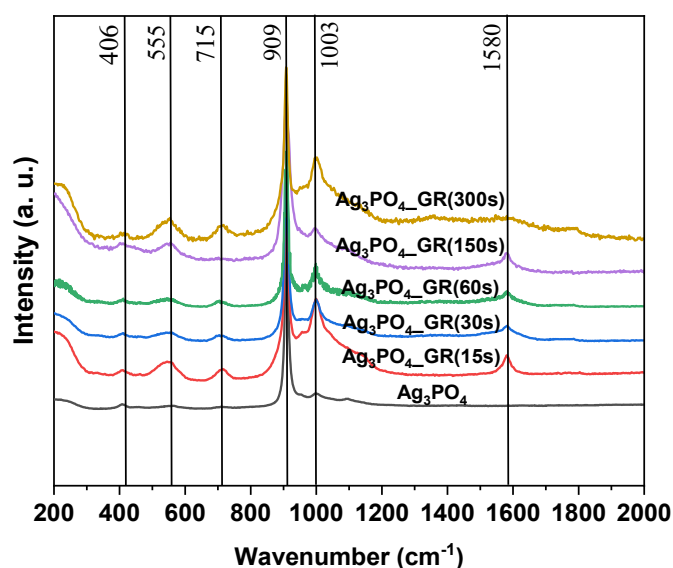

Figure 26. Raman spectra of the investigated samples. [177]

The X-ray diffraction patterns of the investigated samples have been analyzed, and the results are presented in Figure 7. The diffraction patterns confirm that the initial material is Ag_3PO_4, as evidenced by the presence of peaks at 20.9°, 29.7°, 33.2°, 36.6°, 47.8°, 52.7°, 55.0°, 57.3°, 61.6°, 69.8°, and 71.9°. These peaks can be indexed by the crystallographic (110), (200), (210), (211), (310), (222), (320), (321), (400), (420), and (421) planes, assuming a cubic (P-43n) crystal structure type. The refined lattice parameter a is very close to the reported value for Ag_3PO_4, which is a = 6.01839(7) [38], with a value of a = 6.0127(2) Å.

Neither the base material nor the samples exposed to plasma sputtering showed any traces of metallic silver. However, in the post-processed samples, reflections at 38.1, 44.3, and 64.4, respectively corresponding to (111), (200), and (220) planes, appeared. This effect is likely due to the fact that silver in Ag_3PO_4 is very susceptible to thermal and photoinduced reduction to metallic form. The nanographene deposition method used in this work was specifically selected for this material as it allows for graphene nanostructures deposition without significantly heating up the sample. The ambient plasma, which carries little heat due to very low density (similar to the ionosphere layer of the atmosphere), was used. The obtained diffraction patterns did not reveal any traces of graphene in Ag_3PO_4-GR, possibly due to very low concentration.
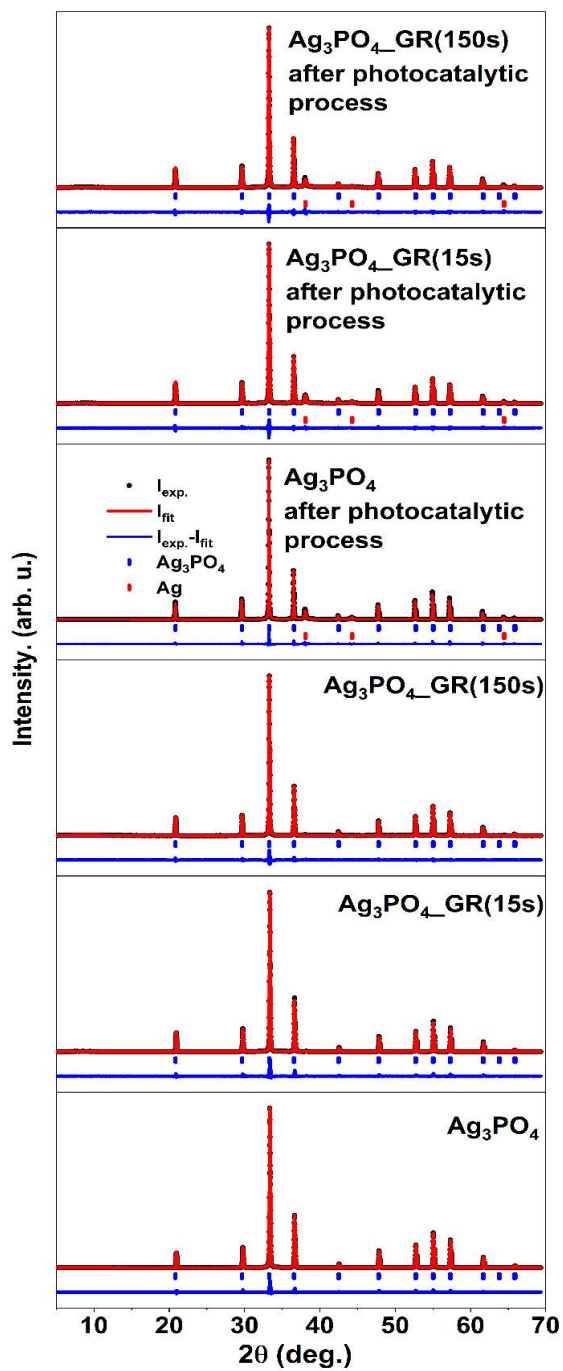
Figure 27. X-ray diffraction patterns for: Ag₃PO₄, Ag₃PO₄_GR(15s), Ag₃PO₄_GR(150s), before and after the photocatalytic process of phenol degradation. [177]
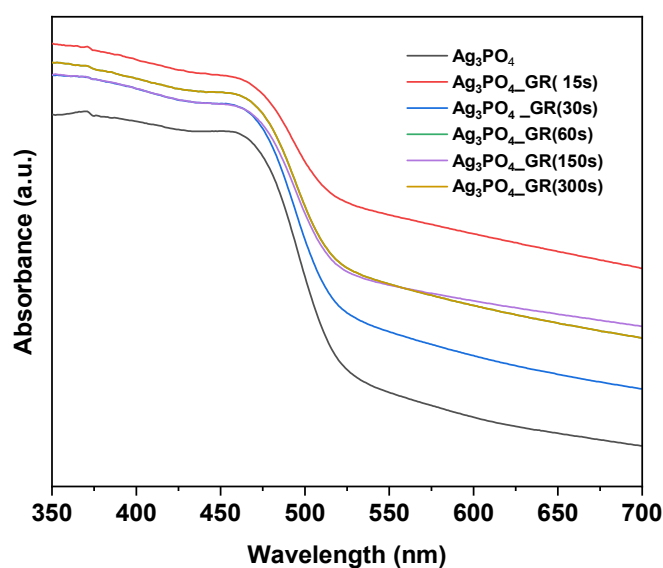
Figure 28. UV-VS Spectra of the investigated samples [177]

Figure 28 demonstrates the UV-vis diffuse reflectance spectra of all samples. Pure Ag_3PO_4 exhibits prominent absorption properties in both the UV and visible regions, up to 550 nm. However, Ag_3PO_4 subjected to plasma nanographene sputtering process has shown a significant increase in absorbance in the visible light region (>560 nm). These results indicate that both pure Ag_3PO_4 and Ag_3PO_4-GR samples are suitable for use as visible light induced photocatalysts. The absorption spectra of Ag_3PO_4 subjected to plasma nanographene sputtering are similar to those reported by other researchers for Ag_3PO_4-graphene and Ag_3PO_4-graphene oxide composites [193-195]

9.2.2. Photoactivity and stability (water purification experiment)

The photocatalytic efficiency of the composite photocatalysts was evaluated for water purification using phenol as a model pollutant and VIS light only irradiation (with a 455 nm cut-off filter). The experimental results are presented in Figure 29. Pristine Ag_3PO_4 exhibited the highest efficiency, degrading 100% of phenol within 5 minutes. Ag_3PO_4_GR (15s), which was sputtered for the shortest amount of time, was the second best performer and achieved complete degradation of phenol within 10 minutes. Samples subjected to plasma sputtering for exposure times between 30 and 150 seconds performed similarly to each other, except for the

Ag$_3$PO$_4$_GR (300s) sample, which was unable to degrade the phenol within 20 minutes. The prolonged sputtering process may have led to the obstruction of the surface of Ag$_3$PO$_4$ by soot and/or metallic silver nanoparticles. The rise in the concentration of benzoquinone, a phenol degradation product, was proportional to the phenol decomposition and was evident for the samples Ag$_3$PO$_4$, Ag$_3$PO$_4$_GR (15s), Ag$_3$PO$_4$_GR (30s), Ag$_3$PO$_4$_GR (60s), and Ag$_3$PO$_4$_GR (150s), indicating that the disappearance of phenol was not due to an adsorption process.

Although the addition of graphene did not enhance the activity of the samples, it significantly improved their stability, as shown in Figure 30. Pristine Ag$_3$PO$_4$ was found to be highly susceptible to photocorrosion, with the efficiency dropping to only 5% of its original potential after just four cycles of water purification. In contrast, the samples subjected to graphene deposition through plasma sputtering were found to be much more stable, with Ag$_3$PO$_4$_GR (15s) retaining approximately 70% of its initial efficiency after four cycles of the experiment, while Ag$_3$PO$_4$_GR (150s) retained around 30%.

The photocorrosion mechanism of Ag$_3$PO$_4$ involves the reduction of silver to its metallic form by electron-hole pairs created by the semiconductor, which leads to the degradation of the semiconductor structure and the blocking of light reaching the semiconductor's surface, as non-transparent silver particles obstruct the flow of photons. Graphene can act as an electron conduit and prevent the electrons from reducing the silver atoms, thus avoiding the degradation of the semiconductor structure. This mechanism has been described by other authors (references [198-206]). However, XRD (Figure 27) and TEM (Figure 24 and 25) analysis indicated that graphene coating did not fully prevent the photocorrosion of the material, as silver nanoparticles were found in all samples that underwent the photocatalytical experiment. Furthermore, some of the silver particles were not situated directly on the surface of the semiconductor but rather were found on the graphene flakes and separated from Ag$_3$PO$_4$. This indicates that silver nanoparticles are capable of migrating from the surface of the semiconductor onto the surface of graphene, as observed by other researchers (reference [207]).
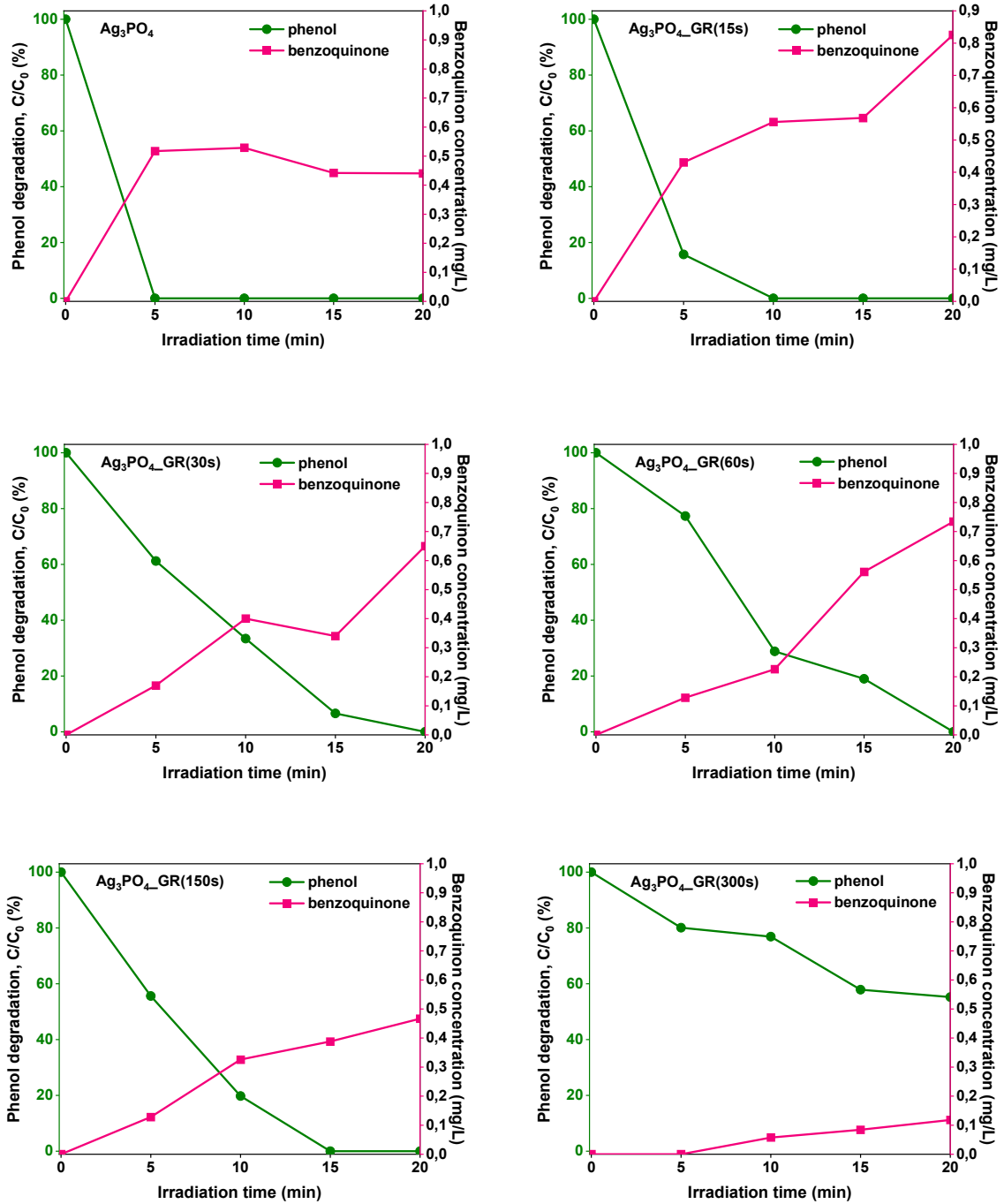
Figure 29. Kinetics of phenol degradation and benzoquinone evolution. Phenol (green line) is given as a percentage of the initial concentration. Benzoquinone concentration (a red line) is given in mg dm^{-3}. [177]
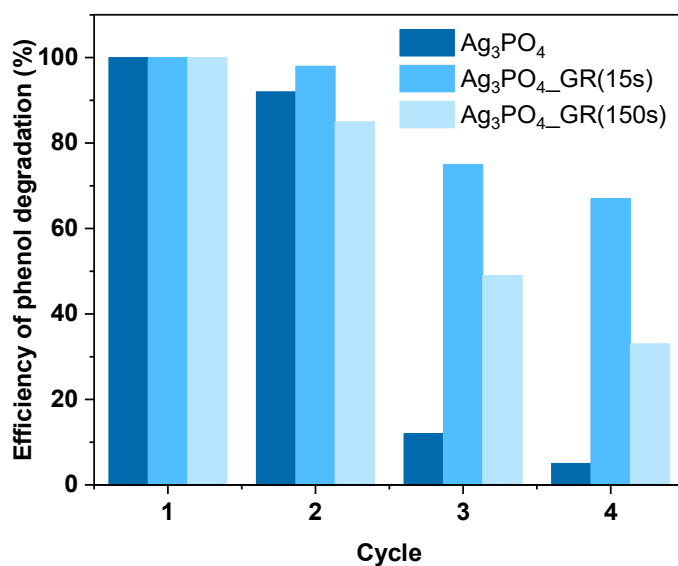
Figure 30. Results of the stability test. Photocatalysts have been separated from the solution, rinsed with deionized water and dried between the cycles. [177]

9.2.3. Action spectra analysis

To investigate whether plasma sputtering of graphene has an impact on the correlation between photoactivity and irradiation wavelength, the study examined pristine Ag_3PO_4 and the most stable sample - Ag_3PO_4_GR (15s) for action spectra analysis. The apparent quantum efficiency (AQE) was calculated as a function of irradiation light (455, 460, 470, 480, 505, 510 nm) using the equation:

AQE(%) = [(2 × number of evolved hydroquinone molecules) / (number of incident photons)] × 100%

As shown in Figure 10, the results revealed that the AQE decreases as the incident wavelength increases for both pristine Ag_3PO_4 and Ag_3PO_4_GR(15s) photocatalysts. The sample exposed to plasma sputtering showed lower activity than pristine Ag_3PO_4 in the shorter wavelength range (455, 460 nm) but became more active than pristine Ag_3PO_4 in the longer wave range (505, 510 nm). The AQE of the samples demonstrated good overlap between the apparent quantum efficiencies and absorbance spectrum at different irradiation wavelengths. Therefore,

photocatalytic degradation of phenol was mainly dependent on the photoabsorption properties of the photocatalyst used.
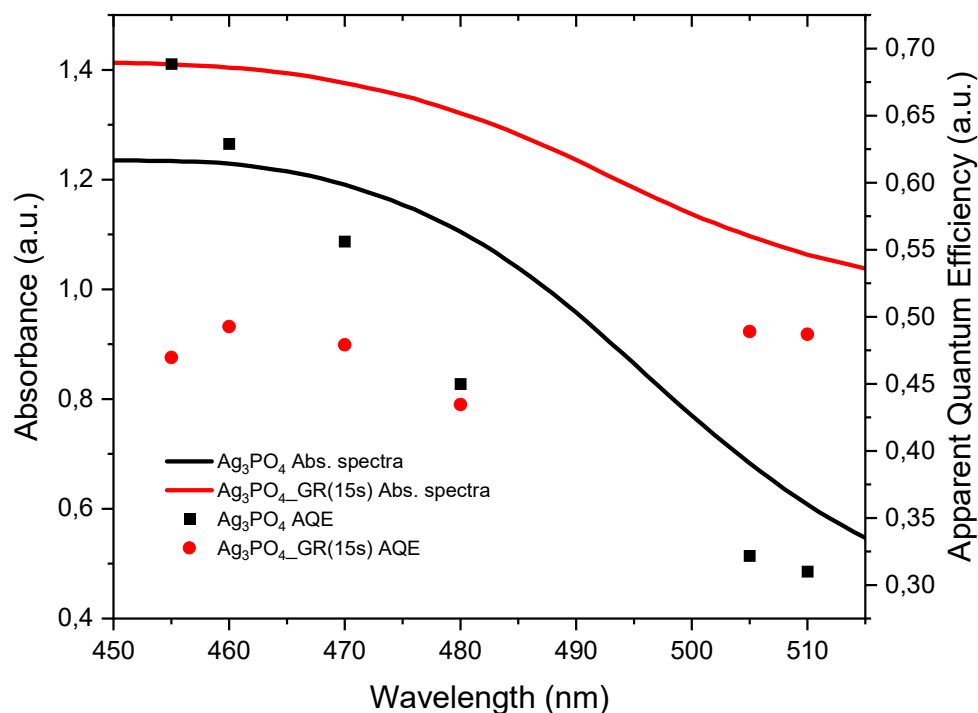

Figure 31. Action spectra of pristine Ag_3PO_4 and $Ag_3PO_4\_GR(15s)$ Absorption spectra of Ag_3PO_4 and $Ag_3PO_4\_GR(15s)$ has been presented as black and red lines respectively. Apparent Quantum Efficiency (AQE) has been presented as black squares for Ag_3PO_4 and red dots for $Ag_3PO_4\_GR(15s)$ [177]

9.2.4. Role of active species

To determine if the addition of graphene alters the photoactivity mechanism of silver phosphate, an experiment was conducted to determine the role of active species in the photocatalytic process. This experiment was compared with previous work done by Zwara et al. where rhombic dodecahedral Ag_3PO_4 was synthesized and investigated for the role of active species using the same procedure and equipment. The scavenger experiment results are presented in Figure 32, where the most active sample ($Ag_3PO_4\_GR(15s)$) was chosen for the experiment. The graph displays the photodegradation of phenol and the effect of scavengers on the reaction rate. It was observed that p-Benzoquinone (BQ) had the greatest impact on slowing the reaction, while tert-butyl alcohol (TBA) and silver nitrate ($AgNO_3$) had a lesser impact. These findings

suggest that, similar to Zwara's work, superoxides ($O_2^{-\bullet}$) play the most significant role in the phenol degradation process, while $^{\bullet}OH$ radicals and excited electrons do not have as significant a role in the reactions. These results are almost identical to those reported by Zwara, indicating that the addition of graphene does not alter the chemical pathways of the photocatalytic mechanism in this instance. This also explains why there was no increase in photoactivity in the graphene-modified samples.
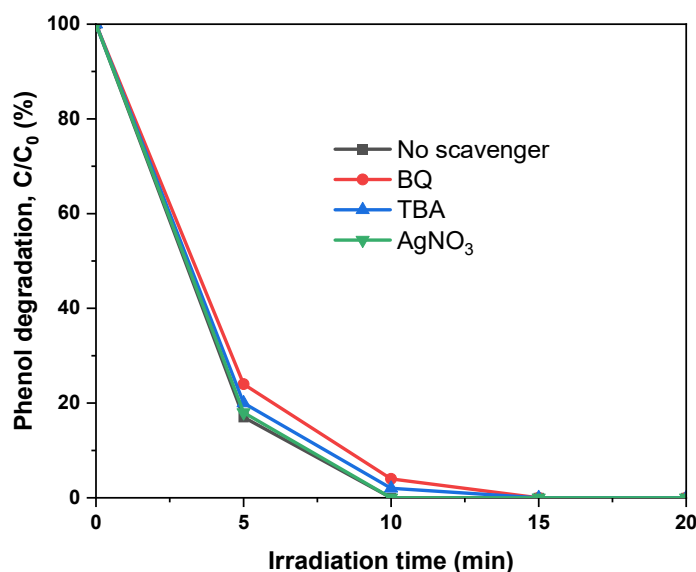

Figure 32. Active species participation in the mechanism of phenol degradation for Ag_3PO_4_GR(15s) [177]

9.2.5. Proposed photocatalytic mechanism in Ag₃PO₄-GR Composites

The deposition of graphene onto Ag_3PO_4 through plasma sputtering method has resulted in an increase in stability. However, contrary to expectations, graphene did not enhance the photocatalytic activity, and prolonged sputtering of graphene had an adverse effect on both stability and activity. TEM analysis confirmed that graphene did not prevent photocorrosion of Ag_3PO_4, as metallic silver nanoparticles were observed, and their numbers increased during the photoactivity experiments. The stability enhancement of Ag_3PO_4 by graphene modification is attributed to two mechanisms: (i) the graphene coating allows electrons to move away from the semiconductor, preventing the silver reduction, and consequently reducing the rate of metallic silver particle generation, and (ii) the silver nanoparticles migrate from the semiconductor

surface to the graphene sheets, thus avoiding obstruction of the Ag_3PO_4 surface from light. The migration of silver nanoparticles has been reported in previous experiments, but not in the context of enhancing photocatalyst stability [207]. The scavenger experiment revealed that the presence of graphene did not alter the activity mechanism, which follows the same chemical paths as described by Zwara et al. in previous work [173], attributing the primary role to superoxide radicals.

9.2.6. Efficiency and viability – water purification

The efficiency and viability of photocatalysts for water purification make them ideal for industrial applications, with many achieving near 100% efficiency within minutes of use. However, to make the transition from laboratory to practical use, certain factors must be considered. A review of table 1 shows that many photocatalysts designed for water purification contain metals such as Ni, Zn, Mn, Sn, Cd, and other elements that may pose a potential risk to the environment and human health. The production process is another factor that needs to be taken into account, as only a few studies mention the possibility of scalable production. Stability is also a crucial factor for photocatalysts intended for environmental purification (water and air), as it minimizes the risk of environmental spillage. As environmental waters often contain a mix of unpredictable natural substances and/or contaminants such as pharmaceuticals, polycyclic aromatic hydrocarbons, and other persistent organic pollutants, it is essential to include natural water purification in mainstream research to gather the knowledge required for the safe implementation of photocatalytic water purification. In this study, the plasma sputtering method was employed to increase stability, and it was shown that an industrial and scalable method of plasma sputtering could successfully be used to deposit graphene on the surface of a typically unstable semiconductor and increase its stability to a point of reasonable utility.

10 Conclusions

The aim of this study was to verify seven initial hypotheses regarding the effect of graphene on the photoactivity and stability of semiconductor photocatalysts. The experimental results have provided answers to these hypotheses as follows:

Re 1. Application of graphene on the surface of a semiconductor can increase its photoactivity, possibly through a mechanism similar to that of a metal cocatalyst. However, the effect of graphene on the activity of TiO_2-Copper composites was small, while no effect was observed for Ag_3PO_4. Furthermore, prolonged graphene synthesis had a detrimental effect on the activity of the photocatalysts, suggesting that the influence of graphene on the photocatalytic process is specific to each photocatalyst.

Re 2. The experimental data did not provide a clear answer as to whether graphene increases the photoactivity of a photocatalyst by increasing its specific area. Ag_3PO_4 did not show any changes in its photochemical pathways due to the presence of graphene, and no significant improvement in activity was observed. In the case of TiO_2-Copper composites, high temperatures (T>600ºC) of graphene synthesis led to sintering of the semiconductor, thus defeating the specific surface gain provided by the graphene. However, samples treated at T<550ºC demonstrated a noticeable increase in activity, although the mechanism behind this increase remains unclear. Therefore, the second hypothesis remains plausible but requires further investigation.

Re 3. Application of graphene on the surface of a semiconductor greatly increased the stability of Ag_3PO_4, as evidenced by the prevention (or at least slowing down) of the photocorrosion of Ag_3PO_4. Additionally, an unexpected stability increase mechanism was observed in which metallic silver nanoparticles migrated from the surface of Ag_3PO_4 to the body of the graphene flakes, preventing obstruction of light reaching the semiconductor by excess metallic silver. TiO_2-Copper composites, being a relatively stable semiconductor, showed a less pronounced effect of graphene on stability. However, the presence of metallic copper in TiO_2-Cu-C composites indicates the high possibility of graphene preventing (or slowing down) Cu(0) oxidation, which occurs quickly under normal ambient conditions.

Re 4. The results confirm the applicability of scalable and industrial methods for photocatalyst synthesis. Two methods were used in this study: chemical vapor deposition (CVD) in a

fluidized bed reactor for TiO_2-Cu-Graphene photocatalysts, and plasma sputtering for Ag_3PO_4-Graphene components. The use of these methods in the field of photocatalyst synthesis has not been attempted before, and both methods proved to be fully viable, scalable, and industrial.

Re 5. The fluidized bed reactor allowed for the synthesis of graphene at temperatures as low as 500ºC, with the most active samples obtained at precisely this temperature. Therefore, hypothesis number 5 is fully confirmed.

Re 6. Graphene is an unusual material in terms of popular application of plasma sputtering reactors. Initially developed for metal coatings, the literature on the use of these reactors for obtaining graphene layers is scarce. Therefore, it was not immediately clear whether this method would work with a graphite target electrode, especially for photocatalysts. However, the experiments confirmed hypothesis number 6.

Re 7. Graphene was successfully synthesized directly on the surface of the semiconductor in a fluidized bed reactor. Metallic copper was necessary for the synthesis of graphene via the CVD method. However, this hypothesis was confirmed.

As of today, one of the most important challenges of the field of photocatalyst research is the standardization of the photoactivity measurements. The overwhelming majority of the published research does not allow for recalculating efficiency data into absolute values, that would allow for direct comparison of the results. In order to achieve that, the bare minimum of the following information must be included in all published papers: (i) the spectrum of the light used for irradiation, (ii) total power reaching the reactor, (iii) the rate of the reaction in the function of time for the whole experiment, (iv) temperature inside the reactor.

Reporting efficiencies as Quantum Yields or Apparent Quantum Yields would be optimal.

Further research should focus on cataloguing the available efficiency data in order to allow more of the industrial application experiments, similar to those done by Kazuhiko, Wang and Nishiyama [16-18] with the use of the photocatalysts that are both – efficient, scalable in production and environmentally safe.

Photocatalysts are not yet fully ready for industrial and commercial application. But they did reach a point where semi industrial levels of application experiments would provide invaluable data necessary to maintain the current pace of development.

11. Acknowledgements

12. References

[1]   worldbank.org

[2]   Daniel Schmidt, Martin D. Hager, and Ulrich S. Schubert Photo-Rechargeable Electric Energy Storage Systems Adv. Energy Mater. 2016, 6, 1500369 DOI: 10.1002/aenm.201500369

[3]   Timm Weitzel, Christoph H. Glock, Energy Management for Stationary Electric Energy Storage Systems: A Systematic Literature Review, European Journal of Operational Research (2017), Doi: 10.1016/j.ejor.2017.06.052

[4]   S. Jalal Kazempour, M. Parsa Moghaddam, M.R. Haghifam, G.R. Yousefi Electric energy storage systems in a market-based economy: Comparison of emerging and traditional technologies Renewable Energy 34 (2009) 2630–2639 doi:10.1016/j.renene.2009.04.027

[5]   Sergio Vazquez, Member, IEEE, Srdjan M. Lukic, Member, IEEE, Eduardo Galvan, Member, IEEE, Leopoldo G. Franquelo, Fellow, IEEE, and Juan M. Carrasco, Member, IEEE Energy Storage Systems for Transport and Grid Applications IEEE transactions on industrial electronics, vol. 57, no. 12, December 2010 doi: 10.1109/TIE.2010.2076414

[6]   Jamshid Aghaei Mohammad-Iman Alizadeh Demand response in smart electricity grids equipped with renewable energy sources: A review Renewable and Sustainable Energy Reviews Volume 18, February 2013, Pages 64-72 https://doi.org/10.1016/j.rser.2012.09.019

[7]   Simon R. Sinsel Rhea L. Riemke Volker H. Hoffmann Challenges and solution technologies for the integration of variable renewable energy sources—a review https://doi.org/10.1016/j.renene.2019.06.147

[8]   David Kilama Okot Review of small hydropower technology Renewable and Sustainable Energy Reviews Volume 26, October 2013, Pages 515-520 https://doi.org/10.1016/j.rser.2013.05.006

[9]   Jon G. McGowan and Stephen R. Connors Windpower: A Turn of the Century Review Annual Review of Energy and the Environment Vol. 25:147-197 (Volume publication date November 2000) https://doi.org/10.1146/annurev.energy.25.1.147

[10]   Junlei Chen, Jihui Wang and Aiqing Ni Recycling and reuse of composite materials for wind turbine blades: An overview Journal of Reinforced Plastics and Composites 2019, Vol. 38(12) 567–577 DOI: 10.1177/0731684419833470

[11]   Paulsen, E.B.; Enevoldsen, P. A Multidisciplinary Review of Recycling Methods for End-of-Life Wind Turbine Blades. Energies 2021, 14, 4247. https://doi.org10.3390//en14144247

[12]   IRENA (2022), Renewable Energy Statistics 2022, International Renewable Energy Agency (IRENA), Abu Dhabi www.irena.org

[13]   Martin Green, Ewan Dunlop, Jochen Hohl-Ebinger, Masahiro Yoshita, Nikos Kopidakis, Xiaojing Hao Solar cell efficiency tables (version 57) Prog Photovolt Res Appl. 2020;1–13. DOI: 10.1002/pip.3371

[14]   Martin Green, Ewan Dunlop, Jochen Hohl-Ebinger, Masahiro Yoshita, Nikos Kopidakis, Xiaojing Hao Solar cell efficiency tables (version 58) Prog Photovolt Res Appl. 2021;29:657–667. DOI: 10.1002/pip.3444

[15] Fubao Zhang, Xianming Wang, Haonan Liu, Chunli Liu, Yong Wan, Yunze Long, and Zhongyu Cai Recent Advances and Applications of Semiconductor Photocatalytic Technology Appl. Sci. 2019, 9, 2489; doi:10.3390/app9122489

[16] Kazuhiko Maeda and Kazunari Domen Photocatalytic Water Splitting: Recent Progress and Future Challenges J. Phys. Chem. Lett. 2010, 1, 2655–2661 DOI: 10.1021/jz1007966

[17] Qian Wang and Kazunari Domen Particulate Photocatalysts for Light-Driven Water Splitting: Mechanisms, Challenges, and Design Strategies Chem. Rev. 2020, 120, 919−985 DOI: 10.1021/acs.chemrev.9b00201

[18] Hiroshi Nishiyama, Taro Yamada, Mamiko Nakabayashi, Yoshiki Maehara, Masaharu Yamaguchi, Yasuko Kuromiya, Yoshie Nagatsuma, Hiromasa Tokudome, Seiji Akiyama, Tomoaki Watanabe, Ryoichi Narushima, Sayuri Okunaka, Naoya Shibata, Tsuyoshi Takata, Takashi Hisatomi & Kazunari Domen Photocatalytic solar hydrogen production from water on a 100-m^2 scale Nature volume 598, pages 304–307 (2021) https://doi.org/10.1038/s41586-021-03907-3

[19] Hannah Ritchie, Max Roser and Pablo Rosado (2020) - "Energy". Published online at OurWorldInData.org. Retrieved from: 'https://ourworldindata.org

[20] Kaveh Mazloomi Chandima Gomes Hydrogen as an energy carrier: Prospects and challenges Renewable and Sustainable Energy Reviews Volume 16, Issue 5, June 2012, Pages 3024-3033 https://doi.org/10.1016/j.rser.2012.02.028

[21] S. Mekhilefa, R. Saidurb, A. Safari Comparative study of different fuel cell technologies Renewable and Sustainable Energy Reviews Renewable and Sustainable Energy Reviews 16 (2012) 981– 989 doi:10.1016/j.rser.2011.09.020

[22] Markus Graef, Peter Treffinger, Sven-Erik Pohl, Frank Rinderknech Investigation of a highly efficient Free Piston Linear Generator with variable Stroke and variable Compression Ratio a New Approach for Free Piston Engines © 2007 WEVA Journal, pp. 116-120 The World Electric Vehicle Association Journal, Vol. 1, 2007 ISSN 2032-6653

[23] https://www2.pvlighthouse.com.au/resources/optics/spectrum%20library/spectrum%20library.aspx

[24] Ren, G.; Han, H.; Wang, Y.; Liu, S.; Zhao, J.; Meng, X.; Li, Z. Recent Advances of Photocatalytic Application in Water Treatment: A Review. Nanomaterials 2021, 11, 1804. https://doi.org/10.3390/nano11071804

[25] Zongpeng Wang, Zhiping Lin, Shijie Shen, Wenwu Zhong, Shaowen Cao Advances in designing heterojunction photocatalytic materials Chinese Journal of Catalysis Volume 42, Issue 5, May 2021, Pages 710-730 https://doi.org/10.1016/S1872-2067(20)63698-1

[26] Wan Zhao, Zhi Chen, Xiuru Yang, Xiaoxiao Qian, Chunxi Liu, Dantong Zhou, Tao Sun, Ming Zhang, Guoying Wei, Pavani Dulanja Dissanayake, Yong Sik Ok, Recent advances in photocatalytic hydrogen evolution with high-performance catalysts without precious metals, Renewable and Sustainable Energy Reviews, Volume 132, 2020, 110040, ISSN 1364-0321, https://doi.org/10.1016/j.rser.2020.110040.

[27]   Li, X., Yu, J., Wageh, S., Al-Ghamdi, A.A. and Xie, J. (2016), Graphene in Photocatalysis: A Review. Small, 12: 6640-6696. https://doi.org/10.1002/smll.201600382

[28]   Chen, Z., Jaramillo, T., Deutsch, T., Kleiman-Shwarsctein, A., Forman, A., Gaillard, N., . . . Dinh, H. (2010). Accelerating materials development for photoelectrochemical hydrogen production: Standards for methods, definitions, and reporting protocols. Journal of Materials Research, 25(1), 3-16. doi:10.1557/JMR.2010.0020

[29]   Konda Reddy Kunduru, Michael Nazarkovsky, Shady Farah, Rajendra P. Pawar, Arijit Basu, Abraham J. Domb, Nanotechnology for water purification: applications of nanotechnology methods in wastewater treatment, Editor(s): Alexandru Mihai Grumezescu, Water Purification, Academic Press, 2017, Pages 33-74, ISBN 9780128043004

[30]   Gylen Odling and Neil Robertson Bridging the gap between laboratory and application in photocatalytic water purification Catal. Sci. Technol., 2019, 9, 533-545 DOI: 10.1039/C8CY02438C

[31]   Sarah A. Green, Neil V. Blough Optical absorption and fluorescence properties of chromophoric dissolved organic matter in natural waters Limnol. Oceanogr., 39(S), 1994, 1903-l 9 16

[32]   Charles M. Sharpless and Neil V. Blough The importance of charge-transfer interactions in determining chromophoric dissolved organic matter (CDOM) optical and photochemical properties Environmental science: processes & impacts Issue 4, 2014 DOI https://doi.org/10.1039/C3EM00573A

[33]   Mats A. Granskog, Robie W. Macdonald, C.-J. Mundy, David G. Barber, Distribution, characteristics and potential impacts of chromophoric dissolved organic matter (CDOM) in Hudson Strait and Hudson Bay, Canada, Continental Shelf Research, Volume 27, Issue 15, 2007, Pages 2032-2050, ISSN 0278-4343, https://doi.org/10.1016/j.csr.2007.05.001

[34]   A. Mukherji, B. Seger, G. Q. Lu and L. Z. Wang, Nitrogen Doped $Sr_2Ta_2O_7$ Coupled with Graphene Sheets as Photocatalysts for Increased Photocatalytic Hydrogen Production ACS Nano, 2011, 5, 3483.

[35]   Agegnehu, A.K.; Pan, C.-J.; Rick, J.; Lee, J.-F.; Su, W.-N.; Hwang, B.-J. Enhanced hydrogen generation by cocatalytic Ni and NiO nanoparticles loaded on graphene oxide sheets. J. Mater. Chem. 2012, 22, 13849–13854.

[36]   Alansi AM, Qunaibit MA, Alade IO, Qahtan TF, Saleh TA (2018) Visible-light responsive BiOBr nanoparticles loaded on reduced grapheme oxide for photocatalytic degradation of dye. J Mol Liq 253:297–304. https://doi.org/10.1016/j.molliq.2018.01.034

[37]   B. Li and H. Cao, ZnO@graphene composite with enhanced performance for the removal of dye from water J. Mater. Chem., 2011, 21, 3346.

[38]   Bhunia SK, Jana NR (2014) Reduced graphene oxide-silver nanoparticle composite as visible light photocatalyst for degradation of colorless endocrine disruptors. ACS Appl Mater Interfaces 6:20085–20092. https://doi.org/10.1021/am505677x

[39] Borthakur P, Boruah PK, Darabdhara G, Sengupta P, Das MR, Boronin AI, Kibis LS, Kozlova MN, Fedorov VE (2016) Microwave assisted synthesis of CuS-reduced graphene oxide nanocomposite with efficient photocatalytic activity towards azo dye degradation. J Environ Chem Eng 4:4600–4611. https://doi.org/10.1016/j.jece.2016.10.023

[40] C. Chen, W. Cai, M. Long, B. Zhou, Y. Wu, D. Wu and Y. Feng, Synthesis of visible-light responsive graphene oxide/TiO(2) composites with p/n heterojunction ACS Nano, 2010, 4, 6425.

[41] D. Yoo, T. V. Cuong, V. H. Pham, J. S. Chung, N. T. Khoa, E. J. Kim and S. H. Hahn, Curr. D. Yoo, T. V. Cuong, V. H. Pham, J. S. Chung, N. T. Khoa, E. J. Kim and S. H. Hahn, Enhanced photocatalytic activity of graphene oxide decorated on TiO_2 films under UV and visible irradiation Curr. Appl. Phys., 2011, 11, 805. Appl. Phys., 2011, 11, 805.

[42] E. Gao, W. Wang, M. Shang and J. Xu, Synthesis and enhanced photocatalytic performance of graphene-Bi_2WO_6 composite Phys. Chem. Chem. Phys., 2011, 13, 2887.

[43] F. Zhou, R. Shi and Y. Zhu, Significant enhancement of the visible photocatalytic degradation performances of γ-Bi2MoO6 nanoplate by graphene hybridization J. Mol. Catal. A: Chem., 2011, 340, 77.

[44] Fu L, Xia T, Zheng Y, Yang J, Wang A, Wang Z (2015) Preparation of WO_3 -reduced graphene oxide nanocomposites with enhanced photocatalytic property. Ceram Int 41:5903–5908. https://doi.org/10.1016/j.ceramint.2015.01.022

[45] G. Jiang, Z. Lin, C. Chen, L. Zhu, Q. Chang, N. Wang, W. Wei and H. Tang, Enhanced photocatalytic activity of TiO_2/graphene by tailoring oxidation degrees of graphene oxide for gaseous mercury removal Carbon, 2011, 49, 2693.

[46] Ghosh S, Basu S, Baskey (Sen) M (2017) Decorating mechanism of Mn_3O_4 nanoparticles on reduced graphene oxide surface through reflux condensation method to improve photocatalytic performance. J Mater Sci Mater Electron 28:17860–17870. https://doi.org/10.1007/s10854- 017-7727-3

[47] Gliniak, J.; Lin, J.-H.; Chen, Y.-T.; Li, C.-R.; Jokar, E.; Chang, C.-H.; Peng, C.-S.; Lin, J.-N.; Lien, W.-H.; Tsai, H.-M.; et al. Sulfur-Doped Graphene Oxide Quantum Dots as Photocatalysts for Hydrogen Generation in the Aqueous Phase. ChemSusChem 2017, 10, 3260–3267.

[48] H. Hu, X. Wang, F. Liu, J. Wang and C. Xu, Rapid microwave-assisted synthesis of graphene nanosheets–zinc sulfide nanocomposites: Optical and photocatalytic properties Synth. Met., 2011, 161, 404.

[49] H. Sun, L. Cao and L. Lu, Magnetite/reduced graphene oxide nanocomposites: One step solvothermal synthesis and use as a novel platform for removal of dye pollutants Nano Res., 2011, 4, 550.

[50] H. Zhang, P. Xu, G. Du, Z. Chen, K. Oh, D. Pan and Z. Jiao, Synthesis of Reduced Graphene Oxide-Titanium (rGO-TiO_2) Composite Using a Solvothermal and Hydrothermal Methods and Characterized via XRD and UV-Vis Nano Res., 2011, 4, 274.

[51] H. Zhang, X. Lv, Y. Li, Y. Wang and J. Li, P25-Graphene Composite as a High Performance Photocatalyst ACS Nano, 2010, 4, 380.

[52] Huang, T.; Wu, J.; Zhao, Z.; Zeng, T.; Zhang, J.; Xu, A.; Zhou, X.; Qi, Y.; Ren, J.; Zhou, R.; et al. Synthesis and photocatalytic performance of CuO-CeO$_2$/graphene oxide. Mater. Lett.2016,185, 503–506

[53] J. Du, X. Lai, N. Yang, J. Zhai, D. Kisailus, F. Su, D. Wang and L. Jiang, Hierarchically Ordered Macro−Mesoporous TiO$_2$−Graphene Composite Films: Improved Mass Transfer, Reduced Charge Recombination, and Their Enhanced Photocatalytic Activities ACS Nano, 2011, 5, 590.

[54] J. Guo, S. Zhu, Z. Chen, Y. Li, Z. Yu, Q. Liu, J. Li, C. Feng and D. Zhang, Sonochemical synthesis of TiO$_2$ nanoparticles on graphene for use as photocatalyst Ultrason. Sonochem., 2011, 18, 1082.

[55] J. L. Wu, S. Bai, X. P. Shen and L. Jiang, Preparation and characterization of graphene/CdS nanocomposites Appl. Surf. Sci., 2010, 257, 747.

[56] J. Liu, H. Bai, Y. Wang, Z. Liu, X. Zhang and D. Sun, Nanocomposites: A Simple Route to Reduced Graphene Oxide-Draped Nanocomposites with Markedly Enhanced Visible-Light Photocatalytic Performance Adv. Funct. Mater., 2010, 20, 4175.

[57] J. Liu, L. Liu, H. Bai, Y. Wang and D. Sun, Gram-scale production of graphene oxide–TiO$_2$ nanorod composites: Towards high-activity photocatalytic materials Appl. Catal., B, 2011, 106, 76.

[58] J. Zhang, Z. Xiong and X. S. Zhao, Graphene–metal–oxide composites for the degradation of dyes under visible light irradiation J. Mater. Chem., 2011, 21, 3634.

[59] Kumar S, Ojha AK, Walkenfort B Cadmium oxide nanoparticles grown in situ on reduced graphene oxide for enhanced photocatalytic degradation of methylene blue dye under ultraviolet irradiation. J Photochem Photobiol B 159:111–119. https://doi.org/10.1016/j.jphotobiol.2016. 03.025

[60] L. Zhang, Z. Xiong and X. S. Zhao, Pillaring Chemically Exfoliated Graphene Oxide with Carbon Nanotubes for Photocatalytic Degradation of Dyes under Visible Light Irradiation ACS Nano, 2010, 4, 7030.

[61] Latorre-Sánchez, M.; Esteve-Adell, I.; Primo, A.; García, H. Innovative preparation of MoS$_2$ – graphene heterostructures based on alginate containing (NH$_4$)$_2$MoS$_4$ and their photocatalytic activity for H$_2$ generation. Carbon 2015, 81, 587–596.

[62] Latorre-Sánchez, M.; Primo, A.; García, H. P-Doped Graphene Obtained by Pyrolysis of Modified Alginate as a Photocatalyst for Hydrogen Generation from Water–Methanol Mixtures. Angew. Chem. Int. Ed. 2013, 52, 11813–11816.

[63] Lavorato, C.; Primo, A.; Molinari, R.; Garcia, H. N-Doped Graphene Derived from Biomass as a Visible-Light Photocatalyst for Hydrogen Generation from Water/Methanol Mixtures. Chem. A Eur. J. 2014, 20, 187–194.

[64] Mateo, D.; Esteve-Adell, I.; Albero, J.; Primo, A.; García, H. Oriented 2.0.0 Cu$_2$O nanoplatelets supported on few-layers graphene as efficient visible light photocatalyst for overall water splitting. Appl. Catal. B Environ. 2017, 201, 582–590.

[65] Mateo, D.; Esteve-Adell, I.; Albero, J.; Royo, J.F.S.; Primo, A.; Garcia, H. 111 oriented gold nanoplatelets on multilayer graphene as visible light photocatalyst for overall water splitting. Nat. Commun. 2016, 7, 11819.

[66] Nouri M, Saray AM, Azimi HR, Yousefi R High solar-light photocatalytic activity of using Cu_3Se_2 /rGO nanocomposites synthesized by a green co-precipitation method. Solid State Sci 73:7–12. https://doi.org/10.1016/j.solidstatesciences.2017.09.001

[67] Peng H, Jing N, Miao Y, Yan LS (2017) Facile solvothermal synthesis of reduced graphene oxide-$BiPO_4$ nanocomposite with enhanced photocatalytic activity. Chin J Anal Chem 45(3):357–362. https://doi.org/10.1016/S1872-2040(17)61000-4

[68] Prabhu S, Pudukudy M, Sohila S, Harish S, Navaneethan M, Navaneethan D, Ramesh R, Hayakawa Y (2018) Synthesis, structural and optical properties of ZnO spindle/reduced graphene oxide composites with enhanced photocatalytic activity under visible light irradiation. Opt Mater 79:186–195. https://doi.org/10.1016/j.optmat.2018.02.061

[69] Putri, L.K.; Ng, B.-J.; Ong, W.-J.; Lee, H.W.; Chang, W.S.; Chai, S.-P. Heteroatom Nitrogen- and Boron-Doping as a Facile Strategy to Improve Photocatalytic Activity of Standalone Reduced Graphene Oxide in Hydrogen Evolution. ACS Appl. Mater. Interfaces 2017, 9, 4558–4569.

[70] Rahimi K, Zafarkish H, Yazdani A Reduced graphene oxide can activate the sunlight- induced photocatalytic effect of NiO nanowires. Mater Design 144:214–221. https://doi.org/10.1016/j.matdes.2018.02.030

[71] Rosy A, Kalpana G (2018) Reduced graphene oxide/strontium titanate heterostructured nanocomposite as sunlight driven photocatalyst for degradation of organic dye pollutants. Curr Appl Phys 18:1026–1033. https://doi.org/10.1016/j.cap.2018.05.019

[72] Shamsabadi TM, Goharshadi EK, Shafaee M, Niazi Z (2018) ZnS@reduced graphene oxide nanocomposite as an effective sunlight driven photocatalyst for degradation of reactive black 5: a mechanistic approach. Sep Purif Technol 202:326–334. https://doi.org/10.1016/j.seppur.2018.04.001

[73] Shen H, Zhao X, Duan L, Liu R, Wu H, Hou T, Jiang X, Gao H Influence of interface combination of RGO-photosensitized SnO_2 @RGO core-shell structures on their photocatalytic performance. Appl Surf Sci 391:627–634. https://doi.org/10.1016/j.apsusc.2016.06.031

[74] Stefanska KS, Fluder M, Tylus W, Jesionowski T (2018) Investigation of amino-grafted TiO_2 / reduced graphene oxide hybridsas a novel photocatalyst used for decomposition of selected organic dyes. J Environ Manag 212:395–404. https://doi.org/10.1016/j.jenvman.2018.02.030

[75] T. Kamegawa, D. Yamahana and H. Yamashita, Graphene Coating of TiO_2 Nanoparticles Loaded on Mesoporous Silica for Enhancement of Photocatalytic Activity J. Phys. Chem. C, 2010, 114, 15049.

[76] Zeng, Xf., Wang, Js., Zhao, Yn. et al. Construction of TiO_2-pillared multilayer graphene nanocomposites as efficient photocatalysts for ciprofloxacin degradation. Int J Miner Metall Mater 28, 503–510 (2021). https://doi.org/10.1007/s12613-020-2193-y

[77] T. Xu, L. Zhang, H. Cheng and Y. Zhu Significantly enhanced photocatalytic performance of ZnO via graphene hybridization and the mechanism study Appl. Catal., B, 2011, 101, 382.

[78]   Thangavel S, Venugopal G, Kim SJ (2014) Enhanced photocatalytic efficacy of organic dyes using β-tin tungstate reduced graphene oxide nanocomposites. Mater Chem Phys 145:108–115. https://doi.org/10.1016/j.matchemphys.2014.01.046

[79]   Vinoth R, Babu SG, Ramachandran R, Neppolian B (2017) Bismuth oxyiodide incorporated reduced graphene oxide nanocomposite material as an efficient photocatalyst for visible light assisted degradation of organic pollutants. Appl Surf Sci 418:163–170. https://doi.org/10.1016/j.apsusc.2017.01.278

[80]   Wang A, Li X, Zhao Y, Wu W, Chen J, Meng H (2014) Preparation and characterizations of Cu_2O/reduced graphene oxide nanocomposites with high photo-catalytic performances. Powder Technol 261:42–48. https://doi.org/10.1016/j.powtec.2014.04.004

[81]   Wang W, Liu Y, Zhang H, Qian Y, Guo Z (2017b) Re-investigation on reduced graphene oxide/AG_2CO_3 composite photocatalyst: an insight into the double-edged sword role of RGO. Appl Surf Sci 396:102–109. https://doi.org/10.1016/j.apsusc.2016.11.030

[82]   Wang W, Shen J, Li N, Ye M (2013) Synthesis of novel photocatalytic RGO–$ZnWO_4$ nanocomposites with visible light photoactivity. Mater Lett 106:284–286. https://doi.org/10.1016/j.matlet.2013.05.042

[83]   X. Y. Zhang, H. P. Li, X. L. Cui and Y. H. Lin, Graphene/TiO_2 nanocomposites: synthesis, characterization and application in hydrogen evolution from water photocatalytic splitting J. Mater. Chem., 2010, 20, 2801.

[84]   X. Zhang, X. Quan, S. Chen and H. Yu, Constructing graphene/$InNbO_4$ composite with excellent adsorptivity and charge separation performance for enhanced visible-light-driven photocatalytic ability Appl. Catal., B, 2011, 105, 237.

[85]   Xu J, Ao Y, Chen M (2013) A simple method for the preparation of Bi_2WO_6 -reduced grapheme oxide with enhanced photocatalytic activity under visible light irradiation. Mater Lett 92:126–128. https://doi.org/10.1016/j.matlet.2012.10.038

[86]   Y. Fu and X. Wang, Magnetically Separable $ZnFe_2O_4$–Graphene Catalyst and its High Photocatalytic Performance under Visible Light Irradiation Ind. Eng. Chem. Res., 2011, 50, 7210.

[87]   Y. H. Ng, I. V. Lightcap, K. Goodwin, M. Matsumura and P. V. Kamat, TiO_2 Nanostructures: Recent Physical Chemistry Advances J. Phys. Chem. Lett., 2010, 1, 2222.

[88]   Liang, Y., Wang, H., Sanchez Casalongue, H. et al. TiO_2 nanocrystals grown on graphene as advanced photocatalytic hybrid materials. Nano Res. 3, 701–705 (2010). https://doi.org/10.1007/s12274-010-0033-5

[89]   Y. Zhang and C. Pan, TiO_2/graphene composite from thermal reaction of graphene oxide and its photocatalytic activity in visible light J. Mater. Sci., 2011, 46, 2622.

[90]   Y. Zhang, Z. Tang, X. Fu and Y. Xu, TiO_2−Graphene Nanocomposites for Gas-Phase Photocatalytic Degradation of Volatile Aromatic Pollutant: Is TiO_2−Graphene Truly Different from Other TiO_2−Carbon Composite Materials? ACS Nano, 2010, 4, 7303.

[91] Yao S, Xu L, Gao Q, Wang X, Kong N, Li W, Wang J, Li G, Pu X (2017) Enhanced photocatalytic degradation of Rhodamine B by reduced graphene oxides wrapped-Cu_2SnS_3 flower-like architectures. J Alloys Compd 704:469–477. https://doi.org/10.1016/j.jallcom.2017.02.069

[92] Yeh, T.-F.; Syu, J.-M.; Cheng, C.; Chang, T.-H.; Teng, H. Graphite Oxide as a Photocatalyst for Hydrogen Production from Water. Adv. Funct. Mater. 2010, 20, 2255–2262

[93] Yeh, T.-F.; Teng, C.-Y.; Chen, S.-J.; Teng, H. Nitrogen-Doped Graphene Oxide Quantum Dots as Photocatalysts for Overall Water-Splitting under Visible Light Illumination. Adv. Mater. 2014, 26, 3297–3303.

[94] Yousefi R, Azimi HR, Mahmoudian MR, Basirun WJ (2018a) The effect of defect emissions on enhancement photocatalytic performance of ZnSe QDs and ZnSe/rGO nanocomposites. Appl Surf Sci 435:886–893. https://doi.org/10.1016/j.apsusc.2017.11.183

[95] Z. Xiong, L. Zhang and X. Zhao, Visible-Light-Induced Dye Degradation over Copper-Modified Reduced Graphene Oxide Chem. Eur. J., 2011, 17, 2428.

[96] Z. Xiong, L. Zhang, J. Ma and X. S. Zhao, Nanocomposites: A Simple Route to Reduced Graphene Oxide-Draped Nanocomposites with Markedly Enhanced Visible-Light Photocatalytic Performance Chem. Commun., 2010, 46, 6099.

[97] Zhang L, Li N, Jiu H, Zhang Q (2016) Solvothermal synthesis of reduced graphene oxide-Bi_2S_3 nanorod composites with enhanced photocatalytic activity under visible light irradiation. J Mater Sci Mater Electron 27:2748–2753. https://doi.org/10.1007/s10854-015-4086-9

[98] Zhang L, Wang A, Zhu N, Sun B, Liang Y, Wu W (2018a) Synthesis of butterfly-like $BiVO_4$/RGO nanocomposites and their photocatalytic activities. Chin J Chem Eng 26:667–674. https://doi.org/10.1016/j.cjche.2017.09.007

[99] Zhu L, Ye S, Ali A, Ulla K, Cho KY, Oh WC (2015) Modified hydrothermal synthesis and characterization of reduced graphene oxide-silver selenide nanocomposites with enhanced reactive oxygen species generation. Chin J Catal 36:603–611. https://doi.org/10.1016/S1872-2067(14)60275-8

[100] Zou L, Wangn X, Xu X, Wang H (2016) Reduced grapheme oxide wrapped CdS composites with enhanced photocatalytic performance and high stability. Ceram Int 42:372–378. https://doi.org/10.1016/j.ceramint.2015.08.119

[101] Zou X, Zhou Y, Wang Z, Chen S, Xiang B, Qiang Y, Zhu S (2018) Facile synthesis of α-Fe_2O_3 pyramid on reduced graphene oxide for supercapacitor and photo-degradation. J Alloys Compd 744:412–420. https://doi.org/10.1016/j.jallcom.2018.02.126

[102] Y. Wang, J. Yu, W. Xiao, Q. Li, Microwave-assisted hydrothermal synthesis of graphene based Au–TiO_2 photocatalysts for efficient visible-light hydrogen production, J. Mater. Chem. A. 2 (2014) 3847-3855. https://doi.org/10.1039/C3TA14908K.

[103] P. Jiménez-Calvo, V. Caps, M.N. Ghazzal, C. Colbeau-Justin, V. Keller, Au/TiO_2(P25)-gC_3N_4 composites with low gC_3N_4 content enhance TiO_2 sensitization for remarkable H_2 production from water under visible-light irradiation, Nano Energy. 75 (2020) 104888. https://doi.org/10.1016/j.nanoen.2020.104888.

[104] C. Marchal, T. Cottineau, M.G. Méndez-Medrano, C. Colbeau- Justin, et al., Au/TiO$_2$–gC$_3$N$_4$ Nanocomposites for Enhanced Photocatalytic H$_2$ Production from Water under Visible Light Irradiation with Very Low Quantities of Sacrificial Agents, Adv. Energy Mater. 8 (2016) 1702142. https://doi.org/10.1002/aenm.201702142.

[105] S.J.P. Varapragasam, S. Mia, C. Wieting, C. Balasanthiran, et al., Ag–TiO$_2$ Hybrid Nanocrystal Photocatalyst: Hydrogen Evolution under UV Irradiation but Not under Visible-Light Irradiation, ACS Appl. Energy Mater. 2 (2019) 8274–8282. https://doi.org/10.1021/acsaem.9b01730.

[106] M. Manikandan, T. Tanabe, P. Li, S. Ueda, et al., Photocatalytic Water Splitting under Visible Light by Mixed-Valence Sn$_3$O$_4$, ACS Appl. Mater. Interfaces. 6 (2014) 3790–3793. https://doi.org/10.1021/am500157u.

[107] S.W. Cao, J. Fang, M.M. Shahjamali, F.Y.C. Boey, et al., Plasmon-Enhanced Hydrogen Evolution on Au-InVO$_4$ Hybrid Microspheres, RSC Adv. 2 (2012) 5513-5515. https://doi.org/10.1039/C2RA20405C.

[108] J. Zhang, Z. Yu, Z. Gao, H. Ge, et al., Porous TiO$_2$ Nanotubes with Spatially Separated Platinum and CoO$_x$ Cocatalysts Produced by Atomic Layer Deposition for Photocatalytic Hydrogen Production, Angew. Chem. Int. Ed. 56 (2017) 816. https://doi.org/10.1002/anie.201611137.

[109] N. Güy, Directional transfer of photocarriers on CdS/g-C$_3$N$_4$ heterojunction modified with Pd as a cocatalyst for synergistically enhanced photocatalytic hydrogen production, Appl. Surf. Sci. 522 (2020) 146442. https://doi.org/10.1016/j.apsusc.2020.146442.

[110] M. Song, Y. Wu, G. Zheng, C. Du, Y. Su, Junction of porous g- C$_3$N$_4$ with BiVO$_4$ using Au as electron shuttle for cocatalyst-free robust photocatalytic hydrogen evolution, Appl. Surf. Sci. 498 (2019) 143808. https://doi.org/10.1016/j.apsusc.2019.143808.

[111] Z.U. Rahman, N. Wei, M. Feng, D. Wang, TiO2 hollow spheres with separated Au and RuO$_2$ co-catalysts for efficient photocatalytic water splitting, Int. J. Hydrog. Energy. 44 (2019) 13221-13231. https://doi.org/10.1016/j.ijhydene.2019.03.176.

[112] P. Dong, Y. Wang, A. Zhang, T. Cheng, et al., Platinum Single Atoms Anchored on a Covalent Organic Framework: Boosting Active Sites for Photocatalytic Hydrogen Evolution, ACS Catal. 11 (2021) 13266–13279. https://doi.org/10.1021/acscatal.1c03441.

[113] M. Tabata, K. Maeda, T. Ishihara, T. Minegishi, et al., Photocatalytic Hydrogen Evolution from Water Using Copper Gallium Sulfide under Visible-Light Irradiation, J. Phys. Chem. C. 114 (2010) 11215–11220. https://doi.org/10.1021/jp103158f.

[114] Z. Mo, H. Xu, X. She, Y. Song, et al., Constructing Pd/2D- C$_3$N$_4$ composites for efficient photocatalytic H$_2$ evolution through nonplasmon-induced bound electrons, Appl. Surf. Sci. 467-468 (2019) 151-157. https://doi.org/10.1016/j.apsusc.2018.10.115.

[115] Y. Chen, Y. Liu, Z. Ma, g-C3N4 Sensitized by an Indoline Dye for Photocatalytic H$_2$ Evolution, Processes. 9 (2021) 1055. https://doi.org/10.3390/pr9061055.

[116]   S. Shen, X. Chen, F. Ren, C.X. Kronawitter, et al., Solar light- driven photocatalytic hydrogen evolution over $ZnIn_2S_4$ loaded with transition-metal sulfides, Nanoscale Res. Lett. 6 (2011) 290. https://doi.org/10.1186/1556-276X-6-290.

[117]   G. Zhu, H. Yin, C. Yang, H. Cui, et al., Black Titania for Superior Photocatalytic Hydrogen Production and Photoelectrochemical Water Splitting, ChemCatChem. 7 (2015) 2614-2619. https://doi.org/10.1002/cctc.201500488.

[118]   H. Zhang, S. Zuo, M. Qiu, S. Wang, et al., Direct probing of atomically dispersed Ru species over multi-edged TiO_2 for highly efficient photocatalytic hydrogen evolution, Sci Adv. 6 (2020). https://doi.org/10.1126/sciadv.abb9823.

[119]   R. Pan, M. Hu, J. Liu, D. Li, et al., Two-Dimensional All-in- One Sulfide Monolayers Driving Photocatalytic Overall Water Splitting, Nano Lett. 21 (2021) 6228–6236. https://doi.org/10.1021/acs.nanolett.1c02008.

[120]   X. Cai, L. Mao, M. Fujitsuka, T. Majima, et al., Effects of Bi- dopant and co-catalysts upon hole surface trapping on $La_2Ti_2O_7$ nanosheet photocatalysts in overall solar water splitting, Nano Res. 15 (2022) 438–445. https://doi.org/10.1007/s12274-021-3498-5.

[121]   X. She, J. Wu, J. Zhong, H. Xu, et al., Oxygenated monolayer carbon nitride for excellent photocatalytic hydrogen evolution and external quantum efficiency, Nano Energy. 27 (2016) 138-146. https://doi.org/10.1016/j.nanoen.2016.06.042.

[122]   X. Yang, X. Wu, J. Li, Y. Liu, TiO2–Au composite nanofibers for photocatalytic hydrogen evolution, RSC Adv. 9 (2019) 29097- 29104. https://doi.org/10.1039/C9RA05113A.,

[123]   T. Wei, Y. Zhu, Y. Wu, X. An, L.M. Liu, Effect of Single-Atom Cocatalysts on the Activity of Faceted TiO_2 Photocatalysts, Langmuir. 35 (2019) 391–397. https://doi.org/10.1021/acs.langmuir.8b03488.

[124]   Y. Chen, S. Ji, W. Sun, Y. Lei, et al., Engineering the Atomic Interface with Single Platinum Atoms for Enhanced Photocatalytic Hydrogen Production, Angew. Chem. Int. Ed. 59 (2020) 1295-1301. https://doi.org/10.1002/anie.201912439.

[125]   J. Yu, Y. Yu, P. Zhou, W. Xiao, B. Cheng, Morphology- dependent photocatalytic H_2-production activity of CdS, Applied Catal. B: Environ. 156-157 (2014) 184-191. https://doi.org/10.1016/j.apcatb.2014.03.013.

[126]   R.K. Chava, J. Yeon Do, M. Kang, Fabrication of CdS-Ag3PO4 heteronanostructures for improved visible photocatalytic hydrogen evolution, J. Alloys Compd. 727 (2017) 86-93. https://doi.org/10.1016/j.jallcom.2017.08.108.

[127]   J. Yu, L. Qi, M. Jaroniec, Hydrogen Production by Photocatalytic Water Splitting over Pt/TiO_2 Nanosheets with Exposed (001) Facets, J. Phys. Chem. C. 114 (2010) 13118–13125. https://doi.org/10.1021/jp104488b.

[128]   Y. Yuan, J. Zheng, X. Zhang, Z. Li, et al., $BaCeO_3$ as a novel photocatalyst with 4f electronic configuration for water splitting, Solid State Ionics. 178 (2008) 1711-1713. https://doi.org/10.1016/j.ssi.2007.11.012.

[129]   H. Kadowaki, N. Saito, H. Nishiyama, Y. Inoue, RuO_2-loaded Sr^{2+}-doped CeO_2 with d0 Electronic Configuration as a New Photocatalyst for Overall Water Splitting, Chem. Lett. 36 (2007) 440. https://doi.org/10.1246/cl.2007.440.

[130] L. Yuliati, J.H. Yang, X. Wang, K. Maeda, et al., Highly active tantalum(v) nitride nanoparticles prepared from a mesoporous carbon nitride template for photocatalytic hydrogen evolution under visible light irradiation, J. Mater. Chem. 20 (2010) 4295-4298. https://doi.org/10.1039/C0JM00341G.

[131] A. Alzahrani, D. Barbash, A. Samokhvalov, "One-Pot" Synthesis and Photocatalytic Hydrogen Generation with Nanocrystalline Ag(0)/CaTiO$_3$ and in Situ Mechanistic Studies, The J. Phys. Chem. C. 120 (2016) 19970–19979. https://doi.org/10.1021/acs.jpcc.6b05407.

[132] M. Wang, P. Ju, W. Li, Y. Zhao, X. Han, Ag$_2$S nanoparticle- decorated MoS$_2$ for enhanced electrocatalytic and photoelectrocatalytic activity in water splitting, Dalton Trans. 46 (2017) 483-490. https://doi.org/10.1039/C6DT04079A.

[133] K. Maeda, K. Teramura, D. Lu, N. Saito, et al., Noble- Metal/Cr$_2$O$_3$ Core/Shell Nanoparticles as a Cocatalyst for Photocatalytic Overall Water Splitting, Angewandte Chemie Int. 45 (2006) 7806-7809. https://doi.org/10.1002/anie.200602473.

[134] H. Li, X. Cui, A hydrothermal route for constructing reduced graphene oxide/TiO$_2$ nanocomposites: Enhanced photocatalytic activity for hydrogen evolution, Int. J. Hydrog. Energy. 39 (2014) 19877-19886. https://doi.org/10.1016/j.ijhydene.2014.10.010.

[135] W. Soontornchaiyakul, T. Fujimura, N. Yano, Y. Kataoka, R. Sasai, Photocatalytic Hydrogen Evolution over Exfoliated Rh-Doped Titanate Nanosheets, ACS Omega. 5 (2020) 9929–9936. https://doi.org/10.1021/acsomega.0c00204.

[136] S. Ida, N. Kim, E. Ertekin, S. Takenaka, T. Ishihara, Photocatalytic Reaction Centers in Two-Dimensional Titanium Oxide Crystals, J. Am. Chem. Soc. 137 (2015) 239–244. https://doi.org/10.1021/ja509970z.

[137] Y. Okamoto, S. Ida, J. Hyodo, H. Hagiwara, T. Ishihara, Synthesis and Photocatalytic Activity of Rhodium-Doped Calcium Niobate Nanosheets for Hydrogen Production from a Water/Methanol System without Cocatalyst Loading, J. Am. Chem. Soc. 133 (2011) 18034–18037. https://doi.org/10.1021/ja207103j.

[138] Zhou, W. J.; Yin, Z. Y.; Du, Y. P.; Huang, X.; Zeng, Z. Y.; Fan, Z. X.; Liu, H.; Wang, J. Y.; Zhang, H., Synthesis of Few-Layer MoS$_2$ Nanosheet-Coated TiO$_2$ Nanobelt Heterostructures for Enhanced Photocatalytic Activities. Small 2013, 9 , 140-147.

[139] Zhang, J.; Zhu, Z. P.; Feng, X. L., Construction of Two-Dimensional MoS$_2$ /CdS p-n Nanohybrids for Highly Efficient Photocatalytic Hydrogen Evolution. Chem. – Eur. J. 2014, 20 , 10632-10635.

[140] Zhu, B. L.; Lin, B. Z.; Zhou, Y.; Sun, P.; Yao, Q. R.; Chen, Y. L.; Gao, B. F., Enhanced photocatalytic H$_2$ evolution on ZnS loaded with graphene and MoS$_2$ nanosheets as cocatalysts. J. Mater. Chem. A 2014, 2 , 3819-3827.

[141] Bai, S.; Wang, L. M.; Chen, X. Y.; Du, J. T.; Xiong, Y. J., Chemically exfoliated metallic MoS$_2$ nanosheets: A promising supporting co-catalyst for enhancing the photocatalytic performance of TiO$_2$ nanocrystals. Nano Res. 2015, 8 , 175-183.

[142] Li, H. D.; Wang, Y. N.; Chen, G. H.; Sang, Y. H.; Jiang, H. D.; He, J. T.; Li, X.; Liu, H., Few-layered MoS_2 nanosheets wrapped ultrafine TiO_2 nanobelts with enhanced photocatalytic property. Nanoscale 2016, 8 , 6101-6109.

[143] Jiapeng Ji, Zeheng Li, Chenchen Hu, Ying Sha, Siyuan Li, Xuehui Gao, Shiyu Zhou, Tong Qiu, Chenyu Liu, Xintai Su, Yang Hou, Zhan Lin, Shaodong Zhou, Min Ling, and Chengdu Liang, Platinum Atomic Clusters Embedded in Defects of Anatase/ Graphene for Efficient Electro- and Photocatalytic ACS Appl. Mater. Interfaces DOI: 10.1021/acsami.0c06931

[144] Xuehua Wang, Xianghu Wang, Jianfeng Huang, Shaoxiang Li, Alan Meng, Zhenjiang Li Interfacial chemical bond and internal electric field modulated Z-scheme S v -$ZnIn_2S_4$ /$MoSe_2$ photocatalyst for efficient hydrogen evolution Nature Communications (2021) 12:4112 | https://doi.org/10.1038/s41467-021-24511-z`

[145] Liuqing Yang, Jianfeng Huang, Li Shi, Liyun Cao, Wei Zhou, Kun Chang, Xianguang Meng, Guigao Liu, Yanni Jie, Jinhua Ye Efficient hydrogen evolution over Sb doped SnO2 photocatalyst sensitized by Eosin Y under visible light irradiation Nano Energy S2211-2855(17)30241-0 http://dx.doi.org/10.1016/j.nanoen.2017.04.039

[146] Pawan Kumar Dubey, Prashant Tripathi, R.S. Tiwari, A.S.K. Sinha, O.N. Srivastava, Synthesis of reduced graphene oxide TiO_2 nanoparticle composite systems and its application in hydrogen production international journal of hydrogen energy39 (2014) 16282 e1 6 292

[147] N.R. Khalid, E. Ahmed, M. Ahmad, N.A. Niaz, M. Ramzan, M. Shakil, T. Iqbal, A. Majid Microwave-assisted synthesis of Ag–TiO_2 /graphene composite for hydrogen production under visible light irradiation Ceramics International (2016), http://dx.doi.org/10.1016/j.ceramint.2016.08.149i

[148] Xiaoyan Zhang, Yujun Sun, Xiaoli Cui a, Zhiyu Jiang A green and facile synthesis of TiO_2 /graphene nanocomposites and their photocatalytic activity for hydrogen evolution international journal of hydrogen energy 37 (2012) 811 e8 15

[149] Tobaldi, D.M.; Lajaunie, L.; Dvoranová, D.; Brezová, V.; Figueiredo, B.; Seabra, M.P.; Calvino, J.J.; Labrincha, J.A. Cooperative and fully reversible color switching activation in hybrid graphene decorated nanocages and copper-TiO_2 nanoparticles. Mater. Today Energy 2020, 17, 100460.

[150] Fan, W.; Yu, X.; Lu, H.-C.; Bai, H.; Zhang, C.; Shi, W. Fabrication of TiO_2 /RGO/Cu_2O heterostructure for photoelectrochemical hydrogen production. Appl. Catal. B Environ. 2015, 7, 32.

[151] Q. Xiang, J. Yu, M. Jaroniec, Enhanced photocatalytic H_2 -production activity of graphene-modified titania nanosheets Nanoscale 3 (2011) 3670.

[152] X.Y. Zhang, H.P. Li, X.L. Cui, Y.H. Lin, Graphene/TiO_2 nanocomposites: synthesis, characterization and application in hydrogen evolution from water photocatalytic splitting J. Mater. Chem. 20 (2010) 2801.

[153] Jo, W.-K.; Jin, Y.-J. 2D graphene-assisted low-cost metal (Ag, Cu, Fe, or Ni)-doped TiO_2 nanowire architectures for enhanced hydrogen generation. J. Alloy. Compd. 2018, 765, 106–112.

[154] Lei Liua_ and Zexiang Shen Bandgap engineering of graphene: A density functional theory study Applied Physics Letters 95, 252104 2009

[155]   Luisa M. Pastrana-Martínez, Sergio Morales-Torres, José L. Figueiredo, Joaquim L. Faria, Adrián M.T. Multifunctional Photocatalytic Materials for Energy Silva, Graphene Photocatalysts chapter 5, Woodhead Publishing in Materials 2018, Pages 79-101

[156]   Chastain, J.; King, R.C., Jr. Handbook of X-ray photoelectron spectroscopy. Perkin-Elmer Corp. 1992, 40, 221.

[157]   Poulston, S.; Parlett, P.M.; Stone, P.; Bowker, M. Surface oxidation and reduction of CuO and Cu_2O studied using XPS and XAES.Surf. Interface Anal. Int. J. Devoted Dev. Appl. Tech. Anal. Surf. Interfaces Thin Film. 1996, 24, 811–820.

[158]   Rudd, J.A.; Jones, D.R.; Dunnill, C.W.; Andreoli, E. Study of copper (II) oxide and copper (II) acetate on multiwalled carbon nanotubes by XPS. Surf. Sci. Spectra 2019, 26, 014013.

[159]   Tobaldi, D. M.; Kočí, K.; Edelmannová, M.; Lajaunie, L.; Figueiredo, B.; Calvino, J. J.; Seabra, M. P.; Labrincha, J. A., Cu_xO and carbon–modified TiO_2–based hybrid materials for photocatalytically assisted H_2 generation. Materials Today Energy 2021, 19, 100607.

[160]   Lignier, P.; Bellabarba, R.; Tooze, R.P. Scalable strategies for the synthesis of well-defined copper metal and oxide nanocrystals. Chem. Soc. Rev. 2012, 41, 1708–1720.

[161]   Gawande, M.B.; Goswami, A.; Felpin, F.-X.; Asefa, T.; Huang, X.; Silva, R.; Zou, X.; Zboril, R.; Varma, R.S. Cu and Cu-based nanoparticles: Synthesis and applications in catalysis. Chem. Rev. 2016, 116, 3722–3811.

[162]   Lewandowski, Ł.;Gajewicz-Skretna, A.; Klimczuk, T.;Trykowski, G.; Nikiforow, K.; Lisowski, W.; Gołąbiewska, A.; Zaleska-Medynska, A. Towards Computer-Aided Graphene Covered TiO2-Cu/(Cu_xO_y) Composite Design for the Purpose of Photoinduced Hydrogen Evolution. Catalysts 2021, 11, 698. https://doi.org/10.3390/catal11060698

[163]   Yuan, J.; Yang, M.-P.; Hu, Q.-L.; Li, S.-M.; Wang, H.; Lu, J.-X., Cu/TiO_2 nanoparticles modified nitrogen-doped graphene as a highly efficient catalyst for the selective electroreduction of CO_2 to different alcohols. Journal of CO_2 Utilization 2018, 24, 334-340.

[164]   Loader, C. Local Regression and Likelihoo; Springer Science & Business Media: Berlin/Heidelberg, Germany, 2006. 36. De Brabanter, K.; De Brabanter, J.; De Moor, B.; Gijbels, I. Derivative Estimation with Local Polynomial Fitting. J. Mach. Learn. Res. 2013, 14, 281–301. 37. Fan, J.

[165]   Gijbels, I. Local Polynomial Modelling and Its Applications: Monographs on Statistics and Applied Probability 66; CRC Press: Boca Raton, FL, USA, 1996; Volume 66. 38.

[166]   Gajewicz-Skretna, A.; Kar, S.; Piotrowska, M.; Leszczynski, J. The kernel-weighted local polynomial regression (KwLPR) approach: An efficient, novel tool for development of QSAR/QSAAR toxicity extrapolation models. J. Cheminformatics 2021, 13, 1–20.

[167] Gramatica, P. Principles of QSAR models validation: Internal and external. QSAR Comb. Sci. 2007, 26, 694–701. 40. Tropsha, A. Best practices for QSAR model development, validation, and exploitation. Mol. Inform. 2010, 29, 476–488.

[168] Chirico, N.; Gramatica, P. Real external predictivity of QSAR models: How to evaluate it? Comparison of different validation criteria and proposal of using the concordance correlation coefficient. J. Chem. Inf. Modeling 2011, 51, 2320–2335.

[169] Roy, K.; Das, R.N.; Ambure, P.; Aher, R.B. Be aware of error measures. Further studies on validation of predictive QSAR models. Chemom. Intell. Lab. Syst. 2016, 152, 18–33.

[170] Hu, Q.; Huang, J.; Li, G.; Chen, J.; Zhang, Z.; Deng, Z.; Jiang, Y.; Guo, W.; Cao, Y. Effective water splitting using CuO_x/TiO_2 composite films: Role of Cu species and content in hydrogen generation. Appl. Surf. Sci. 2016, 369, 201–206

[171] A. B. Murphy, P. R. F. Barnes, L. K. Randeniya, I. C. Plumb, I. E. Grey, M. D. Horne and J. A. Glasscock. Int. J. Hydrogen Energy, 2006, 31, 1999-2017.

[172] Goto, Y. et al. (2018) A particulate photocatalyst water-splitting panel for large-scale solar hydrogen generation. Joule 2, P509–P520

[173] J. Zwara, E. Grabowska, T. Klimczuk, W. Lisowski, A. Zaleska-Medynska, Shapedependent enhanced photocatalytic effect under visible light of Ag_3PO_4 particles, J. Photochem. Photobiol. Chem. 367 (2018) 240–252, https://doi.org/10.1016/j.

[174] Y. Liu, D. Yang, R. Yu, J. Qu, Y. Shi, H. Li, Z.-Z. Yu, Tetrahedral silver phosphate graphene oxide hybrids as highly efficient visible light photocatalysts with excellent cyclic stability, J. Phys. Chem. C 121 (45) (2017) 25172–25179, https://doi.org/10.1021/acs.jpcc.7b07848.

[175] G. Chen, H. Wang, W. Dong, Y. Huang, Z. Zhao, Y. Zeng, Graphene dispersed and surface plasmon resonance-enhanced Ag_3PO_4 (DSPR-Ag_3PO_4) for visible light driven high-rate photodegradation of carbamazepine. https://doi.org/10.1016/j. cej.2020.126850, 1 February 2021, 405.

[176] B. Ohtani, Preparing articles on photocatalysis-beyond the illusions, misconceptions, and speculation, Chem. Lett. 37 (2008) 216–229.

[177] B. Jiang, Y. Wang, J.Q. Wang, C. Tian, W. Li, Q. Feng, Q. Pan, H. Fu, In situ fabrication of Ag/Ag_3PO_4/graphene triple heterostructure visible-light photocatalyst through graphene-assisted reduction strategy, ChemCatChem 5 (6) (2013) 1359–1367, https://doi.org/10.1002/cctc.201390030.

[178] M.I. Shinger, A.M. Idris, S. Devaramani, D.-D. Qin, H. Baballa, S.-T. Zhang, D.L. Shan, X. Lu, In situ fabrication of graphene-based $Ag_3PO_4@$ AgBr composite with enhanced photocatalytic activity under simulated sunlight, J. Environ. Chem. Eng. 5 (2) (2017) 1526–1535, https://doi.org/10.1016/j.jece.2017.02.032.

[179]   G. Chen, M. Sun, Q. Wei, Y. Zhang, B. Zhu, B. Du, Ag$_3$PO$_4$/graphene-oxide composite with remarkably enhanced visible-light-driven photocatalytic activity toward dyes in water, J. Hazard Mater. 244 (2013) 86–93, https://doi.org/10.1016/ j.jhazmat.2012.11.032.

[180]   M.I. Shinger, A.M. Idris, S. Devaramani, D.-D. Qin, H. Baballa, S.-T. Zhang, D. L. Shan, X. Lu, In situ fabrication of graphene-based Ag$_3$PO$_4$@ AgBr composite with enhanced photocatalytic activity under simulated sunlight, J. Environ. Chem. Eng. 5 (2) (2017) 1526–1535, https://doi.org/10.1016/j.jece.2017.02.032.,

[181]   X. Yang, H. Cui, Y. Li, J. Qin, R. Zhang, H. Tang, Fabrication of Ag$_3$PO$_4$-graphene composites with highly efficient and stable visible light photocatalytic performance, ACS Catal. 3 (3) (2013) 363–369, https://doi.org/10.1021/ cs3008126.

[182]   H. Lin, H. Ye, B. Xu, J. Cao, H. Chen, Ag$_3$PO$_4$ quantum dot sensitized BiPO$_4$: a novel p–n junction Ag$_3$PO$_4$/BiPO$_4$ with enhanced visible-light photocatalytic activity, Catal. Commun. 37 (2013) 55–59, https://doi.org/10.1016/j.catcom.2013.03.026.

[183]   [Fu-Jye Sheu, Chun-Pei Cho, Yu-Ting Liao, Chang-tze yu Ag$_3$PO$_4$ -TiO$_2$ -graphene oxide ternary composites with efficient photodegradation, Hydrogen Evolution, and Antibacterial Properties, Catalysts 8 (2018) 57, https://doi.org/10.1016/j. apsusc.2018.10.049.

[184]   Xiaofei Yang, Haiying Cui, Li Yang, Jieling Qin, Rongxian Zhang, Hua Tang, Fabrication of Ag$_3$PO$_4$-graphene composites with highly efficient and stable visible light photocatalytic performance, ACS Catal. 3 (2013) 363–369, https://doi.org/ 10.1021/cs3008126.

[185]   Can Cui, Yaping Wang, Dayu Liang, Wei Cui, Haihua Hu, Bingqing Lu, Sheng Xu, Xiaoyun Li, Chong Wang, Yu Yang Photo-assisted synthesis of Ag$_3$PO$_4$/reduced graphene oxide/Ag heterostructure photocatalyst with enhanced photocatalytic activity and stability under visible light, Appl. Catal. B Environ. (2014) 158 159, https://doi.org/10.1016/j.apcatb.2014.04.007, 150–160.

[186]   Ma Ni, Yiwei Qiu, Yichao Zhang, Hanyang Liu, Yana Yang, Jingwei Wang, Xiaoyun Li, Can Cui Reduced graphene oxide enwrapped pinecone-liked Ag$_3$PO$_4$/ TiO$_2$ composites with enhanced photocatalytic activity and stability under visible light, J. Alloys Compd. 648 (2015), https://doi.org/10.1016/j.

[187]   Can Cui, Yaping Wang, Dayu Liang, Wei Cui, Haihua Hu, Bingqing Lu, Sheng Xu, Xiaoyun Li, Chong Wang, Yu Yang Photo-assisted synthesis of Ag$_3$PO$_4$/reduced graphene oxide/Ag heterostructure photocatalyst with enhanced photocatalytic activity and stability under visible light, Appl. Catal. B Environ. (2014) 158–159, https://doi.org/10.1016/j.apcatb.2014.04.007, 150–160.

[188] Ma Ni, Yiwei Qiu, Yichao Zhang, Hanyang Liu, Yana Yang, Jingwei Wang Xiaoyun Li, Can Cui Reduced graphene oxide enwrapped pinecone-liked Ag_3PO_4/ TiO_2 composites with enhanced photocatalytic activity and stability under visible light, J. Alloys Compd. 648 (2015), https://doi.org/10.1016/j. jallcom.2015.07.070, 818e825.

[189] Ma Ni, Yiwei Qiu, Yichao Zhang, Hanyang Liu, Yana Yang, Jingwei Wang Xiaoyun Li, Can Cui Reduced graphene oxide enwrapped pinecone-liked Ag_3PO_4/ TiO_2 composites with enhanced photocatalytic activity and stability under visible light, J. Alloys Compd. 648 (2015), https://doi.org/10.1016/j. jallcom.2015.07.070, 818e825.

[190] Guodong Chen, Meng Sun, Wei Qin, Yongfang Zhang, Baocun Zhu, Bin Du Ag_3PO_4/ graphene oxide composite with remarkably enhanced visible light-driven photocatalytic activity toward dyes in water, 244– 245, J. Hazard Mater. (2013) 86–93, https://doi.org/10.1016/j.jhazmat.2012.11.032.

[191] Quanjun Xiang, Di Lang, Tingting Shen, Fan Liu Graphene-modified nanosized Ag_3PO_4 photocatalysts for enhanced visible-light photocatalytic activity and stability, Appl. Catal. B Environ. 162 (2015) 196, https://doi.org/10.1016/j. apcatb.2014.06.051. –203.

[192] Quanjun Xiang, Di Lang, Tingting Shen, Fan Liu Graphene-modified nanosized Ag_3PO_4 photocatalysts for enhanced visible-light photocatalytic activity and stability, Appl. Catal. B Environ. 162 (2015) 196, https://doi.org/10.1016/j.apcatb.2014.06.051. –203

[193] Yan, J.; Wang, C.; Xu, H.; Xu, Y.; She, X.; Chen, J.; Song, Y.; Li, H.; Zhang, Q., AgI/Ag_3PO_4 heterojunction composites with enhanced photocatalytic activity under visible light irradiation. Applied surface science 2013, 287, 178-186. https://doi.org/10.1016/j.apsusc.2013.09.113,

[194] Gu, X.-q.; Zhang, S.; Wang, B.; Qiang, Y.-h., Synthesis and photocatalytic performance of Ag_3PO_4/$AgCl$ hybrids. Optoelectronics Letters 2014, 10 (2), 119-122. https://doi.org/10.1007/s11801-014-3221-9

[195] Amornpitoksuk, P.; Suwanboon, S., Photocatalytic decolorization of methylene blue dye by Ag_3PO_4–AgX (X= Cl^-, Br^- and I^-) under visible light. Advanced Powder Technology 2014, 25 (3), 1026-1030. https://doi.org/10.1016/j.apt.2014.02.001

[196] Lei Liu, Jincheng Liu, Darren Delai Sun Graphene oxide enwrapped Ag_3PO_4 composite: towards a highly efficient and stable visible-light induced photocatalyst for water purification, Catal. Sci. Technol. 2 (2012) 2525–2532, https://doi.org/ 10.1039/C2CY20483E.

[197] Bo Chai, Li Jing, Qian Xu, Reduced graphene oxide grafted Ag_3PO_4 composites with efficient photocatalytic activity under visible-light irradiation, Ind. Eng. Chem. Res. 53 (2014), https://doi.org/10.1021/ie4041065, 8744

[198] G. Chen, M. Sun, Q. Wei, Y. Zhang, B. Zhu, B. Du, Ag_3PO_4/graphene-oxide composite with remarkably enhanced visible-light-driven photocatalytic activity toward dyes in water, J. Hazard Mater. 244 (2013) 86–93, https://doi.org/ 10.1016/j.jhazmat.2012.11.032.

[199] W. Chen, X. Niu, J. Wang, A photocatalyst of graphene oxide (GO)/Ag$_3$PO$_4$ with excellent photocatalytic activity over decabromodiphenyl ether (BDE-209) under visible light irradiation, J. Photochem. Photobiol. Chem. 356 (2018) 304–311, https://doi.org/10.1016/j.jphotochem.2017.12.038.

[200] L. Liu, J. Liu, D.D. Sun, Graphene oxide enwrapped Ag$_3$PO$_4$ composite: towards a highly efficient and stable visible-light-induced photocatalyst for water purification, Catal. Sci. Technol. 2 (12) (2012) 2525–2532, https://doi.org/10.1039/C2CY20483E.

[201] L. Xu, Y. Wang, J. Liu, S. Han, Z. Pan, L. Gan, High-efficient visible-light photocatalyst based on graphene incorporated Ag$_3$PO$_4$ nanocomposite applicable for the degradation of a wide variety of dyes, J. Photochem. Photobiol. Chem. 340 (2017) 70–79, https://doi.org/10.1016/j.jphotochem.2017.02.022.

[202] Fu-Jye Sheu, Chun-Pei Cho, Yu-Ting Liao, Chang-tze yu Ag$_3$PO$_4$ -TiO$_2$ -graphene oxide ternary composites with efficient photodegradation, Hydrogen Evolution, and Antibacterial Properties, Catalysts 8 (2018) 57, https://doi.org/10.1016/j.apsusc.2018.10.049.

[203] Xiaofei Yang, Haiying Cui, Li Yang, Jieling Qin, Rongxian Zhang, Hua Tang, Fabrication of Ag$_3$PO$_4$-graphene composites with highly efficient and stable visible light photocatalytic performance, ACS Catal. 3 (2013) 363–369, https://doi.org/ 10.1021/cs3008126.

[204] Q.H. Liang, Y. Shi, W.J. Ma, Z. Li, X.M. Yang, Enhanced photocatalytic activity and structural stability by hybridizing Ag$_3$PO$_4$ nanospheres with graphene oxide sheets, Phys. Chem. Chem. Phys. 14 (2012) 15657–15665, https://doi.org/10.1039/C2CP42465G.

[205] C. Cui, Y.P. Wang, D.Y. Liang, W. Cui, H.H. Hu, B.Q. Lu, S. Xu, X.Y. Li, C. Wang, Y. Yang, Photo-assisted synthesis of Ag$_3$PO$_4$/reduced graphene oxide/Ag heterostructure photocatalyst with enhanced photocatalytic activity and stability under visible light, Appl. Catal. B Environ. 158 (2014) 150–160, https://doi.org/10.1016/j.apcatb.2014.04.007.

[206] Pengyu Dong, Guihua Hou, Chao Liu, Xinjiang Zhang, Hao Tian, Fenghua Xu, Xinguo Xi, Rong Shao, Origin of activity and stability enhancement for Ag$_3$PO$_4$ photocatalyst after calcination, Materials 9 (2016) 968, https://doi.org/10.3390/ma9120968,

[207] Yong Han Jerome Leow, Patria Yun Xuan Lim, Sharon Xiaodai Lim, Jianfeng Wu, Chorng-Haur Sow, Nanosurfer flash-mobs: electric-field-choreographed silver migration on graphene oxide, Nanoscale Adv. 1 (2019) 2180, https://doi.org/10.1039/c9na00151d.

[208] Jussi Kukkonen, Aimo Oikari, Bioavailability of organic pollutants in boreal waters with varying levels of dissolved organic material, Water Research, Volume 25, Issue 4, 1991, Pages 455-463, ISSN 0043-1354, https://doi.org/10.1016/0043-1354(91)90082-2.

[209] Srimanti Duttagupta, Abhijit Mukherjee, Animesh Bhattacharya, Jayanta Bhattacharya, Wide exposure of persistent organic pollutants (PoPs) in natural waters and sediments of the densely populated Western Bengal basin, India, Science of The Total Environment, Volume 717, 2020, 137187, ISSN 0048-9697, https://doi.org/10.1016/j.scitotenv.2020.137187.

[210] Anne-Laure Badin, Pierre Faure, Jean-Philippe Bedell, Cécile Delolme, Distribution of organic pollutants and natural organic matter in urban storm water sediments as a function of grain size, Science of The Total Environment, Volume 403, Issues 1–3, 2008, Pages 178-187, ISSN 0048-9697, https://doi.org/10.1016/j.scitotenv.2008.05.022

[211] Philip M. Gschwend and Shianchee. Wu On the constancy of sediment-water partition coefficients of hydrophobic organic pollutants Environmental Science & Technology 1985 19 (1), 90-96 DOI: 10.1021/es00131a011

[212] Biesinger, M.C. Advanced analysis of copper X-ray photoelectron spectra. Surf. Interface Anal. 2017, 49, 1325–1334.

[213] Terzyk, A.P. The influence of activated carbon surface chemical composition on the adsorption of acetaminophen (paracetamol) in vitro: Part II. TG, FTIR, and XPS analysis of carbons and the temperature dependence of adsorption kinetics at the neutral pH. Colloids Surf. A Physicochem. Eng. Asp. 2001, 177, 23–45.

13. Doctoral candidate's scientific achievements

International journals, first author:

1. Lewandowski Łukasz, Zwara Julia, Gołąbiewska Anna, Klimczuk Tomasz, Trykowski Grzegorz, Zaleska-Medynska Adriana: New approach for the synthesis of Ag_3PO_4-graphene photocatalysts, Materials Science in Semiconductor Processing, vol. 149, 2022, article number: 106851, s. 1-11, DOI:10.1016/j.mssp.2022.106851, 70 punktów, IF(4,644)

2. Lewandowski Łukasz, Gajewicz-Skrętna Agnieszka, Klimczuk Tomasz, Trykowski Grzegorz, Nikiforow Kostiantyn, Lisowski Wojciech, Gołąbiewska Anna, Zaleska-Medynska Adriana: Towards computer-aided graphene covered TiO_2-Cu/(Cu$_x$O$_y$) composite design for the purpose of photoinduced hydrogen evolution, Catalysts, vol. 11, nr 6, 2021, article number: 698, s. 1-19, DOI:10.3390/catal11060698, 100 punktów, IF(4,501)

Patent applications, first author:

1. Lewandowski Ł., Zaleska-Medynska A., Sposób wytwarzania warstw węglowych zawierających grafen na nanocząstkach, zwłaszcza kropkach kwantowych, zawierających co najmniej jeden materiał półprzewodnikowy, oraz naczynie reakcyjne do wytwarzania warstw węglowych zawierających grafen na nanocząstkach zawierających co najmniej jeden materiał półprzewodnikowy, zwłaszcza tlenkach metali i materiałach kompozytowych, (A method of producing carbon layers containing graphene on nanoparticles, especially quantum dots, containing at least one semiconductor material, and a reaction vessel for producing carbon layers containing graphene on nanoparticles containing at least one semiconductor material, especially metal oxides and composite materials.) Patent Application P.430994 (data zgłoszenia: 29.08.2019)

International conference presentations:

1. Lewandowski Łukasz, Gajewicz-Skrętna Agnieszka, Klimczuk Tomasz, Trykowski Grzegorz, Nikiforow Kostiantyn, Lisowski Wojciech, Gołąbiewska Anna, Zaleska-Medynska Adriana: Prezentacja pod tytułem "Fluidised Bed Reactor Used for Graphene Wrapping of Photocatalyst for Photoinduced Hydrogen Evolution" presented at: "11th European Conference on Solar Chemistry and Photocatalysis: Environmental Applications (SPEA)" 6-10 Czerwca 2022, Turin, Italy.

International journals, supporting author:

1. Nevarez Martinez Maria, Cavdar Onur, Haliński Łukasz, Miodyńska Magdalena, Parnicka Patrycja, Bajorowicz Beata, Kobylański Marek, Lewandowski Łukasz, Zaleska-Medynska Adriana: Hydrogen detection during photocatalytic water splitting: a tutorial, International Journal of Hydrogen Energy, Elsevier, vol. 47, nr 35, 2022, s. 15783-15788, DOI:10.1016/j.ijhydene.2022.03.050, 140 points, IF(7,139)

2. Elżbieta Łysiak-Pastuszak1, Włodzimierz Krzymiński, Łukasz Lewandowski Development of tools for ecological quality assessment in Polish marine areas according to the Water Framework Directive. Part I – Nutrients Oceanol. Hydrobiol. St. 2009 Vol. XXXVIII, No.3 (87-99)

3. Elżbieta Łysiak-Pastuszak, Włodzimierz Krzymiński, Łukasz Lewandowski Development of tools for ecological quality assessment in polish marine areas according to the Water Framework Directive. Part II – Chlorophyll-a Oceanol. Hydrobiol. St. 2009 Vol. XXXVIII, No.3 (101-112)

4. Elżbieta Łysiak-Pastuszak, Włodzimierz Krzymiński, Łukasz Lewandowski Development of tools for ecological quality assessment in polish marine areas according

to the Water Framework Directive. Part III – Secchi depth Oceanol. Hydrobiol. St. 2009 Vol. XXXVIII, No.3 (113-124)

5. Andrzej Osowiecki, Elżbieta Łysiak-Pastuszak,, Lidia Kruk-Dowgiałło, Magdalena Błeńska, Paulina Brzeska,Wojciech Kraśniewski, Łukasz Lewandowski, Włodzimierz Krzymiński Development of tools for ecological quality assessment in the Polish marine areas according to the Water Framework Directive. Part IV - preliminary assessment Oceanol. Hydrobiol. St. 2012 Volume 41 , Issue 3 (1-10)

6. Helcom 2009 - Eutrophication in the Baltic Sea - An integrated thematic assessment of the effects of nutrients enrichment and eutrophication in the Baltic Sea region. Balt. Sea Environ. Proc. No. 115B. (Contributor)

Polish journals, supporting author:

1. Elżbieta Łysiak-Pastuszak, Maria Bartoszewicz ,Katarzyna Bradtke, Mirosław Darecki, Natalia Drgas, Piotr Kowalczuk, Wojciech Kraśniewski, Adam Krężel, Włodzimierz Krzymiński, Łukasz Lewandowski, Hanna Mazur-Marzec, Bogusz Piliczewski, Sławomir Sagan, Katarzyna Sutryk, Barbara Witek A study of episodic events in the Baltic Sea – combined in situ and satellite observations 2012 OCEANOLOGIA, 54 (2) (121 - 141)

2. Stan środowiska polskiej strefy przybrzeżnej Bałtyku w latach 1986-2005 Wybrane zagadnienia, Pod redakcją Mirosława Miętusa i Marzenny Sztobryn Warszawa 2011 - Monografie Instytutu Meteorologii i Gospodarki Wodnej ISBN 978-83-61102-52-6 (Co-author of chapters "Oxygenation of waters" and "Nutrients in the sea.")

3. Bałtyk Południowy Charakterystyka wybranych elementów środowiska – Co-author of issues 2007-2012 Publisher - IMGW.